Chapter 3
The Atmospheric Channel

Abhijit Biswas and Sabino Piazzolla

An optical receiving network that can provide availability similar to the National Aeronautics and Space Administration's (NASA's) existing radio frequency (RF) Deep Space Network (DSN) is being considered for future planetary exploration, where large data volumes acquired using advanced sensors must be returned to scientists on Earth. Optical groundbased receiving networks are an option for realizing this objective. The interaction between laser beams and the atmosphere must be taken into account in order to fully exploit this option. Alternatively, atmospheric effects on the laser beam can be partially or completely eliminated by resorting to either airborne or spaceborne optical receivers. The reason for considering groundbased networks, however, lies in the perceived reductions in cost and risk. Deploying a receiving station in space with the flexibility of re-configuring receiver settings will be expensive and vulnerable to single-point failures. With the maturity in technologies for deploying relatively large apertures on airborne and orbital platforms the cost and feasibility of achieving spaceborne operations seems very likely. However, current estimates for deploying a single fully functional receiver in Earth orbit are comparable to the cost of building an entire ground network, a fact that motivates a close study of the prospects and consequences of implementing a ground network, at least until such time as the cost of deploying receivers in space becomes more competitive.

This chapter describes the effects of Earth's atmosphere upon laser communication beams. Clouds, fog, haze, mist, and other precipitation in the atmosphere cause strong attenuation of the laser signal and cause communication outages. Fortunately, weather diversity or the global cloud

distribution patterns can provide, with a reasonably high likelihood, a cloud free line of sight (CFLOS) for the optical link to at least one location on the ground. Note that, depending upon the design of the optical communication system, CFLOS must be maintained not only for reception of the laser beam from space, but also for transmission of a pointing reference beacon and/or an uplink command laser. This can be an important consideration when the receiving and transmitting terminals are not co-located on the ground. Analysis of local and global statistical distribution of clouds provides the quantitative estimates of CFLOS described in Section 3.1.

Even when CFLOS can be maintained, atmospheric effects continue to play a critical role in the link performance. Spectral attenuation due to absorption and scattering of the laser signal by atmospheric molecular and aerosol constituents determine the laser signal that can be received from or transmitted to space. Therefore, choosing laser wavelengths that do not coincide with strong absorption bands in the atmosphere is critical. Section 3.2 elaborates upon spectral attenuation predictions with a description of measurements made at Jet Propulsion Laboratory (JPL) to verify the predictions and their statistics.

Though optical reception of laser communications has similarities with low-light detection applications extant in astronomy and satellite laser ranging, a significant point of departure is the need to operate the links during day as well as night with a relatively high probability of correct detection. Therefore, sky radiance, or sunlight scattered and reflected by atmospheric constituents, plays a major role in determining link performance. Under the most stressing circumstances, the ground station design must support links when the spacecraft angular separation from the Sun, or Sun-Earth-probe (SEP) angle is approximately 2–3 deg. The sky radiance usually increases with angular proximity to the Sun and is influenced by the aerosol concentration and airmass through which communications must be maintained. Atmospheric modeling software can provide reasonable predictions of sky radiance under a varying set of assumptions. The background photon flux resulting from sky radiance, especially at low SEP angles can be considered to have a twofold contribution. First, the field of view (FOV) of sky imaged onto the detector by the light-collection system is directly proportional to the background. Second, light from outside the FOV (or “stray light”) is scattered and reflected onto the detector. The latter contribution is highly dependent upon the light-collection system used. The light-collection system must necessarily use properly designed narrow band-pass optical filters to minimize both the in-band light and leakage of out-of-band background light that is incident on the detector. Section 3.2 below also presents a discussion on models used to predict sky radiance and a comparison between the predictions and the field data.

NASA’s deep space programs so far have relied upon a global network of RF antennas to capture the signal return from the spacecraft. However, for the case of optical signal return from deep space, new architectural and system

problems are encountered because of atmospheric channel effects. Section 3.3 introduces the problem of deploying a ground optical deep-space network and its site selection.

The atmosphere is a dynamic medium with a randomly varying refractive index to a propagating laser beam. The resulting perturbations of the laser beam wavefront originating from space or being transmitted from the ground are broadly called atmospheric “seeing” effects. Thus, atmospheric “seeing” effects result in solid angles, or equivalently, the FOV of the ground light-collection system being many times the diffraction limit, assuming perfect optics. The penalty for the increased FOV is an increase in background light. Especially during daytime optical links, near the Sun the penalty can be severe. Other effects include the irradiance fluctuations of the laser beams received and transmitted, tilts and wander of the beam fronts, and spreading of the beam widths. These effects, and their impact on link performance, are discussed in Section 3.4

3.1 Cloud Coverage Statistics

Cloud opacity is an atmospheric physical phenomenon that jeopardizes optical links from deep space to any single ground station. Clearly, when clouds are in the line-of-sight, the link is blocked. Therefore, ground receiving telescopes need to be located in sites where cloud coverage is low and statistically predictable. Moreover, to guarantee continuity of data delivery from deep space to ground, while the Earth is rotating, a global network of telescopes is necessary. The selection of the sites for telescopes belonging to an optical deep space network (ODSN) is driven by considerations based, among other factors, on cloud-cover statistics.

To characterize the atmospheric channel and global cloud coverage, a number of resources are actually available to the scientific community. International agencies, institutions, and programs have made available sources of weather data and cloud coverage around the globe. For instance, the International Satellite Cloud Climatology Project (ISCCP) [1] is one source for weather data that can be utilized for selection of optimal telescope sites. ISCCP extracts and elaborates data from a multitude of weather satellites, e.g., Geostationary Operational Environmental Satellite (GOES), European weather observation satellite (METEOSAT), Geostationary Meteorological Satellite (GMS), Indian National Satellite (INSAT), and National Oceanic & Atmospheric Administration (NOAA) polar orbiting satellites. Another source of atmospheric data is the NOAA National Climatic Data Center (NCDC) that can provide surface observation data from observation sites distributed all around the globe [2].

In this chapter we present two different approaches to elaborate statistical characterization of the cloud coverage. First, we present a study of cloud

distributions in the United States Southwest using surface observation data from NCDC. Then, we discuss the results of ongoing research by TASC Inc. [3] under JPL contract and based on satellite observations.

3.1.1 National Climatic Data Center Data Set

The NCDC is the sole climatic record center for the Department of Commerce. The NCDC collects, prepares, and distributes climate data regarding the United States, and the NCDC is also responsible for the United States branch of the World Data Center (along with Russia, Japan, and China).

Among the different types of environmental and weather observations collected and maintained by the NCDC, the work presented here is specifically based on the elaboration and processing of surface observation data. Surface observations are meteorological data that describe the climate of an area (or a site) where an observation station is located. Surface observations for each site indicate temperature, humidity, precipitation, snowfall, wind speed and direction, atmospheric pressure, visibility, and other kinds of weather conditions, including obscurations. The observations are (in general) made hourly, recorded, and collected by a certified operator. The data that we analyzed are in a format DATSAV3 (NCDC designation).

Essentially, the DATSAV3 format consists of rows of data, where each row contains the weather observations made at a specific moment of the day. To indicate the cloud coverage of the celestial dome, a station operator uses standardized requirements specified by the Federal Meteorological Handbook [4]. According to these requirements, an operator during an observation specifies the cloud coverage in “eighths” or “oktas” that are assigned according to the following numeric code: “0” when no clouds are present in the celestial dome (clear sky); “2” when the celestial dome is less than half covered (0 <cloud coverage <4/8) (scattered sky); “7” when the celestial dome is less then 7/8 covered (4/8 <cloud coverage <7/8) (broken sky); “8” when clouds completely cover the celestial dome, except perhaps a small portion (overcast sky).

A study is presented here that considers ten different sites in the United Sates Southwest with locations ranging from California through Texas (Fig. 3-1), and it presents an analysis of cloud coverage records of these sites over a number of years [5]. The United States Southwest is home to a large number of telescopes due to its dry weather, which manifests itself in a limited number of cloudy days with respect to other areas of the United States (and North America in general). Such a large geographical area, however, does not present a uniform weather (and cloud coverage) pattern during the year. For instance, while California experiences dry summers and storms during the winter, Arizona and New Mexico are mainly affected by stormy summer seasons. Therefore, our intent in this study is also to understand the variation

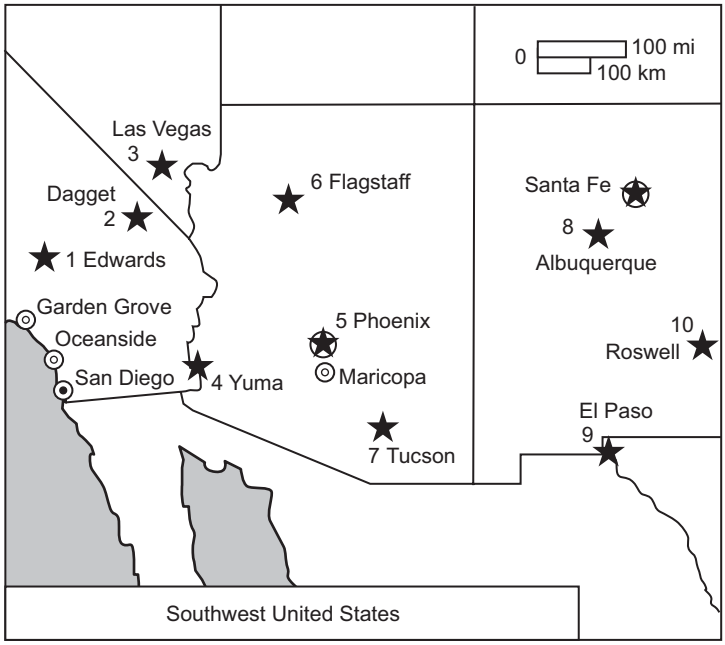

Fig. 3-1. Site Locations (denoted by stars) in the United States Southwest for which cloud coverage statistics have been characterized in this work.

and the correlation of cloud coverage in this area. To accomplish this goal, we have selected ten NCDC observation stations in the region in an area from California (Edwards Air Force Base, 101 km northeast of Los Angeles) to the border between New Mexico and Texas, as indicated in Fig. 3-1. The maximum distance between sites is 1241 km (from Edwards in California to Roswell in New Mexico). There are several reasons for the selection of these particular observation sites. The first one, as already noted, is the intention to cover the relatively dry Southwest. Another reason is to select sites that are near existing telescope facilities. For example, at Table Mountain (California), NASA/JPL deployed a telescope for optical communication; therefore, we selected the NCDC observation station of Edwards Air Force Base, California, which is in the vicinity of Table Mountain Observatory (65 km).

Finally, we selected observation sites near locations or peaks that can be considered for future installation of optical telescopes [5,6]. The selected locations are: (1) Edwards Air Force Base, California; (2) Daggett Airport, California; (3) Las Vegas McCarran International Airport, Nevada; (4) Yuma International Airport, Arizona; (5) Phoenix Sky Harbor International Airport, Arizona; (6) Flagstaff Pulliam Airport, Arizona; (7) Tucson International Airport, Arizona; (8) Albuquerque International Airport, New Mexico; (9) El

Paso International Airport, Texas; (10) Roswell Industrial Airpark, New Mexico.

Most of the NCDC observation centers are located at airports or other locations with relatively modest elevations. By contrast, telescopes are located at higher elevations (usually mountain peaks). Therefore, one may expect (and plan for) different sky visibility conditions between mountain peaks and lower elevation areas in their proximity. For instance, fog and smog do not usually appear at higher elevations because they remain constrained by the inversion layer. Moreover, at higher elevations, mountains may cut off lower clouds, and sometimes the orographic effects of the mountains trap and localize clouds.

3.1.2 Single-Site and Two-Site Diversity Statistics

Initially, we considered 27 years worth of data from NCDC for the ten observation stations (1973–1999). However, in order to have consistent statistics, we considered only years in which the percentage of missing data is at most of the order of one and a half months (13 percent of the year-time amount). Moreover, we considered only years with missing data distributed over the year (i.e., years with an entire month of missing data were disregarded). These principles led us to restrict our study to six years 1991–1993 and 1997–1999 only. Finally, owing to the proximity of Edwards to the Table Mountain Observatory where NASA/JPL has a telescope for optical communications, we emphasize data involving the observation station of Edwards itself [7]. Because of the interest in studying a possible telescope network for deep space optical communications, we present also site diversity data between two sites. The diversity data are obtained by comparing simultaneous cloud coverage between two sites and then by selecting the better sky condition (less cloud coverage).

In Table 3-1 we present and compare the improvement in the average yearly amount of clear sky of two-site diversity over single sites. Figure 3-2 compares the average cumulative distribution of the cloud coverage for single observation site and two-site diversity regarding Edwards and Roswell. Two-site diversity greatly increases the yearly amount of clear sky (66.57 percent), and for cloud coverage less than 4/8 (91.14 percent) with respect to the single site. Another interesting case to consider is two-site diversity between Edwards and Tucson as presented in Fig. 3-3, especially because they are close to existing observatories (i.e., the Goldstone facility (California) and the Mount Lemmon Observatory (Tucson, Arizona)). Even in this case, two-site diversity provides an overall improvement over Tucson and Edwards with clear sky amounts of 61.01 percent and 90.82 percent for cloud coverage less then four eighths.

Table 3-1. Clear sky percentage averaged over six years for single-site (diagonal bold) and two-site diversity.

	Edwards	Daggett	Las Vegas	Yuma	Phoenix	Flagstaff	Tucson	Albuquerque	El Paso	Roswell
Edwards	**26.8**	45.5	51.8	41.3	48.3	50.4	61.0	49.1	58.7	66.5
Daggett	45.5	**41.4**	56.6	50.0	55.5	58.9	68.7	58.4	66.6	74.9
Las Vegas	51.8	56.6	**46.5**	54.6	57.9	59.6	68.0	58.4	67.6	75.0
Yuma	41.3	50.0	54.6	**28.8**	44.5	52.8	57.6	48.2	57.1	66.3
Phoenix	48.3	55.5	57.9	44.5	**36.9**	55.6	57.1	50.1	58.6	68.2
Flagstaff	50.4	58.9	59.6	52.8	55.6	**40.6**	63.4	55.9	65.3	68.8
Tucson	61.0	68.7	68.0	57.6	57.1	63.4	**49.8**	58.1	62.2	68.4
Albuquerque	49.1	58.4	58.4	48.2	50.1	55.9	58.1	**33.3**	54.1	63.1
El Paso	58.7	66.6	67.6	57.1	58.6	65.3	62.2	54.1	**44.7**	65.7
Roswell	66.5	74.9	75.0	66.3	68.2	68.8	68.4	63.1	65.7	**55.0**

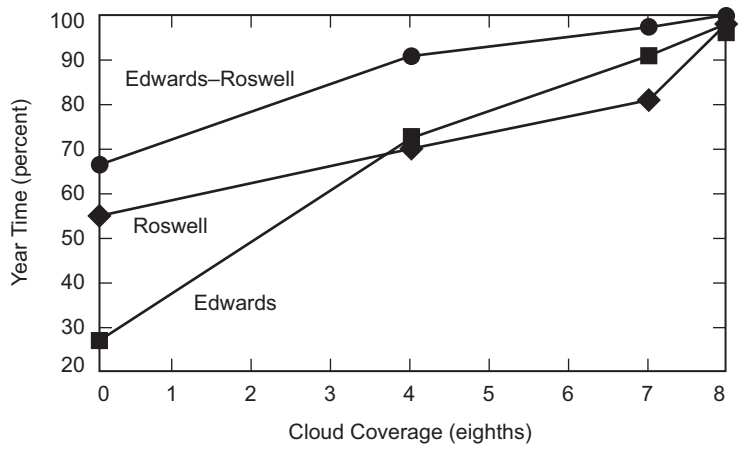

Fig. 3-2. Comparison of cumulative average cloud coverage among one-site Roswell, one-site Edwards, and two-site diversity for combined Roswell and Edwards for the years 1991–1993 and 1997–1999. Since NASA/JPL installed an optical telescope at Table Mountain in the proximity of Edwards, Roswell is a potential location in whose proximity a telescope will enhance the two-site diversity with Table Mountain.

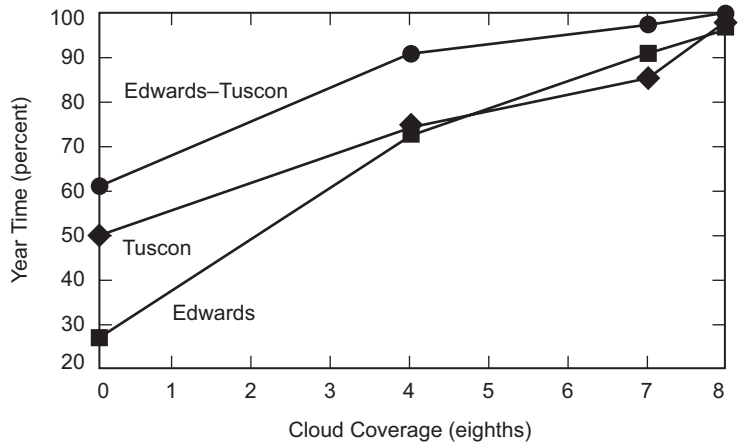

Fig. 3-3. Comparison of cumulative average cloud coverage among one-site Tucson, one-site Edwards, and two-site diversity for combined Tucson and Edwards for the years 1991–1993 and 1997–1999.

Because Edwards has the average lowest clear sky amount among the ten locations, one should expect that other locations could offer higher yields of clear sky amount for two-site diversity.

In fact, best results in two-site diversity involve Roswell and Daggett (see Fig. 3-4), or Roswell and Las Vegas (see Fig. 3-5). In these two cases, the clear sky amount is about 75 percent.

Cloud coverage data from each observation station present monthly variations that greatly differ during the year depending on the geographical

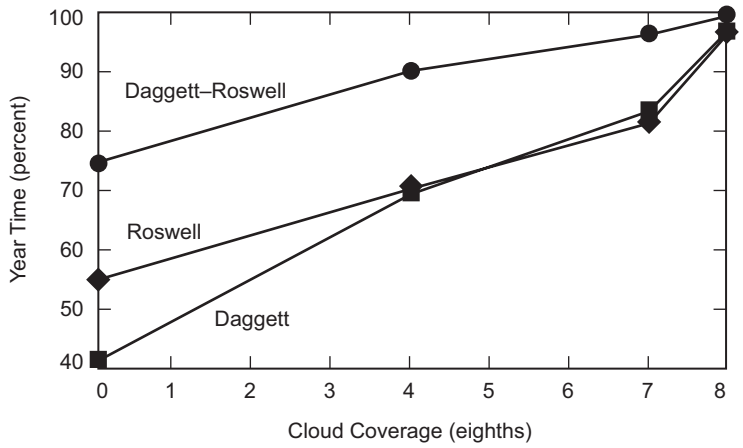

Fig. 3-4. Comparison of cumulative average cloud coverage among one-site Daggett, one-site Roswell, and two-site diversity for Daggett and Roswell for the years 1991–1993 and 1997–1999.

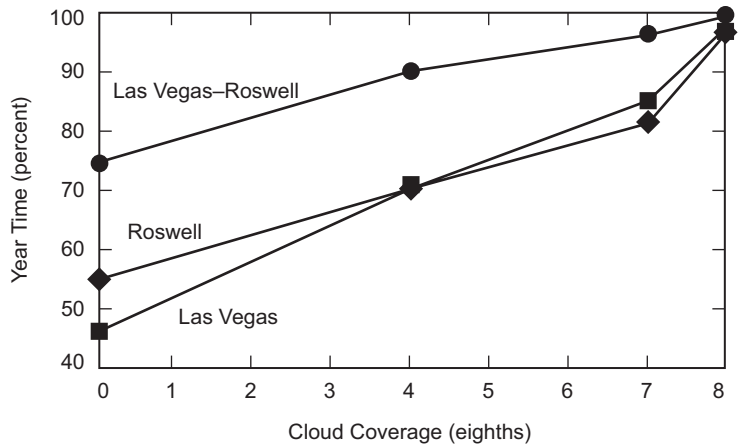

Fig. 3-5. Comparison of cumulative average cloud coverage among one-site Las Vegas, one-site Roswell, and two-site diversity for combined Las Vegas and Roswell for the years 1991–1993 and 1997–1999.

area. For instance, while the clear sky amount was smaller during the winter in Southern California, the same was not true in New Mexico and part of Arizona, where clear sky amount was reduced during the summer months of July and August. Therefore, upon selection of proper locations, one should expect that in two-site diversity statistics the monthly variation of clear sky (and other cloud coverage conditions) would be more uniform over the year. To better prove this last statement, in this segment we discuss monthly variations of two-site diversity statistics involving Edwards, Daggett, Las Vegas, Tucson, and Roswell.

Figure 3-6 presents average monthly variations of cloud coverage between Edwards and Tucson. The differences between Edwards and Tucson are evident in Figs. 3-6(a) and 3-6(c). Consequences of two-site diversity are shown in Fig. 3-6(e), where during the months of winter, spring, and autumn the dominant clear-sky contribution to the statistics is given by Tucson, while during the summer Edwards compensates for the lack of clear sky at Tucson. A monthly variation is still visible in the two-site statistics for the clear sky, but overall we can observe an average of 15 days of clear sky all year round. Two-site diversity between Edwards and Roswell (Fig. 3-7) presents more favorable conditions. In fact, the clear sky amount for the combination of these sites does not change much over the year. Except for January and February, the average clear sky amount for the two-site diversity is approximately 20 days. As previously noted, Daggett and Roswell (Fig. 3-8) along with Las Vegas and Roswell (Fig. 3-9) are the most advantageous choices for two-site diversity. Las Vegas–Roswell two-site diversity presents minimal variation of clear sky amount over the year, with an average of 2/3 clear sky for each month.

3.1.3 Three-Site Diversity

Three-site diversity may offer further improvement of clear sky (and clear plus scattered sky) over two-site diversity. Figure 3-10 presents some results of three-site diversity involving Edwards during the years 1991–1993 and 1997–1999. Among the curves in Fig. 3-10, there is the cloud-coverage cumulative distribution curve that describes a case study with Edwards–Daggett–Tucson. For this configuration, the average clear sky amount is 70.6 percent during the year. However, the fact that Daggett is in the proximity of Edwards and that they both belong to the same climate area does not constitute a good choice for three-site diversity. As a result, for this site selection example, the benefits of having three stations operating simultaneously are greatly reduced. In fact, one may notice that during the same period of time, the clear sky amount for two-site diversity of Tucson and Dagget is 68.79 percent, which suggests that the addition of Edwards to the other two stations provides only marginal improvement of the overall statistics. Adding Roswell to Edwards

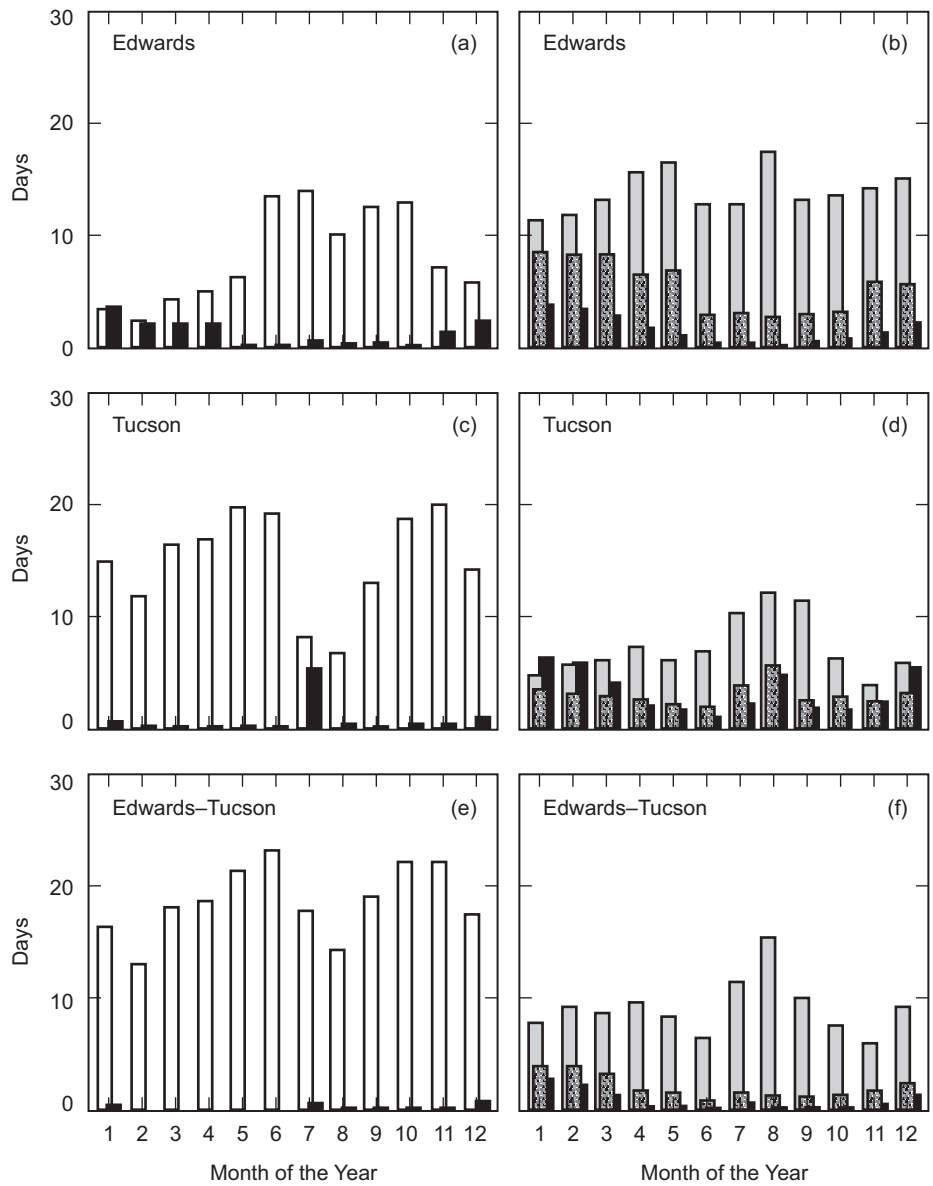

Fig. 3-6. Average monthly cloud coverage: comparison of cumulative average cloud coverage among one-site Edwards, one-site Tucson, and two-site diversity for combined Edwards and Tucson. February is averaged over 28 days: (a), (c), and (e) for each month indicate in sequence the equivalent days of clear sky (white bar) and missing data (black bar); (b), (d), and (f) for each month indicate in sequence the equivalent days of scattered (gray bar), broken (speckled bar), and overcast sky (black bar). The years studied are 1991–1993 and 1997–1999.

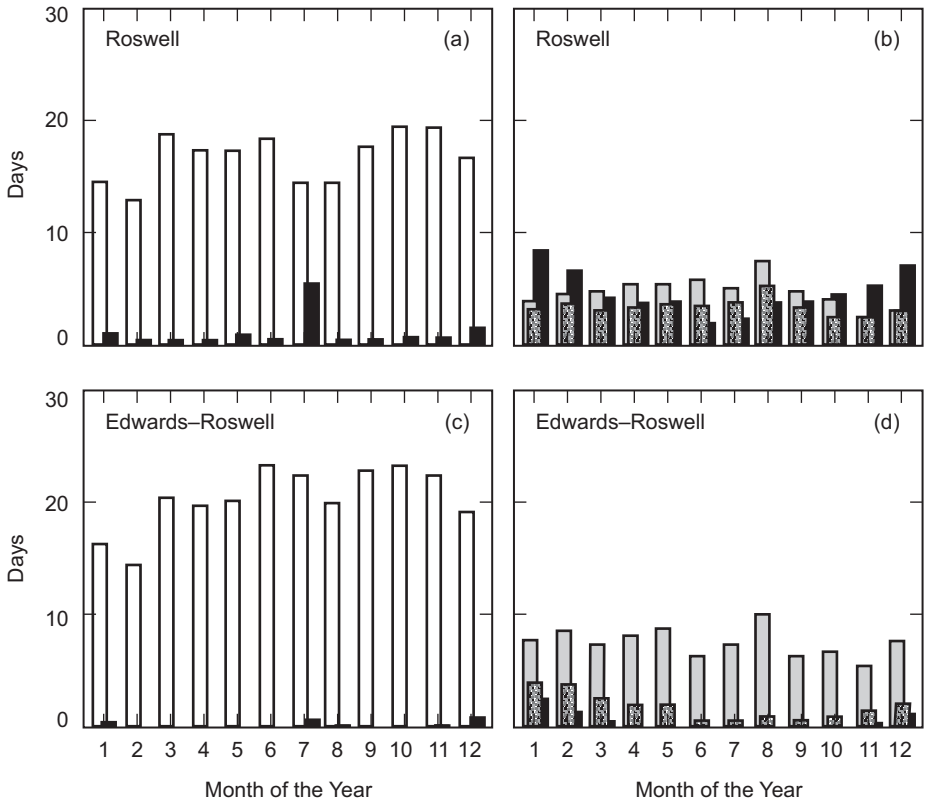

Fig. 3-7. Average monthly cloud coverage: comparison among one-site Edwards, one-site Roswell, and two-site diversity for combined Edwards and Roswell. February is averaged over 28 days: (a) and (c) for each month indicate in sequence the equivalent days of clear sky (white bar) and missing data (black bar); (b) and (d) for each month indicate in sequence the equivalent days of scattered (gray bar), broken (speckled bar), and overcast sky (black bar). The years studied are 1991–1993 and 1997–1999.

and Tucson improves the two-site diversity performances as seen in Fig. 3-3. For this last configuration, the average clear sky amount is 75.33 percent during a year with 19.52 percent scattered sky. However, if Edwards must be considered for three-site diversity, adding Roswell and Las Vegas gives the best contribution to enhance the clear sky statistics, with 77.54 percent.

Among the results analyzed here, the combination Daggett–Tucson–Roswell exhibited the best performance when considered for three-site diversity, producing a yearly clear sky amount of 81.24 percent with a scattered-sky amount of 13.34 percent.

Incidentally, one may notice in the Fig. 3-1 map that in this last configuration Tucson is symmetrically distant from the other two locations

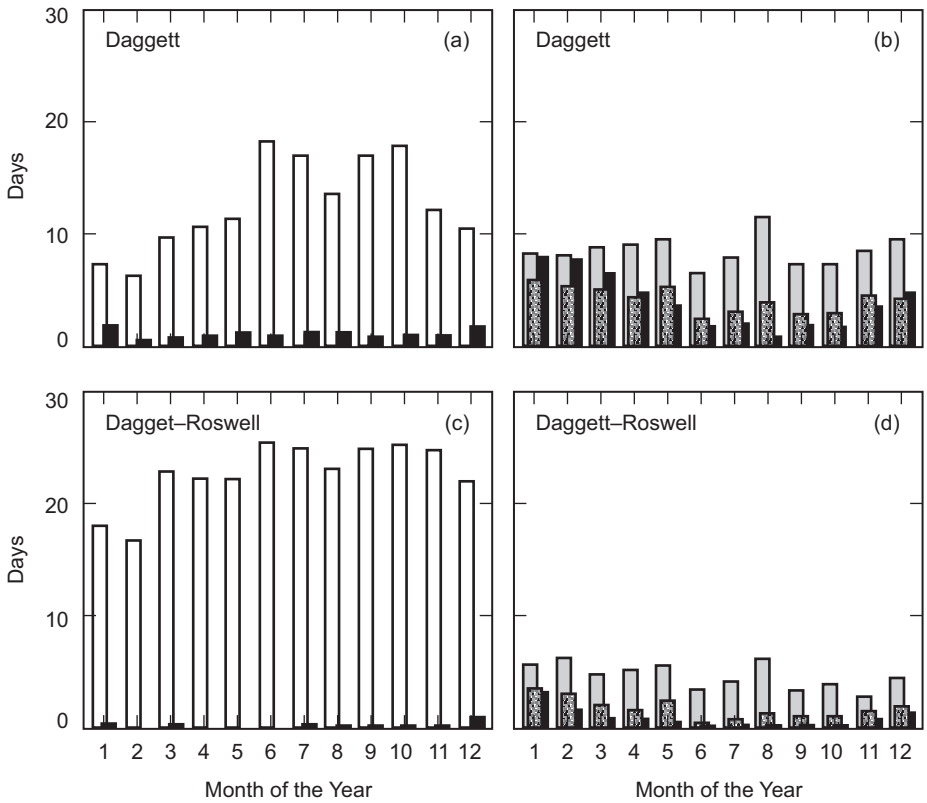

Fig. 3-8. Average monthly cloud coverage: comparison among one-site Daggett, one-site Roswell, and two-site diversity for combined Daggett and Roswell. February is averaged over 28 days: (a) and (c) for each month indicate in sequence the equivalent days of clear sky (white bar) and missing data (black bar); (b) and (d) for each month indicate in sequence the equivalent days of scattered (gray bar), broken (speckled bar), and overcast sky (black bar). The years studied are 1991–1993 and 1997–1999.

(each branch is of the order of 600 km). Moreover, all three locations were representative of three distinct climatic zones.

In this section we present results of monthly variations of cloud coverage for the same examples of three-site diversity analyzed in Fig. 3-10. One should hope, after selecting the proper locations for three-site diversity, to achieve extended durations of clear sky, with minimal monthly variation. For Edwards–Daggett–Tucson, a yearly variation of monthly amount for clear sky is still detectable, with relatively minimal amounts in January, February, and August, as seen in Fig. 3-11(a). During these months, the clear sky amount was in the range of 15–20 days. During the other months of the year it exceeded 20 days. For Edwards–Tucson–Roswell, the clear sky amount exceeded the 20 days with

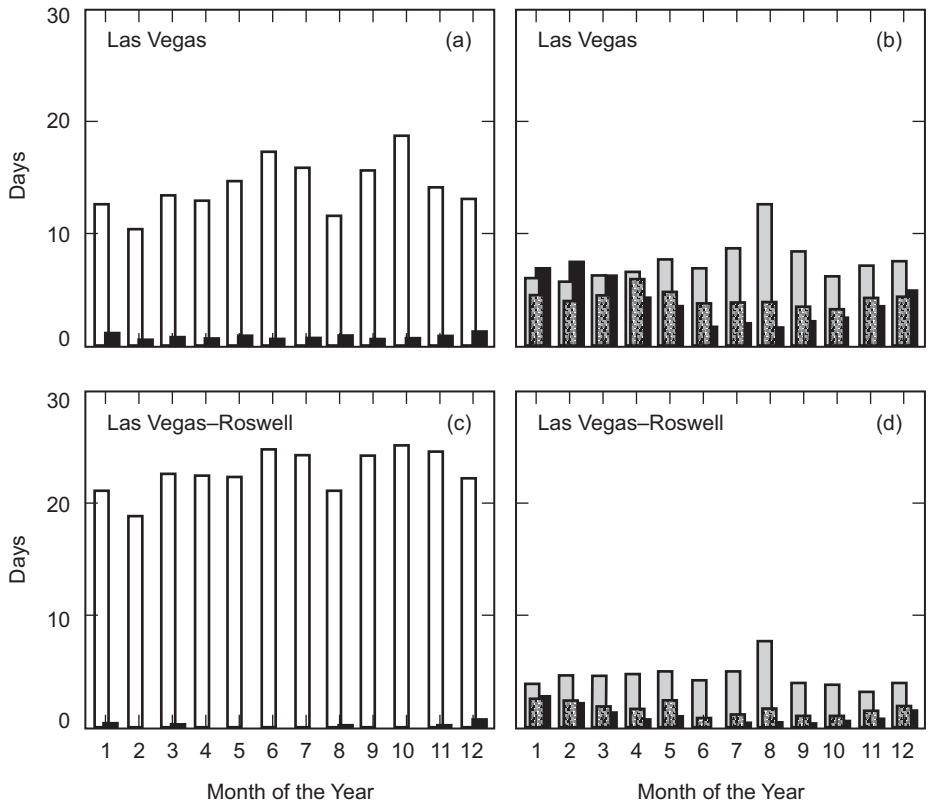

Fig. 3-9. Average monthly cloud coverage: comparison among one-site Las Vegas, one-site Roswell, and two-site diversity for combined Las Vegas and Roswell. February is averaged over 28 days: (a) and (c) for each month indicate in sequence the equivalent days of clear sky (white bar) and missing data (black bar); (b) and (d) for each month indicate in sequence the equivalent days of scattered (gray bar), broken (speckled bar), and overcast sky (black bar). The years studied are 1991–1993 and 1997–1999.

the exception of February (17 days). A reduction of the clear sky amount is detectable during August and the winter months, Fig. 3-11(b).

Monthly variation of the clear sky amount was less accentuated for Edwards–Las Vegas–Roswell, as seen in Fig. 3-11(c). In this configuration, February had only 19.11 days of clear sky amount (which, however, represented over 68 percent or the time during the month of 28 days), with the other months well beyond 20 days presenting a peak of 25.57 days in July.

The combination Daggett–Tucson–Roswell shows a similar trend of less variation, with an evident incremental increase of clear sky during the months of March, April, and May, Fig. 3-11(d).

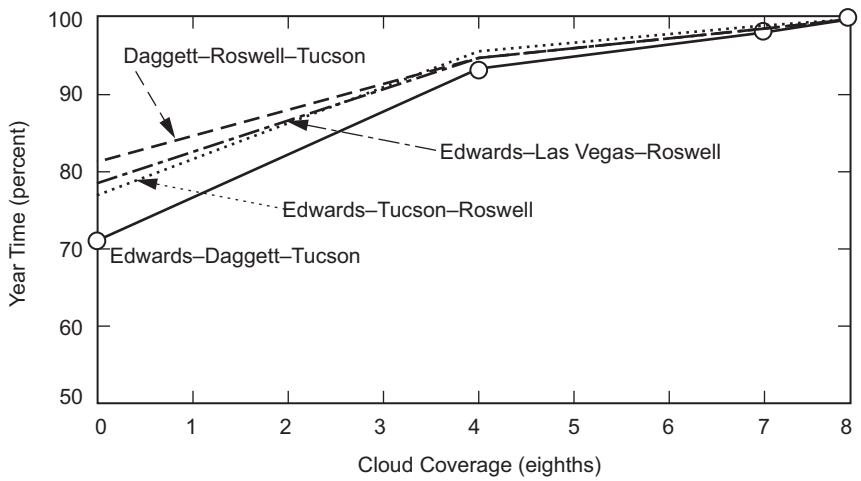

Fig. 3-10. Three-site diversity average cloud coverage statistics for Edwards–Daggett–Tucson (solid curve), Edwards–Tucson–Roswell (dotted curve), Edwards–Las Vegas–Roswell (dash-dotted curve), and Daggett–Roswell–Tucson (dashed curve). The years studied are 1991–1993 and 1997–1999. The piece-wise cumulative distribution curves are shown.

3.1.4 NCDC Analysis Conclusion

Using the surface observations, we were able to calculate a statistical representation of cloud coverage for single site, two-site diversity, and three-site diversity for the Southwest sites studied. Two-site diversity statistics clearly showed improvement over the single observation site statistics. By selecting a proper pair of sites among the 45 available combinations, we also demonstrated that two-site diversity statistics presented favorable periods of clear sky that were more uniform over the months when compared to single-site statistics. For instance, Las Vegas–Roswell, during the years 1991–1993 and 1997–1999, presented clear sky amount of about 75 percent as compared to the single site amount of 46.51 percent for Las Vegas and 55.03 percent for Roswell, Table 3-1.

Besides the overall improvement of the sky visibility, further analysis of data, also has shown that site diversity can be a robust solution against anomalies in the climate patterns that may affect the performance of a single telescope. To better explain this last concept, one may consider the hypothetical case of two telescopes: one located in the proximity of Edwards (e.g., Table Mountain) and the other in the proximity of Tucson (e.g., Mount Lemmon) during the year 1997. Table 3-1 indicates that on average one should expect a yearly amount 28.83 percent of clear sky at Edwards and 49.85 percent in Tucson. However, under the influence of “El Niño,” the cloud coverage in both locations greatly differed from the average that year. In fact, during 1997 at

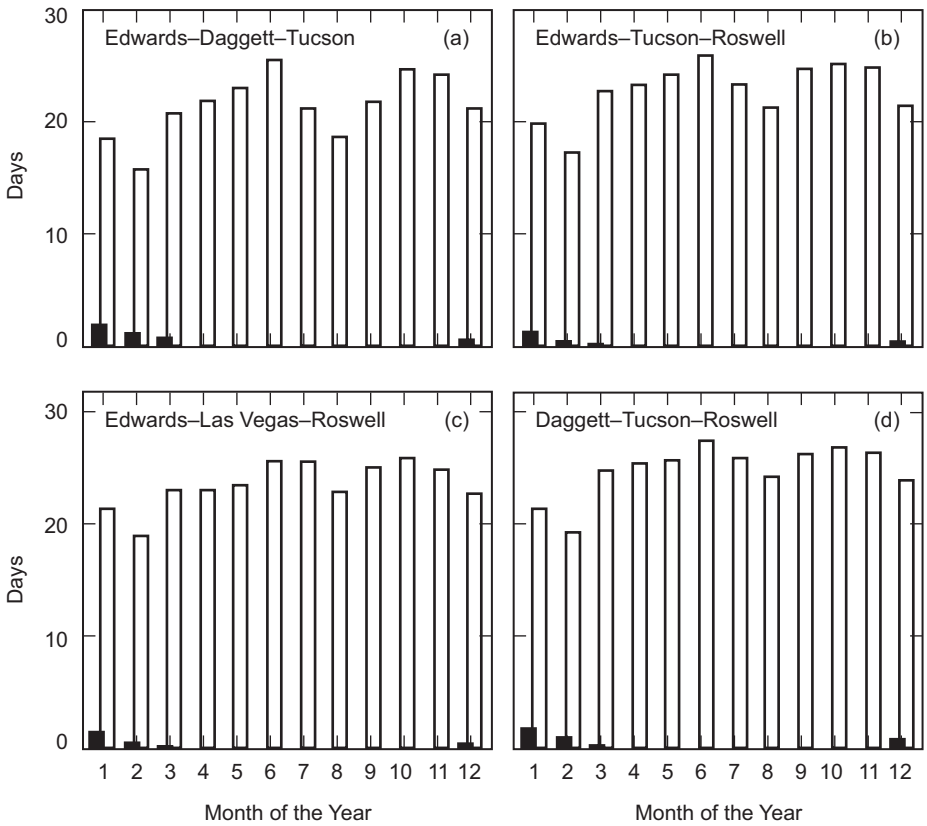

Fig. 3-11. Three-site diversity: average monthly clear sky for (a) Edwards–Daggett–Tucson, (b) Edwards–Tucson–Roswell, (c) Edwards–Las Vegas–Roswell, and (d) Daggett–Tucson–Roswell. February is averaged over 28 days. Bars indicate for each month in sequence the equivalent days of clear sky (white bar) and missing data (black bar) [5,6].

Edwards, only 19.39 percent of the time was the sky clear, while at Tucson the clear-sky amount was 61.36 percent, and the overall diversity clear sky was 66.9 percent. Therefore, the unusual climate pattern caused by El Niño affected the two locations in opposite ways; while the visibility for a telescope in the proximity of Edwards was greatly reduced, in Tucson the visibility was enhanced.

A further improvement with respect to two-site diversity is given by three-site diversity. For instance, statistics show that by adding Tucson (with 61.36 percent of yearly clear sky) to Las Vegas and Roswell, the clear sky amount is almost 80 percent compared to 75 percent for two-site diversity. The best overall results were observed for the triplet Daggett–Tucson–Roswell with 81.28 percent clear sky.

As a result of this investigation, one may notice that the average yearly clear sky amount improves on the order of tens of percent for two-site diversity over a single site for two properly selected locations. However, the additional improvement for three-site diversity compared with two-site diversity may not be as dramatic. System engineers should carefully evaluate the importance of a few percentage numbers in considering whether they can justify the expenses that the use of a third telescope would entail in order to reach a very high availability of the atmospheric channel at optical wavelengths.

Finally, among the sites characterized here, it was not possible to observe an amount of clear sky close to 100 percent in any (single, two-site diversity, or event three-site diversity) configuration. This result suggests that the study presented here based upon NCDC surface observation data be further expanded to other areas of the United States to find if this 100 percent limit of yearly clear sky is achievable by site diversity.

The approach in studying Earth cloud coverage using surface observation data, as proposed in the previous section, has a number of inherent advantages. The NCDC data bank has an extensive historical archive (decades). The data are readily available from the NCDC, and the observation stations are distributed all over the world (with a great emphasis on the continental United States). However a number of drawbacks are evident too. It is not possible to pinpoint a specific site on Earth, except by serendipitous coincidence with one of the observation stations. Observation stations are usually located at airports and not on mountain peaks. Moreover, the surface-observed data are prone to subjectivity of the observer and are at best qualitative. Finally, the number of stations is greatly reduced in the Southern Hemisphere.

3.1.5 Cloud Coverage Statistics by Satellite Data Observation

Satellite imaging measurements offer a more quantitative complement to surface observations. The satellite images acquired at different wavelength bands (both in the visible and in the infrared) are processed to extract spatial distribution of water vapor concentration in the atmosphere and therefore on the presence of clouds. The measurements are broadcast to Earth and distributed. The spatial distribution of clouds (water vapor) is determined using algorithms that perform a series of threshold tests. Over time, it is possible to provide cloud coverage statistics over the region that is imaged by the satellite. The spatio-temporal resolution of this approach is determined by the pixel angular FOV and the frequency at which images are acquired.

The remainder of this section, summarizes results of a study performed by TASC Inc. [3,8,9] on cloud-coverage statistics based on images collected by GOES9, METEOSAT-5, and METEOSAT-7 satellites. The spatial resolution is 5 km, and the temporal resolution is one hour. The averages span from

71.3 percent for Goldstone (California) to 55.29 percent at Starfire Optical Range (New Mexico).

The sites targeted in this study have astronomical observatories or NASA facilities that may be dedicated to space-to-ground communication. The sites chosen were concentrated in the United States Southwest, namely: Goldstone, Mount Wilson, Mount Palomar, and Table Mountain in California; Kitt Peak, in Arizona; Starfire Optical Range, in New Mexico (SOR); McDonald Observatory in Texas; and Mount Haleakala and Mauna Kea in Hawaii. The site altitudes vary from 1 to 4 km with the lowest being at Goldstone and the highest at Mauna Kea. Figure 3-12 shows the average yearly percentage of clear sky for the study sites.

The satellite study emphasized site-diversity statistics to determine link availability for a network of four sites among those considered. In other words, given the four sites distributed among the selected locations, what would the link availability be to any one of these four sites. Particularly, the case of a network of four telescopes supporting a deep space mission from Mars was considered. The determination of the cloud-free-line-of sight (CFLOS) took into account the angular variations on the plane of the ecliptic of Mars and Earth during the mission. It was found that a network of telescopes located in Goldstone, Kitt Peak, McDonald Observatory, and Mauna Kea yielded the best results in terms of availability. This is depicted graphically, based on data acquired from 1997–2002, in Fig. 3-13(a). Apparent in these data is a general evidence of seasonal variability of CFLOS between a spacecraft in Mars orbit and the selected ground stations. For all years with the exception of 1998,

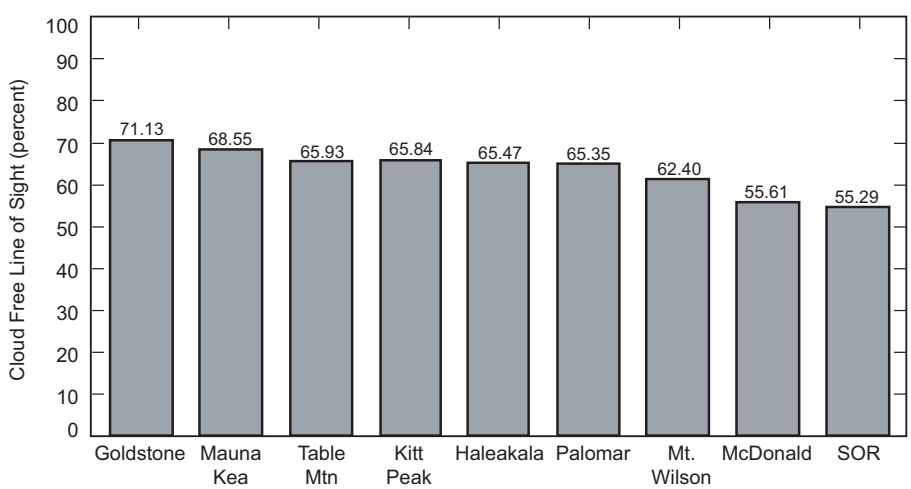

Fig. 3-12. Average yearly percentage of clear sky for the sites considered by the study. (SOR is an acronym for Starfire Optical Range facility.) The data are representative of six years of observations (1997–2002).

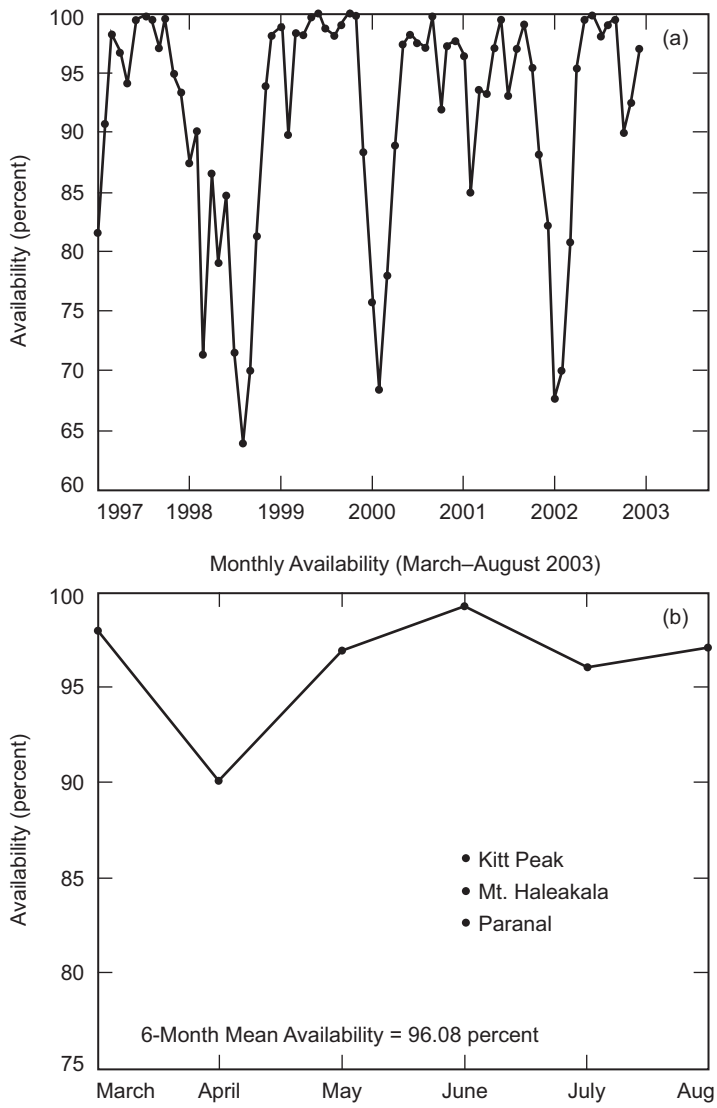

Fig. 3-13. (a) Average yearly percentage of clear sky for a network of four sites in spatial diversity. This combination of sites, Goldstone, Kitt Peak, McDonald Observatory, and Mauna Kea, gives the best results of CLFOS. The data are representative of six years of satellite observations (1997–2002). (b) 6-month statistics including a Southern-Hemisphere site (Paranal, Chile) shows the possibility of enhancing overall availability in a ground-based optical network.

winter and early spring availabilities are 70–80 percent increasing to 95–100 percent during the remainder of the year. The exception is 1998 because an El Niño condition occurred that year, which does not conform to this trend, showing nearly year-round relatively poor availability of 65–90 percent. Note that only Northern Hemisphere sites were considered in the data set presented. The overall network availability can be greatly enhanced by including Southern Hemisphere sites. The benefits would be twofold, namely, summer skies with better availability for the Southern Hemisphere sites as well as possible longer passes of the spacecraft including higher elevation angles. The long term statistical data to prove the better availability had not been analyzed at the time of writing this text. However, a proof of concept analysis based on a six-month period of cloud cover analysis using three sites (namely, Kitt Peak, Arizona; Mt. Haleakala, Hawaii; and Paranal in northern Chile) yield an overall 96 percent availability, as shown in Fig. 3-13b.

3.2 Atmospheric Transmittance and Sky Radiance

3.2.1 Atmospheric Transmittance

To quantify laser beam attenuation experienced by an optical communications link, one can introduce the concept of optical depth τ. The power reaching the receiver P_r is related to the transmitted power P_t [10] as

$$P_r = P_t e^{-\tau} \tag{3.2-1}$$

The fraction of the power transmitted in the optical link, T, is called transmittance and is given by

$$T = \frac{P_r}{P_t} = e^{-\tau} \tag{3.2-2}$$

The atmospheric transmittance and the optical depth are related to the atmospheric attenuation coefficient γ and the transmission path length r by

$$T = e^{-\int_0^r \gamma(\rho) d\rho} \tag{3.2-3}$$

and

$$\tau = \int_0^r \gamma(\rho) d\rho \tag{3.2-4}$$

where the atmospheric attenuation coefficient is laser-wavelength specific and depends on the path-integrated distribution of atmospheric constituents along

the line-of-sight. From the above equation, one can define the loss L in decibels that the beam experiences as

$$L = -10\log_{10} T = 4.34\tau \qquad (3.2\text{-}5).$$

An optical depth of 0.7, therefore, corresponds to a loss of 3 dB, or 50 percent of the signal power.

Generally speaking, the atmospheric attenuation coefficient can be expressed as the combination of absorption and scattering of the light beam due to gas molecules and aerosols present in the atmosphere:

$$\gamma = \alpha_m + \beta_m + \alpha_a + \beta_a \qquad (3.2\text{-}6)$$

where α_m and α_a are respectively the absorption coefficient for the molecular gas and aerosol, and β_m and β_a are the scattering coefficient for the molecular gas and aerosol. One should notice that although both absorption and scattering contribute to the attenuation coefficient, their attenuation mechanism is quite different. When a light beam propagates through the Earth atmosphere, it may interact with the gases and be absorbed. A light photon is absorbed when the quantum state of a molecule is excited to a higher state of energy. Specific states of energy absorb light at specific wavelengths with narrow line widths. The absorbed energy may be released at different wavelengths or as heat. During elastic scattering, there is no loss of energy at that determined wavelength. Instead the scattered light is redirected (at the same wavelength) into the total solid angle, with an effective loss along the propagation direction of the light beam. Scattering not only degrades the propagation of a signal beam in the atmosphere, but it is also the origin of the background sky radiance that introduces noise in a day-time communications downlink operation (sky radiance is discussed later in this chapter). Generally, scattering can be classified according to the size of the scattering particle and the wavelength: if the scattering particle is smaller than the wavelength the process is termed Rayleigh scattering [11]; if the size of the scatterer is comparable to the wavelength, it is termed Mie scattering [12]. Commonly, one may observe that molecular scattering is due to Rayleigh scattering while aerosol scattering is better described by Mie theory. When the size of the scatterers is much larger than the wavelength in consideration, diffraction theory can describe the scattering of light in a more proper fashion.

3.2.2 Molecular Absorption and Scattering

The Earth atmosphere is a combination of different gases [13]. The main constituents of the atmosphere are nitrogen (N_2) with 78.09 percent and oxygen (O_2) with 20.95 percent. Tables 3-2 and 3-3 summarize some data regarding gaseous composition of Earth troposphere.

Table 3-2. Main gases composing the Earth atmosphere.

Constituent	Volume Ratio (%)	Parts Per Million (ppm)
Nitrogen (N_2)	78.09	
Oxygen (O_2)	20.95	
Argon (Ar)	0.93	
Carbon dioxide (CO_2)	0.03	
Water vapor (H_2O)		40–40,000
Neon (Ne)		20
Helium (He)		5.2
Methane (CH_4)		1.5
Krypton (Kr)		1.1
Hydrogen (H_2)		1
Nitrous oxide (N_2O)		0.6
Carbon monoxide (CO)		0.2
Ozone (O_3)		0.05
Xenon (Xe)		0.09

Table 3-3. Earth atmospheric composition at sea level (10^{13} mb pressure and 300 K temperature).

Components	Mixing Ratio	Fraction in Mass	Mass Density (g/m^3)	Number Density (cm^{-3})
N_2	78.09%	76.50%	986.9	2.1×10^{19}
O_2	20.955	21.97%	283.7	5.7×10^{18}
Ar	0.93%	1.30%	16.8	2.6×10^{17}
H_2O	~1%	~0.63%	~8.1	$\sim 2.7 \times 10^{17}$
CO_2	400 ppm	615 ppm	0.8	1.1×10^{16}
CO	0.2 ppm	0.2 ppm	2.6×10^{-4}	5.6×10^{12}

Of course, the composition of the Earth atmosphere can vary with location on Earth and altitude over sea level. For instance water vapor density is larger in tropical areas and quite sparse in desert regions. In proximity to industrial areas and urban centers, the concentration of densities of carbon dioxide, carbon monoxide, ozone, and pollutants are relatively high. Finally, the density of Earth's atmosphere decreases with increasing altitude, as represented in

Fig. 3-14, with a resulting less severe interaction between a propagating optical beam and the atmospheric channel.

As stated earlier, photons (energy) absorbed by atmospheric molecules change the rotational, vibrational, electronic, or all of these energy states for the molecules. These molecular energy states are quantized and selected (bands of) wavelengths that are absorbed. Resulting from this quantized molecular absorption is a peculiar transmittance spectrum of the atmosphere with "forbidden bands" where the absorption loss is close to 100 percent. Figure 3-15 shows the atmospheric transmittance spectrum from which one may choose wavelengths of interest for optical space communication in the range 0.5–2 μm. Figure 3-15 describes the transmittance of the atmosphere for an observer (or a link) viewing local zenith (900 of elevation). The graph was obtained using MODTRAN 4.0 [15]. MODTRAN simulation results are used in this chapter both to obtain a measure of the atmospheric transmittance and background sky radiance under different condition of ground station altitude, aerosols distribution, meteorological visibility, etc. In particular, Fig. 3-15 simulates the transmittance spectrum experienced by a space-to-ground link with a telescope/transmitter at sea level looking at the zenith, at a mid-latitude location on Earth, with no aerosol concentration. Therefore, the spectrum described is generated only by molecular absorption and scattering (the action of aerosols is described in the next subsection).

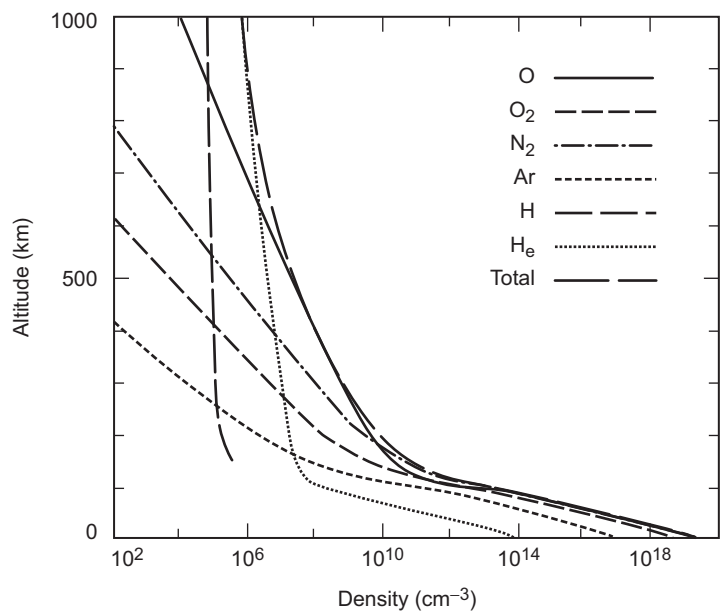

Fig. 3-14. Earth atmospheric number density profiles for individual species.

One may notice that Fig. 3-15 shows that a number of forbidden bands for laser propagation, mainly these around 0.7, 0.8, 0.96, 1.1, 1.38, and 1.9 μm. These forbidden bands are associated mainly with water vapor interactions [15] while oxygen and carbon dioxide have relatively weaker absorption lines in this range. By contrast, attenuation in the visible region of the spectrum is due to Rayleigh scattering [16]. The absorption coefficient of the Rayleigh scattering shows a functional dependence with the wavelength λ as λ^{-4}, clearly indicating a larger attenuation in the blue range (~0.425 μm) of the visible spectrum, a much smaller attenuation in red (~ 0.600 μm), and practically negligible attenuation for wavelengths in the infrared. Incidentally, this functional dependence of Rayleigh scattering wavelength dependence manifests itself with the scattering of the sunlight and the corresponding blue color of the sky.

Finally, the zenith transmittance spectrum of Fig 3-15 can be conveniently scaled at different observation angle. If we define as T_0 the transmittance at the zenith, one can easily calculate the transmittance T_θ at observation zenith angle θ as

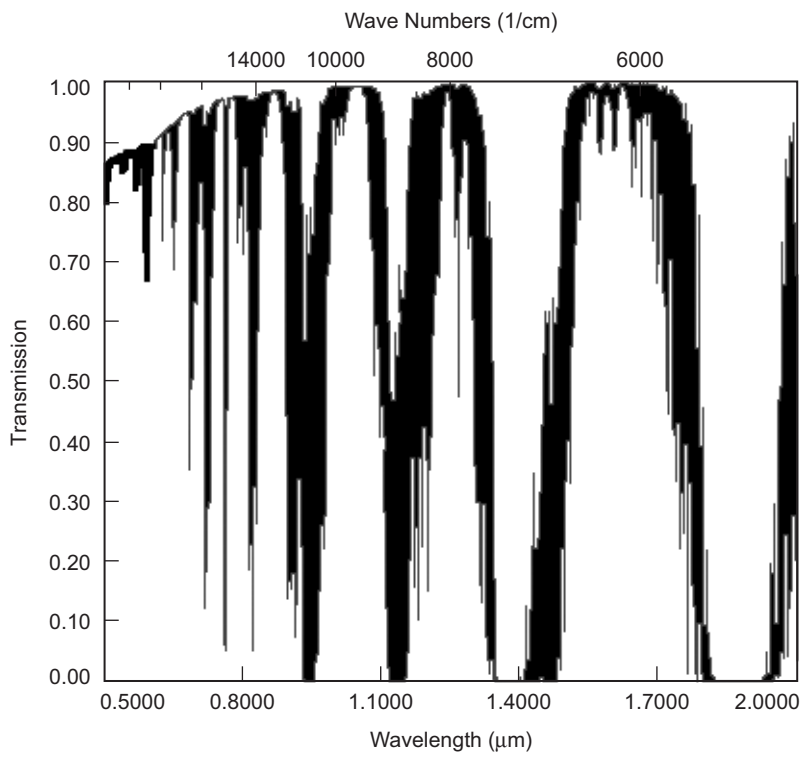

Fig. 3-15. Transmittance spectrum at sea level with zenith angle of zero. The plot is representative of a mid-latitude site on Earth with a hypothetical absence of aerosols.

$$T_\theta = T_0^{\sec(\theta)} \tag{3.2-7}$$

with the above relationship valid up to $\theta = 70°$ without loss of accuracy. The term "sec(θ)" is also referred to as airmass.

3.2.3 Aerosol Absorption and Scattering

Aerosols are atmospheric particles spanning a wide variety of constituents including dust, organic material, pollutants, ice, water droplets etc. Aerosol sizes can vary from sub-micrometer to a few tens of micrometers, and so its shapes (from spherical to irregular). Aerosols differ in distribution, components, and profile concentration in the atmosphere [17]; consequently, they influence the interactions with propagating laser beams in different ways (i.e., absorption and scattering). The largest concentration and variability of aerosols can be located in a boundary layer up to 1–2 km immediately above the Earth surface. Aerosols in the boundary layer are generally classified as maritime, rural, urban, and desert model [10]. Maritime aerosols are in the proximity or over the sea and ocean surfaces, and they typically consist of salt particles in aggregation with water droplets. Over land (distant from industrial settings), the rural model usually describes aerosol composition. Generally, aerosol composition of the rural model consists of dust particles and other substances (sulfates, organic materials originating from local flora) mixed with water droplets. Again, composition, density, and particle size distribution of aerosols belonging to the rural model vary with vegetation, land composition, weather dynamics, and seasonal climate variations. Manmade aerosols, those produced by industrial sources and other typical byproducts of urbanization (combustion, pollution, etc.), contribute to the urban model of the aerosol profile in the boundary layer. In the desert model, aerosols are mainly airborne dust particles, and their concentration mainly depends on wind speed. Above the boundary layer, aerosol concentration decreases in an exponential fashion until air convection and other atmospheric mixing mechanisms cause a globally uniform distribution of aerosols (independent of the sources in the boundary layer). With further increase in altitude, a region in the stratosphere between 10 and 20 km is reached, where particulate matter is essentially composed of sulfates and other products related to photochemical reactions with particles injected into the troposphere during volcanic eruptions [18,19]. This volcanic dust concentration is generally constant in time; however, the composition can change during episodes of volcanic eruption with further injection of volcanic dust that is usually dispersed in a few months. Above 30 km altitudes, aerosols are composed by meteoric and cometary dust.

The aerosol refraction index is described by a real and imaginary part (related to the material conductivity) as:

$$n_a = n_r - jn_i \tag{3.2-8}$$

aerosol absorption coefficient is related to the imaginary part of the refraction index as

$$\alpha_a = \frac{2\pi}{\lambda} n_i \tag{3.2-9}$$

A detailed list of the complex refraction index for a number of aerosol species can be found in [10].

Mie scattering theory describes scattering by aerosols [12]. Generally, according to the Mie theory, the scattering coefficient of aerosols depends on the particle concentration, size distribution, cross-section, and radiation wavelength. Detailed discussions of Mie scattering theory are beyond the scope of this work. However, to simply describe the action of aerosol Mie in the atmosphere, it is convenient to use the following practical relationships commonly used to describe the scattering coefficient, β_a, in horizontal path with constant aerosol concentration:

$$\beta_a = C_1 \lambda^{-\delta} \tag{3.2-10}$$

where C_1 and δ are constants [10,19] determined by aerosol characteristics (density, particle size distribution) and λ is the wavelength of interest in micrometers. The constant δ is related to the atmospheric visibility and varies from 1.0–1.6 (from poor visibility to clear line-of-sight). The constant C_1 is related to the visual (or meteorological) range V (in kilometers) as

$$C_1 = \frac{3.91}{V}(0.55)^{\delta} \tag{3.2-11}$$

where the visual range is referred to 0.550 μm [20]. The scattering coefficient therefore becomes

$$\beta_a = \frac{3.91}{V}\left(\frac{\lambda}{0.55}\right)^{-\delta} \tag{3.2-12}$$

where the wavelength is indicated in micrometers. Typical values of visual range are 5 km for hazy sky (high concentration of aerosol) and 23 km for clear sky. It is interesting to note, that despite an order of magnitude lower aerosol concentration compared to molecular gas concentration, aerosol scattering dominates Rayleigh scattering in the region of interest for optical communications wavelengths (0.5–2 μm).

Practical examples of the atmospheric transmittance dependence on aerosol concentration for a ground-to-space zenith pointing optical path are shown in Figs. 3-16 to 3-21.

Several interesting observations can be derived from these figures. For simplicity, all of these MODTRAN-generated plots are restricted to the case of rural aerosol model and location at mid-latitudes in the Northern Hemisphere during summer.

Figures 3-16 to 3-18 apply to 23-km visual range at different altitudes starting with sea level in Fig. 3-16. It is already evident, by comparing Fig. 3-16 to Fig. 3-15 describing the case of "aerosol free" atmosphere, that the atmospheric transmittance is reduced even with relatively benign high-visibility aerosol distribution. Of course, to mitigate the effects of aerosol concentration, telescope sites are usually located at higher elevation, so that the impact of the aerosols in the boundary layer is greatly reduced and the channel transmittance increased. Considering, for instance, the wavelength of 1 μm, Figs. 3-17, and 3-18, show the improvement in zenith atmospheric transmittance of 0.85 at sea-level to 0.93 at 2 km and 0.96 at 3 km. Note that at a 3-km altitude the

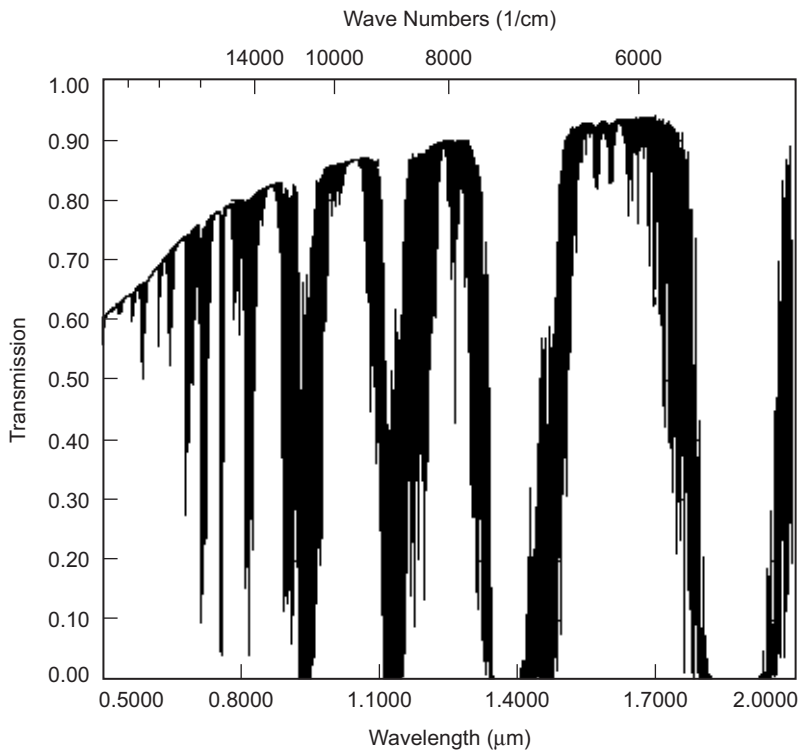

Fig. 3-16. Transmittance spectrum of the atmosphere for a space-to-ground link at sea level with zenith angle 0 deg, mid-latitude, 23 km of visual range.

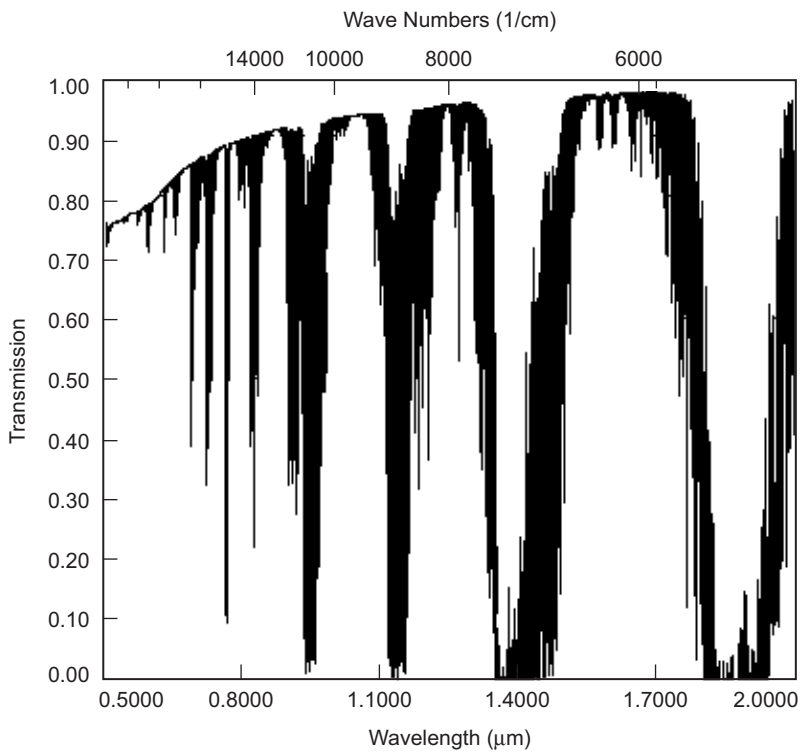

Fig. 3-17. Transmittance spectrum of the atmosphere for a space-to-ground link at 2 km of altitude with zenith angle 0 deg, mid-latitude. The boundary layer starts at 1 km with visual range of 23 km.

atmospheric transmittance starts becoming comparable to the no-aerosol case depicted in Fig. 3-15.

Figures 3-19, 3-20, and 3-21 describe hazy conditions at beginning of the boundary layer with visibility range at 5 km, again comparing sea level with 2- and 3-km altitude. For sea-level zenith transmittance, a wavelength of 1 μm (Figs. 3-19 and 3-16) is reduced to 0.60 from 0.85 or 1.7 dB and when scaled to 70 deg from zenith, this is nearly 4 dB worse (Eq. (3.2-7)). Figures 3-20 and 3-21 show a remarkable improvement in atmospheric attenuation with altitude assuming the beginning of the boundary layer is 1 km high. In fact, at 3 km altitude, the effect of aerosols has negligible impact on atmospheric attenuation at the wavelength of 1 μm (Figs. 3-21 and 3-18).

3.2.3.1 Atmospheric Attenuation Statistics. As shown above, MODTRAN can be effectively used to predict attenuation under a range of conditions that will be encountered during optical communication links through Earth's

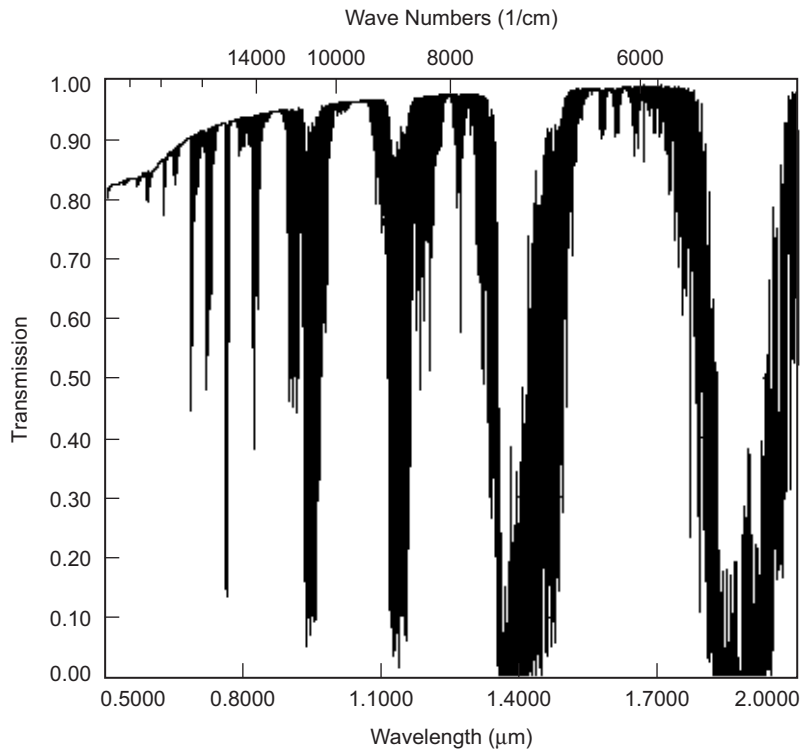

Fig. 3-18. Transmittance spectrum of the atmosphere for a space-to-ground link at 3 km of altitude with zenith angle 0 deg, mid-latitude. The boundary layer starts at 1 km with visual range of 23 km.

atmosphere. From an optical link design standpoint, what is not apparent from the model predictions is the statistical nature of the attenuation variations. How often actual atmospheric attenuation measurements will conform to one or the other kind of model assumptions is critical for designing and making long-term performance predictions for space-to-ground optical links. With this in mind, JPL initiated an Atmospheric Visibility Monitoring (AVM) program. The objective was to monitor the spectral attenuation through the atmosphere using stars as light sources observed through narrow bandpass optical filters. Currently the program is limited to use of silicon sensors and, therefore, measurements up to 1064 nm. At the time of writing this chapter, the state of knowledge is that statistics of atmospheric attenuation are available but purely in an empirical form. In general the AVM experience has been to obtain reliable day and nighttime data at the 860-nm band (10-nm wide), whereas with the 25-nm full-width half-maximum band centered at 1064 nm, mainly nighttime observations can be made since the silicon sensors decreasing response at 1064 nm yielded poor signal-to-noise for daytime measurements,

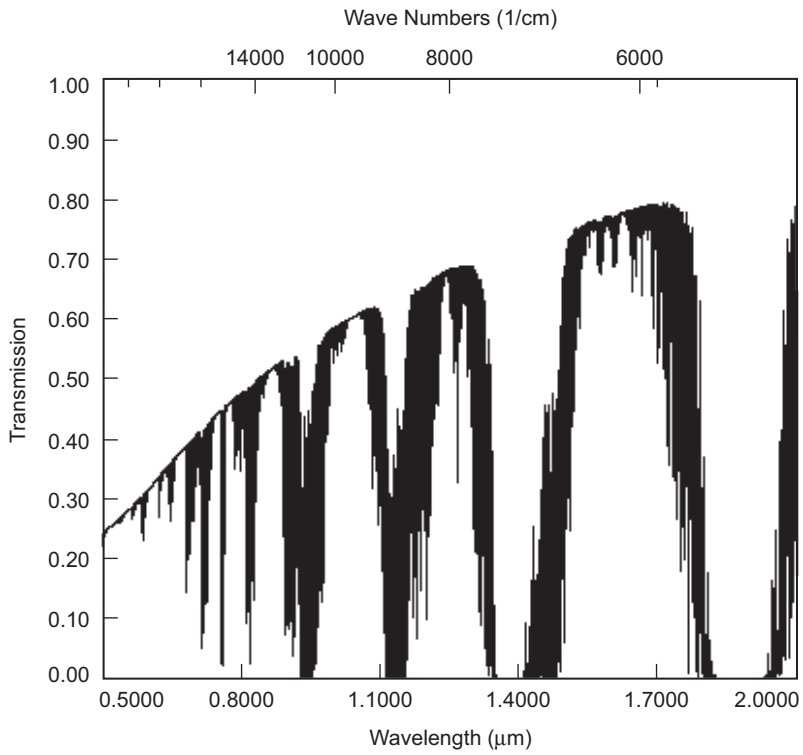

Fig. 3-19. Transmittance spectrum of the atmosphere for a space-to-ground link mid-latitude site at sea level with zenith angle 0 deg, and 5 km of visual range.

because of the increased background. Two tables of data (Tables 3-4 and 3-5) are reported below for 1064-nm and 860-nm reception, respectively. As stated, the 1064-nm results relate to nighttime only data, whereas the 860-nm data are relevant to daytime and nighttime data. The data presented in Tables 3-4 and 3-5 are almost all measured at the Table Mountain Facility (TMF), California, with just a single set of data shown for the Mount Lemmon (ML) observing station near Flagstaff, Arizona.

The site altitudes at TMF and ML are 2200 and 2800 m, respectively. Moreover, the cumulative probabilities apply to an airmass of 1. Table 3-5 shows that availability suffers during the first quarter months of January, February, and March due to increased cloud cover and precipitation associated with winter when it fell to as low as 40 percent availability. The remaining time availability was high, in the 60–80 percent range. Table 3-5 shows that wintertime availability at ML is better than at TMF. In general the observation can be made that the model predictions of benign (0.7-dB attenuation for the 23 km) visibility case at 2–3-km altitudes is borne out by the observations a very small fraction of time ranging typically from 15–30 percent of the time.

Table 3-4. Cumulative probabilities of atmospheric attenuation at 1064 nm (25-nm bandpass) for predominantly nighttime observations made with AVM at TMF.

Quarter	Station Uptime Fraction	<2 dB	<1.5 dB	<1 dB	<0.5 dB
Q3, 2002	0.33	0.8	0.79	0.73	0.15
Q4, 2002	0.62	0.62	0.6	0.56	0.45
Q1, 2003	0.85	NA	NA	NA	NA
Q1, 2003	0.4	0.62	0.58	0.5	0.2
Q2, 2003	0.85	0.73	0.73	0.7	0.4
Q3, 2003	0.7	0.68	0.65	0.53	0.4

Table 3-5. Cumulative probabilities of atmospheric attenuation at 860 nm (10-nm bandpass) for day and nighttime observations made with AVM at TMF.

Quarter	Station Uptime Fraction	<2 dB	<1.5 dB	<1 dB	<0.5 dB
Q3, 2002	0.33	0.87	0.83	0.78	0.35
Q4, 2002	0.62	0.65	0.62	0.58	0.35
Q1, 2003	0.85	0.4	0.35	0.25	0.05
Q1, 2003	0.4	0.5	0.46	0.45	0.27
Q2, 2003	0.85	0.83	0.8	0.75	0.4
Q3, 2003	0.7	0.81	0.72	0.53	0.2

From an optical-communications design standpoint, the statistics suggest designing links for 1-dB attenuation or equivalently 2.8 dB at zenith angles of 70 deg will cover 50–80 percent of the time across all seasons at any given station. The presumption here is that when conditions get worse there will be nearby sites in the network where the link will be switched to in order to achieve overall availability in the high 90s as discussed in the previous sections.

3.2.4 Sky Radiance

Just as atmospheric scattering deflects photons propagating from an optical communications transmitter to a ground receiver resulting in net signal loss, solar photons can be scattered in a manner that causes them to propagate along the transmit–receive line-of-sight path giving rise to unwanted background. The latter degrades the signal-to-noise ratio of the link. The extent of these daytime phenomena is dictated by the source geometry of the observer, the Sun, and the transmitting source. The exo-atmospheric solar spectral irradiance is shown in Fig. 3-22. Source irradiance describes the power emitted by a point source

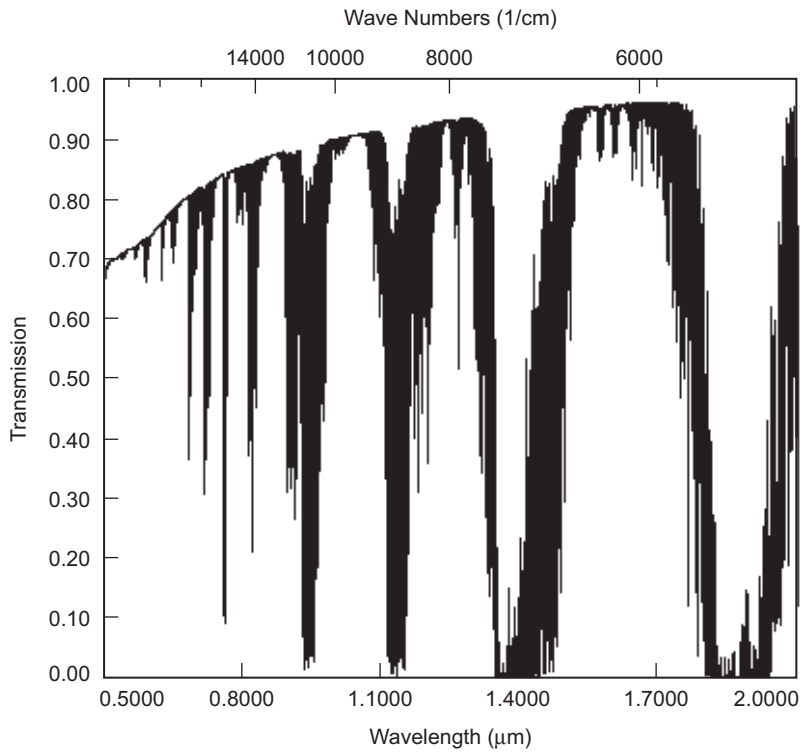

Fig. 3-20. Transmittance spectrum of the atmosphere for a space-to-ground link mid-latitude site at 2 km with zenith angle 0 deg. The boundary layer starts at 1 km with visual range of 5 km.

captured by unit area (receiver) over a spectral bandwidth, which in Fig. 3-22 is dimensionally W/(cm^2 μm).

Radiative transfer due to molecular and aerosol scattering in the atmosphere, and therefore the determination of the sky radiance, is not an easy problem to solve due to both the complexity of scattering theory and the fact that atmosphere is not a homogeneous medium, but instead it greatly varies with altitude. To simplify the problem, the atmosphere is modeled as a layered medium, with each layer consisting of a homogenous mixture of gas and aerosols. This concept is indicated in Fig. 3-23 where solar (S) radiation impinges on scatterer (P) and is redirected to an observer (O). In this figure the atmosphere is divided into a number of homogeneous layers (H_1, H_2, H_3…and so on), with the scattering angle γ between the forward direction of the Sun radiation and the observation point direction [21,22,23].

The basic premise of this model is to consider each single scatterer in a generic atmospheric layer, H_i, as a new scattering source of irradiance $J(\lambda)_i$

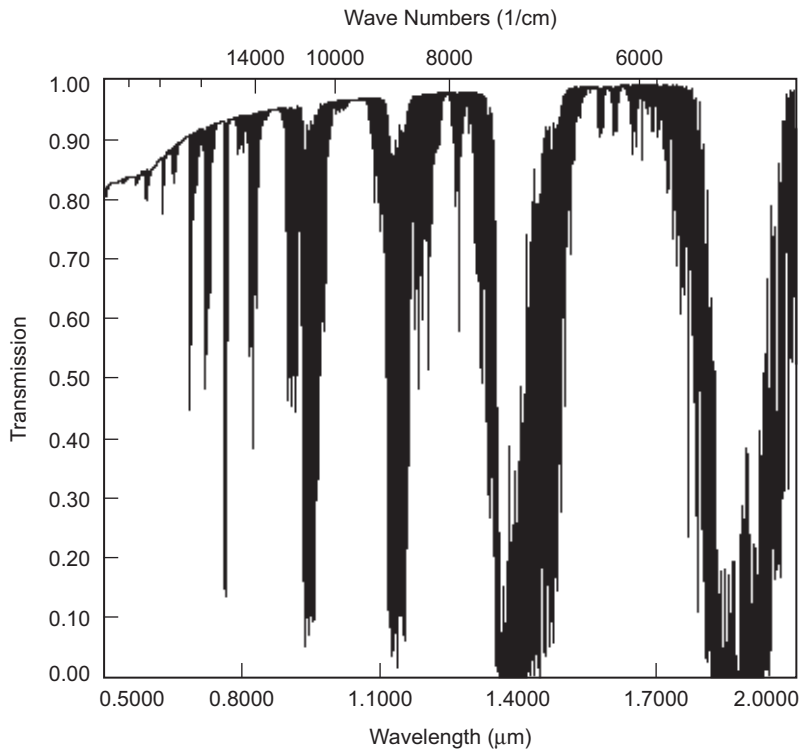

Fig. 3-21. Transmittance spectrum of the atmosphere for a space-to-ground link mid-latitude site at 3 km of altitude with zenith angle 0 deg. The boundary layer starts at 1 km with visual range of 5 km.

$$J(\lambda)_i = H_\lambda T_{sp}\left[p^a(\gamma)B_a + p^m(\gamma)B_m\right] \tag{3.2-13}$$

where H_λ is the exo-atmospheric Sun irradiance at the determined wavelength, T_{sp} is the atmospheric transmittance between Sun and the scatterer at the point P, while $p^a(\gamma)$ and $p^m(\gamma)$ are scattering phase functions for aerosol and molecular scattering describing the amount of energy scattered at the observer angle γ.

The total contribution from all the scattering source functions in the same atmospheric layer is therefore

$$L_i(\lambda,\theta,\varphi) = \int J(\lambda)_i T_{op} ds_{op} \tag{3.2-14}$$

where T_{op} is the atmospheric transmittance at the observation point represented by θ and φ, the observer zenith angle and angular distance between observer

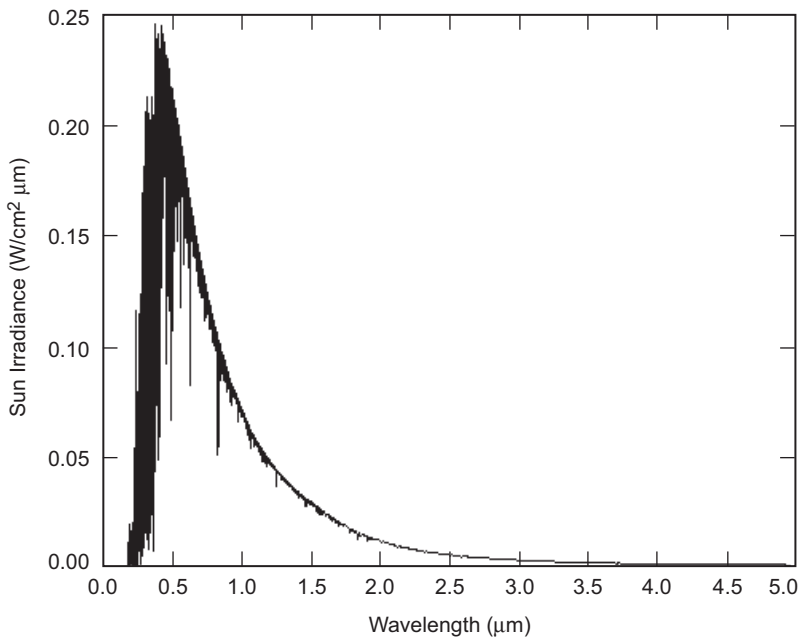

Fig. 3-22. Exo-atmospheric solar irradiance at 1 astronomical unit (AU).

and Sun zenith angles. The integral of Eq. (3.2-14) is defined over all the possible paths s_{op} between scatterer(s) and observation point. Finally, summing the contribution by all N atmospheric layers, one can get the total sky radiance [22,23]

$$L(\lambda,\theta,\varphi) = \sum_{j=1}^{N} L_j(\lambda,\theta,\varphi) \tag{3.2-15}$$

which dimensionally describes the power emitted by an extended source captured by unit area (receiver) over a spectral bandwidth at a given field of view, usually dimensionally is described as W/(cm^2 sr µm). Therefore, given a receiver aperture of diameter D cm, field of view Ω steradians, and $\Delta\lambda$ micron of bandpass filter, the total power P_{pbg} originated by sky radiance collected by the telescope is

$$P_{bg} = L(\lambda,\theta,\varphi)\frac{\pi D^2 \Omega \Delta\lambda}{4} \tag{3.2-16}$$

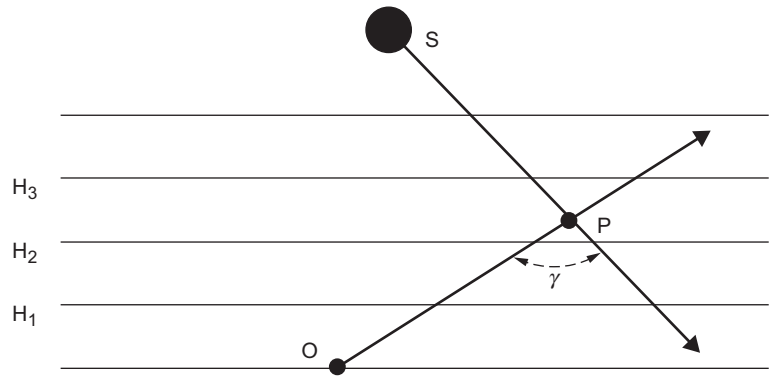

Fig. 3-23. Depiction of (single) scattering mechanism for a layered model of the atmosphere. S stands for the Sun (or any light source); P is the location of the aerosol; O is the observation point; γ is the scattering angle.

Scattering coefficients, phase functions, and transmittance vary greatly in the different atmospheric layers due to the diverse scatterer concentration.

To briefly summarize the consequences of Eq. (3.2-13) to Eq. (3.2-16), one may consider that:

- The higher the concentration of scatterers, the higher (generally, unless atmospheric transmittance is too low) is the sky radiance.
- The higher the altitude of the observer (telescope), the lower is the sky radiance because of lower concentration of scatterers.
- As the angular distance between observation direction and Sun decreases, (so does the scattering angle) the sky radiance increases.
- Sky radiance at small angular distance between observation direction and Sun φ is dominated by single scattering; however, with increased angular distance, the contribution of multiple scattering to sky radiance starts to dominate.
- Within 30 deg from the Sun, sky radiance is greatly dominated by aerosol contribution, as the angular distance from the Sun increases, molecular (Rayleigh) scattering, becomes more significant.

Figures 3-24 through 3-29 show sky radiance for different cases of telescope altitude and sky visibility over the spectrum of 500–2000 nm. For simplicity, we restricted the case of Sun zenith angle of 45 deg, the observer (telescope) zenith angle is instead at 10, 40, and 70 deg. The azimuth between observer and Sun is zero, and in all the cases, a rural aerosol model for a mid-latitude location during summer with observer location at sea level is assumed.

Figure 3-24 depicts the case of an observer at sea level. As clearly shown, the sky radiance is larger when the angle between the observation direction and the Sun is the smallest (5 deg). However, sky radiance is also large even when

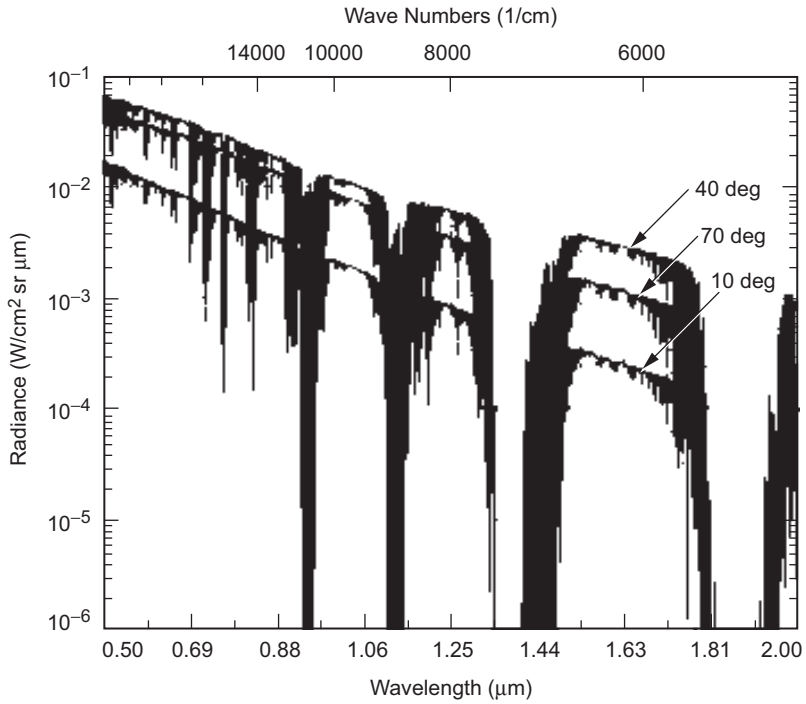

Fig. 3-24. Sky radiance spectrum experienced at an observation point at sea level for 23 km of visibility and Sun zenith angle of 45 deg while observer zenith angle varies as 10, 40, and 70 deg.

the observer angle is 70 deg. This is due to the fact that at a large zenith angle, the effective number of scatterers seen along the observation direction is larger. Figure 3-25 shows the sky radiance decrease upon raising observer location 2 km in altitude. Here the aerosol boundary layer is assumed to start at 1 km.

The reduction of sky radiance is due to the shorter path traversed by the light through the atmosphere, as well as, a smaller concentration of aerosols that scatter sunlight. Of course, such a reduction of the sky radiance is further accentuated at 3-km altitude, as seen in Fig. 3-26. Finally, for sake of completion, the same examples are repeated considering a visual range of 5 km (instead of 23 km) in Figs. 3-27 and 3-29. As expected, a larger aerosol concentration leads to larger sky radiance in Fig. 3-29, which corresponds to the case of 3-km altitude, showing that when the observer zenith angle is at 70 deg (30 deg from the Sun) the amount of sky radiance is larger than that one at 40 deg (5 deg from the Sun). This result, is related to the large difference in path integrated scatterer concentration along the two paths.

3.2.4.1 Sky Radiance Statistics. As discussed for atmospheric attenuation, the models presented in the preceding section are not indicative of sky radiance

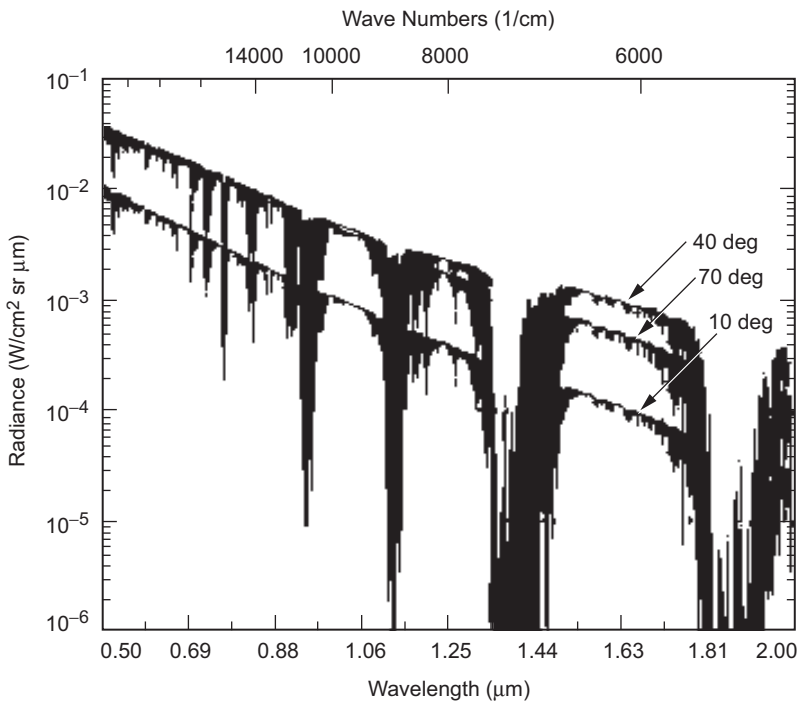

Fig. 3-25. Sky radiance spectrum experienced at an observation point at 2 km of altitude. The boundary layer starts at 1 km with a visual range of 23 km. Sun zenith angle is 45 deg while observer zenith angle varies as 10, 40, and 70 deg.

statistics as would be preferred by an optical communications systems designer. NASA has a global network of deployed Sun photometers that are used to monitor daytime sky radiance. This is known as the Aerosol Robotic Network (AERONET). The Sun photometers acquire sky radiance data in the course of extracting the aerosol optical thickness profiles. The sky radiance is reported in terms of principle plane and almucantar scans that provide a rich data set of sky radiance as a function of the position of the Sun in the sky. A few sets of data from this database were reduced in order to address sky radiance statistics at a few different sites.

Figure 3-30 shows a general comparison between the predicted and measured sky radiance at Table Mountain Facility (TMF), California. The sky radiance is presented as a function of Sun–Earth–Probe (SEP) angle. Noteworthy features displayed by Fig. 3-30 are the spread in measured sky radiance values at any give SEP angle. The measurements are over the period of a few months and are made at a wavelength of 1.026 µm for a zenith angle range of 55–60 deg. The spread is interpreted to be associated with a range of atmospheric conditions. The average of the measurements is shown by the

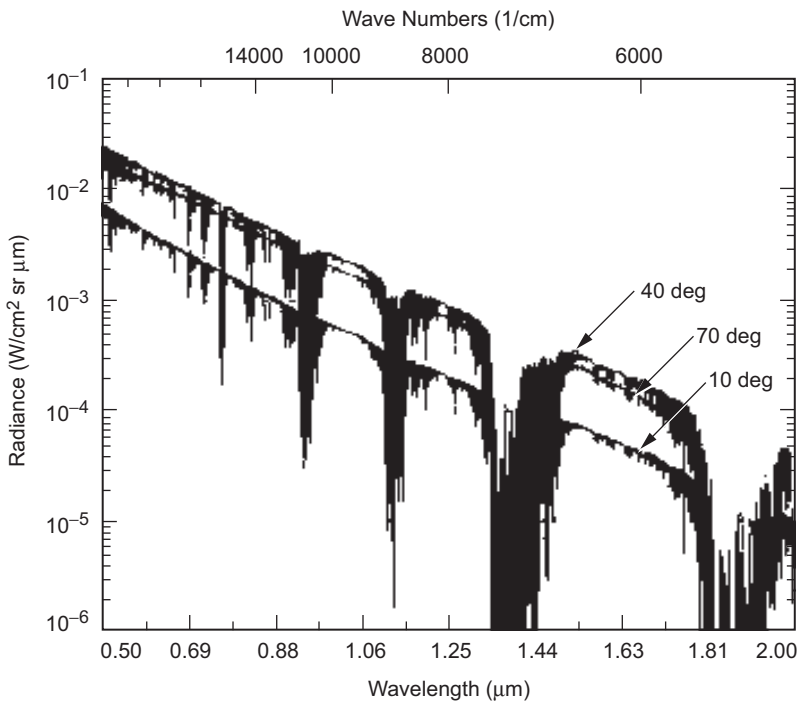

Fig. 3-26. Sky radiance spectrum experienced at an observation point at 3 km of altitude. The boundary layer starts at 1 km with a visual range of 23 km. Sun zenith angle is 45 deg while observer zenith angle varies as 10, 40, and 70 deg.

dotted line. A few MODTRAN sky radiance predictions for different aerosol and high cirrus cloud models at 1.064 μm are overlaid in Fig. 3-30. The comparison is reasonable.

While some evidence of the statistics is evident in Fig. 3-30, Fig. 3-31 shows cumulative distribution functions of sky radiance measured at TMF. The data are for SEP angles of 3 deg but for a few different solar zenith angles. Two separate data campaigns are represented, namely, data acquired in January–February of 2000 and then data acquired from June 2003–January 2004. The same calibrated instrument was used on the two separate occasions; however, the setup was dismantled and re-installed between the two data sets. Repeated in the data sets is the fact that for achieving any cumulative probability, larger zenith angles yield slightly lower sky radiance values, contrary to what the sky radiance models predict. For example, 50-percent cumulative probability at 65–70-deg zenith angle in the 2003 data set is 7×10^{-3} W/(cm^2 sr μm), whereas at the smaller zenith angle of 55–60 deg it is 1.5×10^{-2} W/(cm^2 sr μm). The same observation is generally true for the data gathered in 2000. The reason for departure from model behavior is not understood.

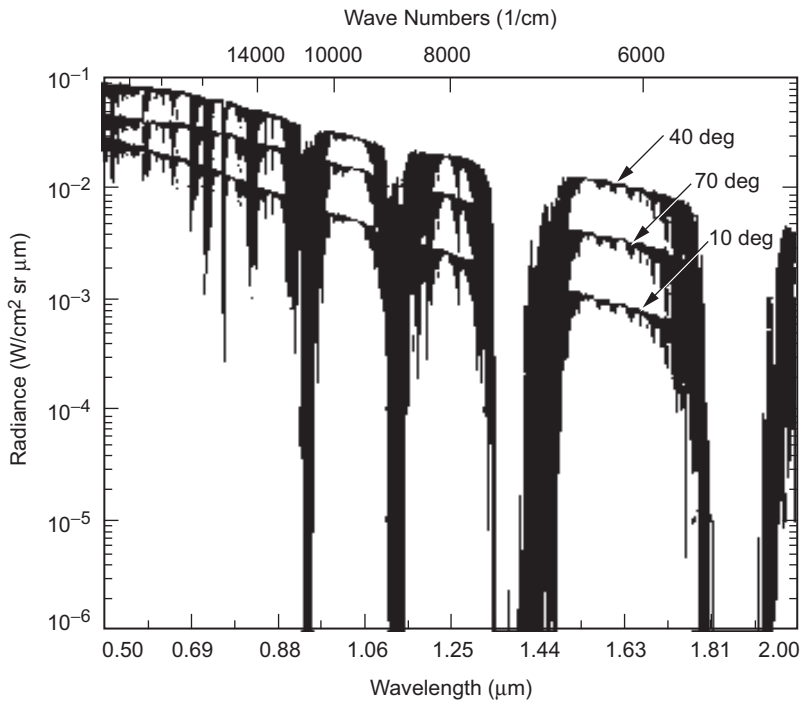

Fig. 3-27. Sky radiance spectrum experienced at an observation point at sea level with a visibility of 5 km. Sun zenith angle is 45 deg while observer zenith angle varies as 10, 40, and 70 deg.

Figure 3-32, on the other hand, shows data gathered at Roger's Dry Lake in California at an altitude of 680 m. In general, the sky radiances for this location appear to be higher than for TMF, consistent with the fact that it is located at a lower elevation. However, note that at Roger's Dry Lake the model behavior, namely larger sky radiance with zenith angle, is borne out.

3.2.5 Point Sources of Background Radiation

Sun-related sky radiance is the largest source of background noise that a telescope on Earth can collect pointing at a spacecraft. However, a telescope can also collect unwanted background light when (illuminated) planets or stars are in its FOV. These different sources of background radiations clearly need to be assessed in order to characterize the performances of a receiver.

In this subsection, therefore, we illustrate how to determine the background irradiance of a star of a given visual magnitude and temperature, and, later, the irradiance of a planet. To simplify, without lack of generalization, our discussion is limited to the case of absence of atmospheric interaction (e.g., a

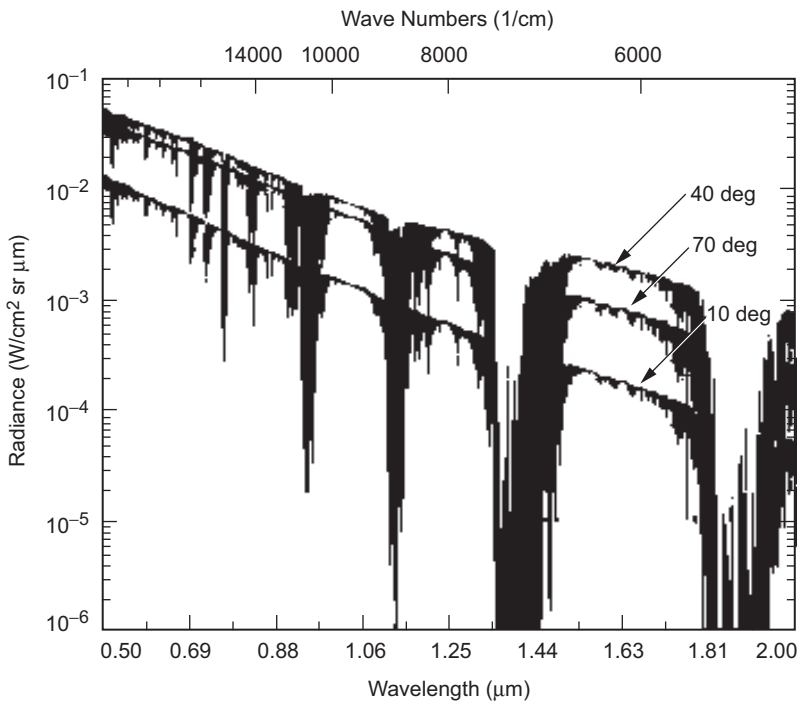

Fig. 3-28. Sky radiance spectrum experienced at an observation point at 2 km of altitude. The boundary layer starts at 1 km with a visual range of 5 km. Sun zenith angle is 45 deg, while observer zenith angle varies as 10, 40, and 70 deg.

receiver located aboard of spacecraft), while a comprehensive example (Mars in the FOV of a telescope on Earth) is shown at the end of this discussion.

Due to their small angular extension, stars (with the exception of the Sun) can be considered point sources because they are encompassed within a receiver FOV. To quantify the background light from a star, it is necessary to know the star's spectral irradiance S_λ. The star spectral irradiance defines the power collected by a receiver of a given collection area over a given spectral band (dimensionally W/m^3). Values of spectral irradiances for a number of stars can be found in Ref [24]. Otherwise, if the spectral irradiance of a star is not defined it can be calculated by knowledge of the radiation temperature T_s and its visual magnitude M_v. In fact, the spectrum of the star irradiance resembles (in shape) that of a black-body at given source temperature T_s such as

$$W(\lambda, T_s) = \frac{2\pi c^2 h}{\lambda^5} \frac{1}{\exp\left(hc / \lambda K T_s\right) - 1} \tag{3.2-17}$$

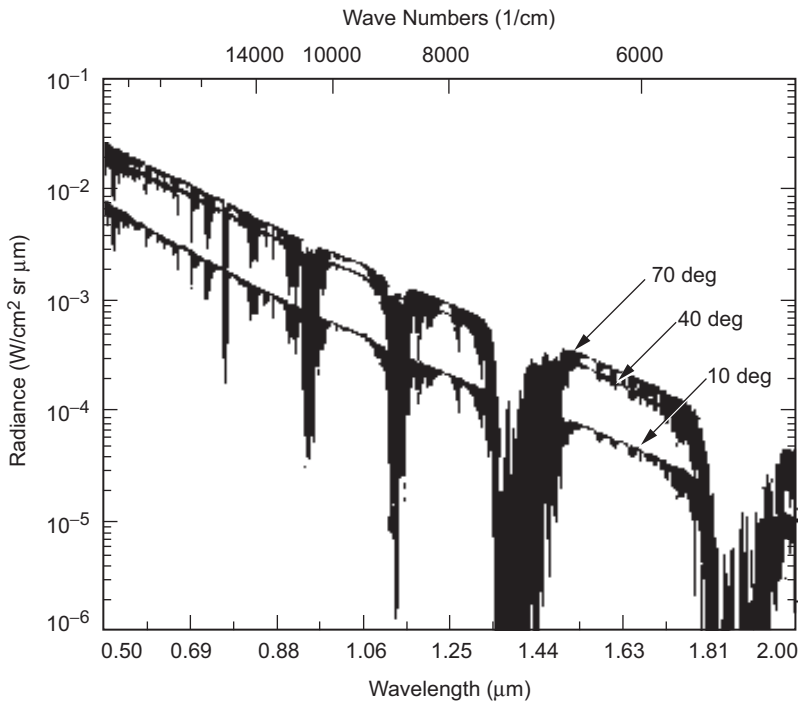

Fig. 3-29. Sky radiance spectrum experienced at an observation point at 3 km of altitude. The boundary layer starts at 1 km with a visual range of 5 km. Sun zenith angle is 45 deg, while observer zenith angle varies as 10, 40, and 70 deg.

where c is the speed of light in vacuo, h is Plank's constant, K is Boltzmann constant, and the blackbody emission is given in watts per meter. The spectral radiance emittance $W(\lambda, T_s)$ defines the power in Watts emitted by a square meter in the wavelength region $\lambda + d\lambda$. The wavelength in Eq. (3.2-17) is in meters. At its maximum value, $W(\lambda, T_s)$ and its corresponding peak wavelength λ_M are related to the source temperature as

$$\lambda_M = \frac{0.00289}{T_s} \tag{3.2-18}$$

where λ_M is in meters and T_s in kelvins. In essence, Eq. (3.2-17) teaches that given a star whose emission peaks at λ_M its spectral irradiance will be proportional to that one of a black body whose temperature T_s can be derived by Eq. (3.2-18). The proportionality constant that help us to calculate the star irradiance from the black body spectrum can be derived by the star visual magnitude.

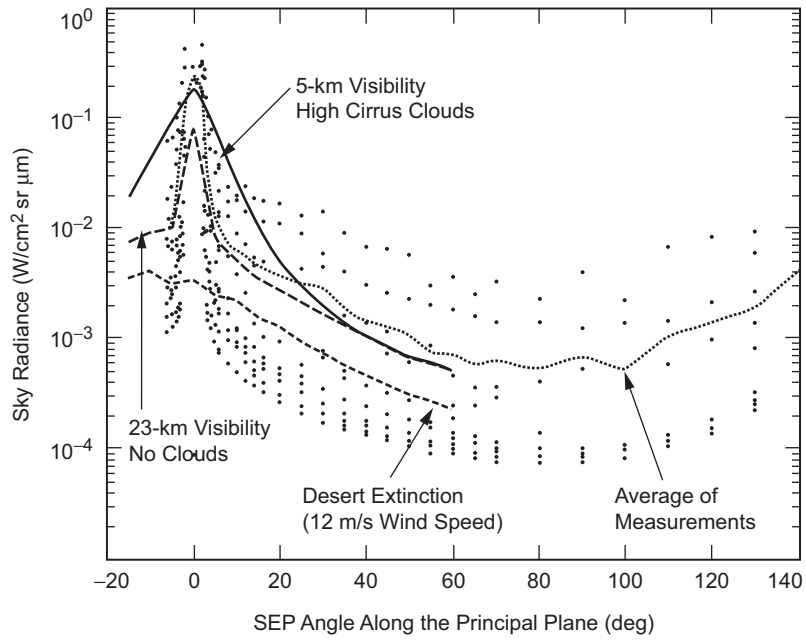

Fig. 3-30. A comparison between measured and predicted sky radiance as a function of SEP angle. The measurements (•) are at a wavelength of 1.02 μm and a zenith angle range of 55–60 deg. The solid lines are MODTRAN predictions for the indicated aerosol models at 1.064 μm.

The star visual magnitude M_v is a function of the star irradiance in the visible spectrum I_v defined as

$$M_v = -2.5\log_{10}\left(\frac{I_v}{3.1\times10^{-17}}\right) \tag{3.2-19}$$

where here I_v is in W/m^2. Using Eq. 3.2-17 to Eq. 3.2-19, it can be shown [24] that the star spectral irradiance of the can be written as

$$S_\lambda = 3.1\times10^{-\left(17+\frac{M_v}{2.5}\right)}\frac{W(\lambda,T_s)}{\int_0^\infty W(\lambda,T_s)e(\lambda)d\lambda} \tag{3.2-20}$$

where $e(\lambda)$ is the eye spectral response. The eye spectral response can be approximated by a triangular function that peaks $e = 1$ at 0.55 μm and is zero at 0.4 and 0.7 μm. Finally, one should notice that S_λ here is given in watts per square meter (of the receiver area) over the spectral bandwidth of interest.

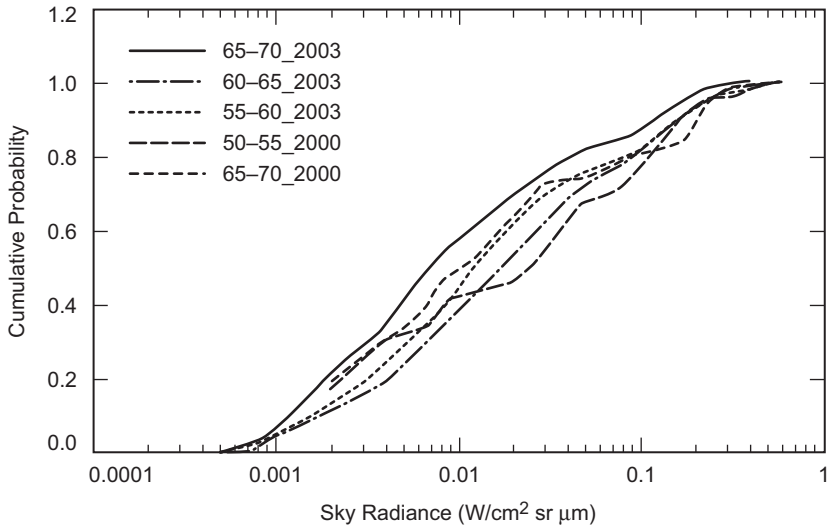

Fig. 3-31. Cumulative probability distribution of measured sky radiances at Table Mountain, California. The data sets marked 2003 were measured during June 2003–January 2004, while the data sets labeled 2000 were measured in January and February of 2000.

In the visible and near-infrared spectrum (our spectrum of interest so far), the planet irradiance is directly related to the reflection of sunlight (in the wavelength range between the mid infrared and far infrared range thermal emission of the planet must be taken into account [24]: this last case will not be discussed here).

Essentially, the planet irradiance can be described as the amount of the sunlight reflected by the planet surface (which is considered as a lambertian disk) and redirected towards the receiver. If a the receiver is located in space (outside the Earth atmosphere or in deep space where there is no interaction with gases and aerosols, implications for a receiver on Earth are introduced later in the section), one can write the planet irradiance E_λ at the receiver as [25]

$$E_\lambda = \frac{H_\lambda}{R_{AU}^2}\left(\frac{R_p}{Z_{PR}}\right)^2 a(\lambda) \tag{3.2-21}$$

where H_λ is the Sun spectral irradiance at 1 AU (Fig. 3-22) at the wavelength of interest, R_{AU} is the planet–Sun distance in AU, R_p is the radius of the planet, Z_{PR} is the planet–receiver distance, and $a(\lambda)$ is the planet spectral albedo. One can clearly notice, that the planet's irradiance is dimensionally related to the Sun spectral irradiance, which is usually indicated in the

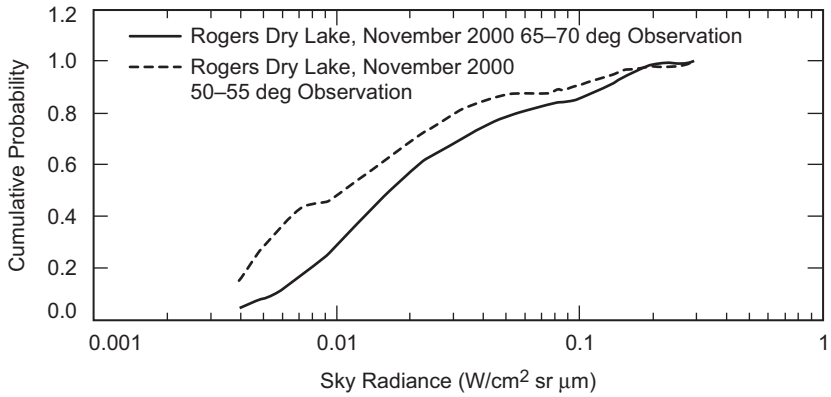

Fig. 3-32. Cumulative probability of sky radiance at a different location, Roger's Dry Lake, California.

Literature as W/(cm^2 μm). Therefore, if the receiver has an aperture of D centimeters in diameter, and the optical bandpass filter is $\Delta\lambda$ micrometers, the total planet background power, P_{pbg}, collected by the receiver is

$$P_{pbg} = E_\lambda \frac{\pi D^2 \Delta\lambda}{4} \tag{3.2-22}$$

Of course, Eq. (3.2-22) is valid if the angular extent of the planet is contained in the receiver FOV. If the angular extent of the planet exceeds the receiver FOV, only the fraction of the planet corresponding to the surface of the planet in the receiver FOV contributes to the background power. In this latter case, greater care must be taken when considering the planet geometric albedo. Some areas of the planet may not reflect uniformly because their albedo greatly depends on the composition (atmospheric and geological) of those specific areas. Therefore, the value of spectral albedo in Eq. (3.2-21) must correspond to these regions. For example, Fig. 3-33 depicts the variation of spectral albedo for different areas of Mars [25, 26].

As shown in Fig. 3-33, the Martian albedo can vary by a factor of four if the reflected light is coming from the dark mare areas or from bright desert area. Concerning the Sun–planet distance R_{AU}, since the orbit of the planets is not circular, there will be some variation due to the orbit eccentricity, and this variation must be taken into account. Table 3-6 summarizes data of orbital constants of planet, radius, and variation of solar irradiance at planetary distances. Notice that the ratio between the maximum and minimum irradiances for a fixed planet–receiver distance r_{Irr} is directly related to the eccentricity ε of the planet orbit as

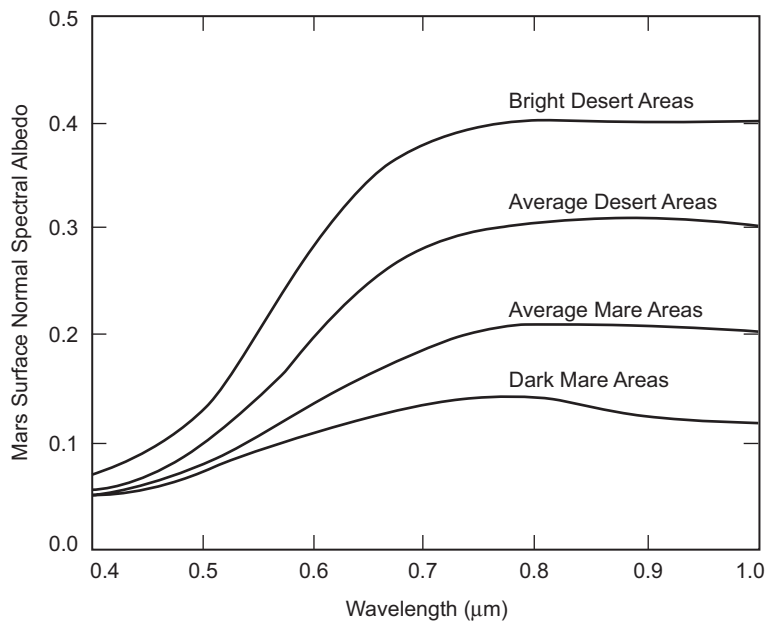

Fig. 3-33. Estimates of Mars spectral albedo for different surface areas.

$$r_{Irr} = \frac{(1+\varepsilon)^2}{(1-\varepsilon)^2} \tag{3.2-23}$$

To have a more precise evaluation of the planet irradiance as in Eq. (3.2-21), one must also consider the possible dependency of the planet irradiance on the sunlit sector of the planet seen from the receiver. The sunlit sector of the planet seen by the receiver depends on the phase angle. The phase angle, here indicated as ϕ_a in Fig. 3-34, is defined by Sun–planet–receiver angle. In fact, depending on the phase angle, one can notice that not all the disk corresponding to the surface illuminated by the Sun contributes to the planetary irradiance, but just a fraction of it. Considering the planet–Sun–receiver angle γ_s, elementary geometry shows that

$$\pi - \phi_a = \gamma_s + \theta_r \tag{3.2-24}$$

where θ_r is the Sun–receiver-planet angle, which is given by

$$\theta_r = \frac{1}{\sin(\gamma_s)}\left[\frac{R_{SR}}{R_{AU}} - \cos(\gamma_s)\right] \tag{3.2-25}$$

Table 3-6. Orbital constants and radii of the planets.

Planet	Semi-Major Axis of Orbit (AU)	Planet Radius (km)	Sidereal Period (days)	Eccentricity of the Orbit (ε)	Ratio Max/Min Irradiance
Mercury	0.387	2439	87.96	0.205	2.303
Venus	0.723	6051	224.7	0.006	1.028
Earth	1	6371	365.257	0.016	1.069
Mars	1.523	3390	686.98	0.093	1.454
Jupiter	5.203	69882	4332.58	0.048	1.212
Saturn	9.55	58234	10759.2	0.052	1.236
Uranus	19.18	25362	30685	0.049	1.218
Neptune	30.07	24622	60188	0.004	1.018
Pluto	39.44	1151	90700	0.252	2.806

Trigonometric calculations show then that the fraction of lit planetary disc is

$$\sin^2\left(\frac{\pi-\phi_a}{2}\right)=\sin^2\left(\frac{\gamma_s+\theta_r}{2}\right) \tag{3.2-26}$$

Of course, as long as the planet appears as an extended background source, its noise contribution is not affected by the above considerations. However, when the planet appears as a point source, its irradiance must be corrected by the lit fraction, as in Eq. (3.2-26). One should notice that this dependency is stronger for inner planets with respect to the receiver (e.g., receiver on Earth and with Mercury in the FOV). For outer planets (e.g., receiver on Earth and with Mars in the FOV), the fraction of the area lit from the Sun is closer to unity. For example, the Mars lit fraction is at the minimum of 87 percent, while for planets from Jupiter and beyond it is 99 percent.

Besides the lit fraction of a planet, there is also a dependence of the geometric albedo on the phase angle because the planet does not act as perfect lambertian reflector. This dependence is expressed by the phase function $f(\phi_a)$, which is shown for Mars [27] in Fig. 3-35. Typical features of the phase function are a linear part for phase angle exceeding approximately 10 deg, and higher order components for phase angles smaller approximately 5 deg. This enhanced reflectivity at small phase angles is called the “opposition effect.” Generally, albedos of planets with atmospheres have a smaller dependence on the phase angle than planets without atmospheres. Moreover, one must consider that the planet’s geometric albedo depends strongly on the wavelength of operation. A number of physical reasons contribute to this dependence, such as

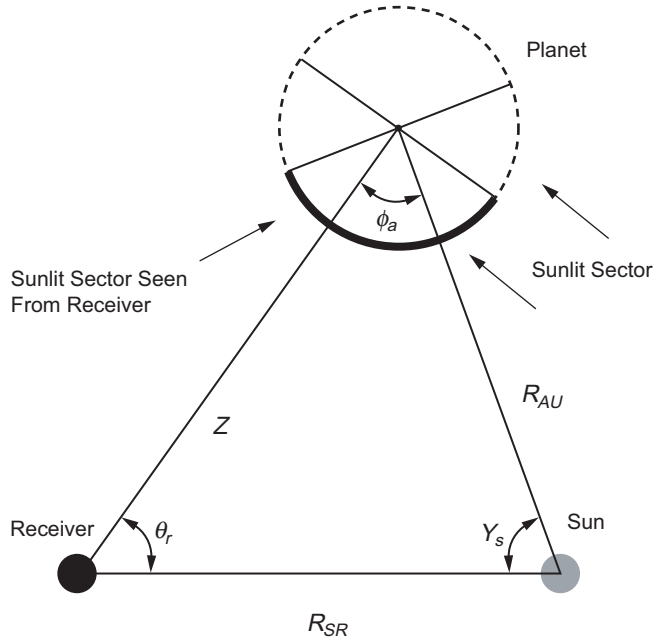

Fig. 3-34. Sun–planet–receiver system (for an inner planet).

planet atmosphere and Raman scattering. Examples of spectral variation of geometric albedo have already been shown in Fig. 3-33 for different area of Mars, while the average spectral variation of the geometric albedo for several other planets is indicated Fig. 3-36. The spectral albedos of Fig. 3-36 are at low resolution and therefore do not take into account of the absorption lines deriving by the reflecting planet atmospheric interactions.

Finally, one must remember that Eq. (3.2-20) and Eq. (3.2-21) refer to star and planet irradiance outside the atmosphere. For a receiver located on Earth, the irradiance is filtered by Earth's atmospheric transmittance $T(\lambda)$, and therefore, for example, a planet irradiance on Earth must be written as

$$E_{\lambda-Earth} = \frac{H_\lambda}{R_{AU}^2}\left(\frac{R_p}{Z_{PR}}\right)^2 a(\lambda)T(\lambda) \tag{3.2-27}$$

As an example of a planet irradiance seen on Earth, one can consider the case of a Mars–Earth downlink. Mars is in the FOV of a telescope located at 2 km above sea level with atmospheric visibility as in Fig. 3-17. The zenith angle of the telescope on Earth is 70 deg. Mars is at 2.4 AU, and the Sun–Mars distance is 1.4 AU. Considering the Sun irradiance as in Fig. 3-22, the Mars average albedo as in Fig. 3-31, for a phase angle close to zero, the Mars

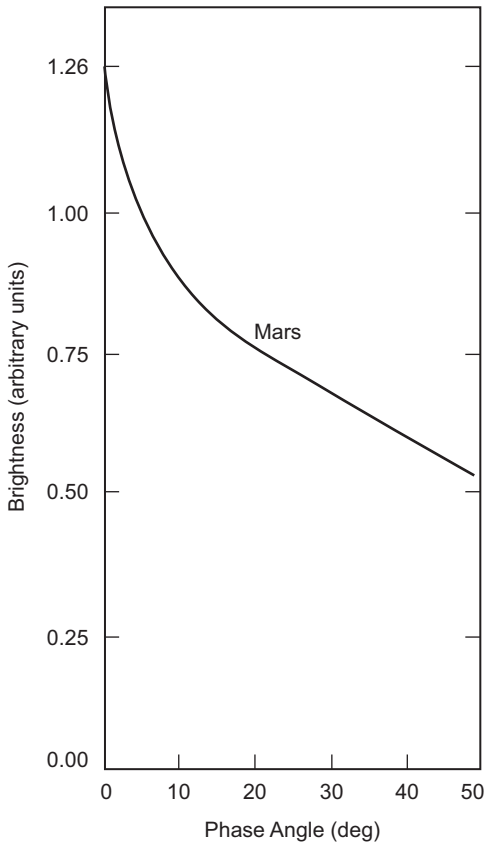

Fig. 3-35. Phase function for Mars after [25].

irradiance seen at the Earth receiver is indicated in Fig. 3-37. From Fig. 3-37, one may notice how the initial Sun irradiance is filtered by the Mars spectral albedo, which reduces spectral components in the visible, and also by the Earth's atmospheric transmittance, which blocks the forbidden bands in its spectrum.

Finally, to understand the impact of planet irradiance in a groundbased downlink scenario, one should compare the possible contribution of planet irradiance with sky background during daytime operations. In fact, comparing values of sky radiance from the previous section and Mars irradiance from Fig. 3-37, it is easy to convince oneself that background noise collected by Sun sky radiance is a number of orders of magnitude greater than that due to planet irradiance. Therefore, during daytime, the greatest source of background noise is represented by sky radiance, which otherwise is absent during nighttime.

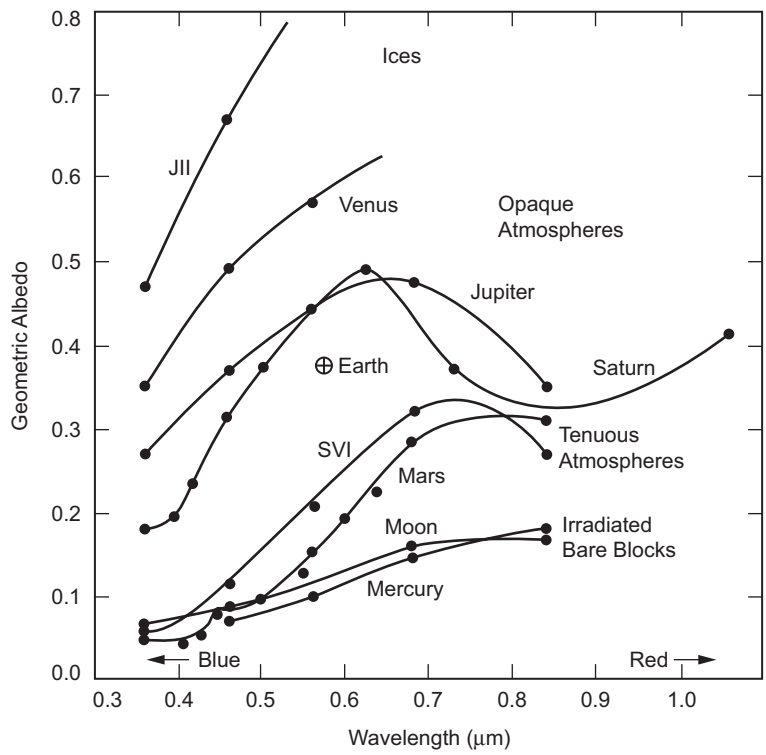

Fig. 3-36. Spectral variation of the geometric albedo for various planetary bodies (after Ref. 10 and Ref. 13).

3.3 Atmospheric Issues on Ground Telescope Site Selection for an Optical Deep Space Network

3.3.1 Optical Deep Space Network

To support deep space missions aimed to the exploration of the universe for the last four decades, NASA has designed and operated a global network of radio-frequency ground stations termed the Deep Space Network (DSN). Clearly, as the use of optical wavelengths has become a feasible technological option for deep space missions, future deployment of an optical deep space network (ODSN) might replicate the function of the DSN. However, the design of an ODSN poses new challenges in terms of mission requirements, mitigation of weather effects, life-cycle cost, and optimization of antenna (telescope) performances. Figure 3-38 summarizes some of the dynamic interactions among ODSN parameters and logistics, environmental, and technological variables.

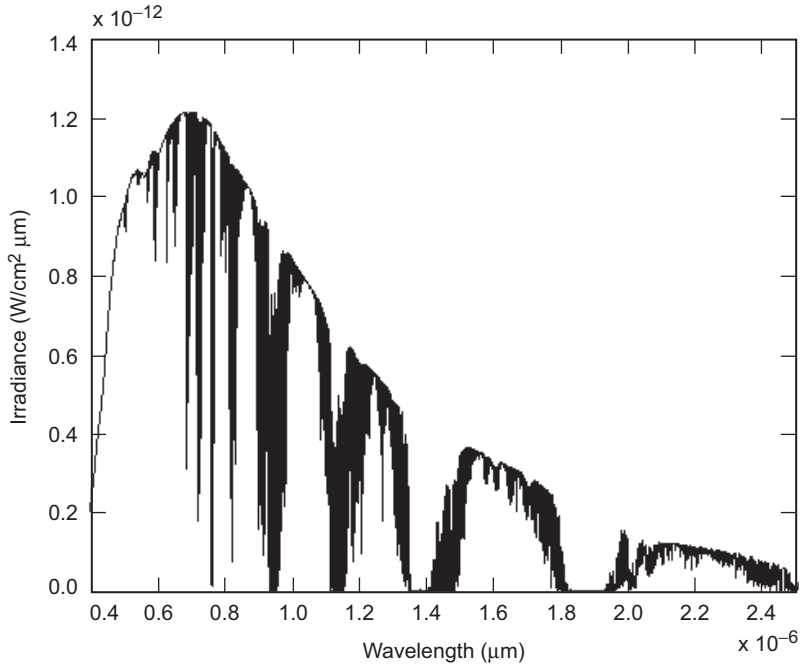

Fig. 3-37. Mars irradiance as seen when the planet is in the FOV of a telescope on Earth, located at 2 km above sea level, with an observation zenith angle of 70 deg, and with clear sky. The Earth–Mars distance is 2.4 AU, and the Mars–Sun distance is 1.4 AU. The phase angle is close to zero.

Note that in Fig. 3-38, three main parameters of the ODSN are listed as being the data delivery capacity and accuracy (data rate/BER), the continuous Earth coverage (network continuity), and the proper location of the nodes (i.e., optical communication telescopes) of the network itself (ground telescope sites). The data rate/BER is clearly influenced by the amount of signal photon flux collected by the aperture of the ground telescope site. This signal flux depends upon, among other factors, the angular spread of the laser beam and the atmospheric transmittance experienced at the receiver. Both atmospheric transmittance and laser beam width are related to the selected transmitter (spacecraft) wavelength, which also determines the sky background radiance, which during daytime operation contributes to increasing the noise level at the detector level.

The number of sky background photons collected by the detector is also determined by the receiver FOV, which is related to effects of atmospheric turbulence. Analysis of atmospheric turbulence effects is presented in a later section of this chapter. To ensure the continuous coverage of the Earth from deep space, despite its rotation, it is necessary to distribute a number of ground

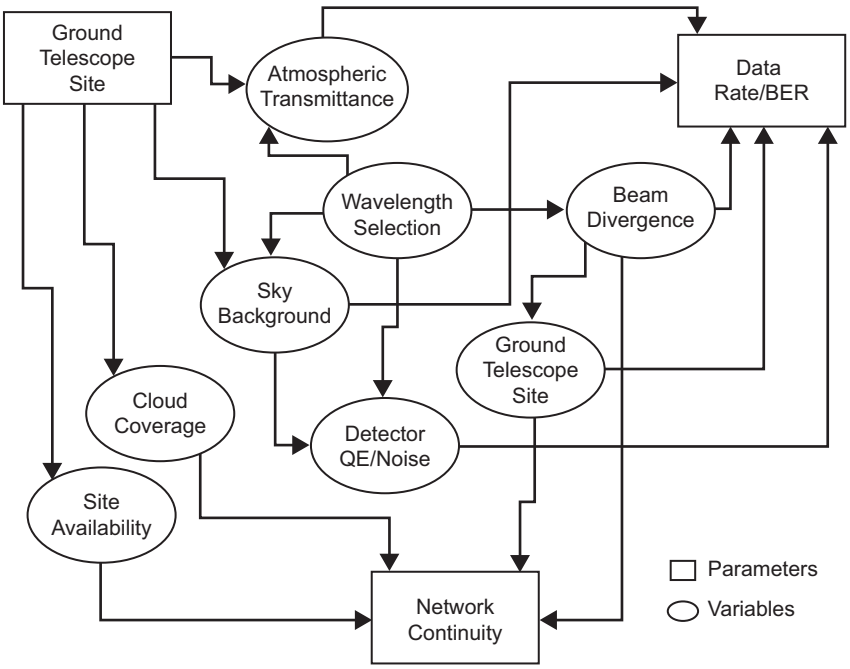

Fig. 3-38. Flowchart illustrating the dynamics among the main ODSN parameters and variables.

telescopes around the globe. Today NASA's DSN only requires three radio-telescope hubs (ground station complexes) to successfully operate the network. The DSN stations (located at approximately 120 deg of separation around the Earth: Goldstone, California; Madrid, Spain; and Canberra, Australia) allow continuous coverage of deep space from Earth. However, operation of the future ODSN will require a different geographical and logistical approach. Since the laser transmitter beam width from space can (usually) cover a limited area (footprint) on Earth it is necessary that the ODSN consists of a number of ground stations located around the Earth as a linear distributed optical subnet (LDOS) [28], Fig. 3-39. The idea behind LDOS is to have the spacecraft always pointing at a visible station belonging to the LDOS. When either the line of sight is too low on the horizon (20 deg of elevation) or is blocked by atmospheric conditions (e.g., clouds or low transmittance), the spacecraft beam is switched to a different station (or network node) by pointing to the adjacent optical ground station. Of course the adjacent station must be located in a geographical area where the atmospheric conditions are uncorrelated (or better, anti-correlated) with the previous station in order to optimize network continuity.

To simplify both the spacecraft re-pointing process and the network hand-off between stations, another network architecture has been proposed. The clustered optical subnet, or COS [28], consists of a number of optical hubs (three or more) distributed around the Earth, with the difference that each hub is composed of more than one ground station (e.g., two or three). Each ground station of a hub (circle in Fig. 3-39) is located in a geographical area having (dry) weather pattern that is uncorrelated (or better anticorrelated) to the other stations to optimize the overall hub availability having at least one station with clear line-of-sight with the spacecraft (Fig. 3-39).

Of course, the location of the ground telescope is critical to the assurance of network operation continuity and is directly linked to the data rate/BER performances. As stated earlier, cloud coverage at the ground station has to be as low as possible to minimize link blockage, and it must be somehow predictable for program station operation. Moreover, at the ground station, the link must experience the highest atmospheric transmittance and lowest sky background possible during daytime. All of the previous atmospheric conditions are optimized when the optical ground station is located at high altitude because the signal atmospheric path is reduced and so, consequently, is its interaction with the atmosphere. Moreover, local microclimatic conditions that usually generate low clouds are not influential at high altitudes (usually more than 2000 m), which reduce the overall cloud coverage at the station. At the same time, the ODSN network continuity requirements demand a regular distribution around the Earth of peaks that may accommodate potential ground stations. Unfortunately, the global scarcity of potential telescope sites around the Earth and their uneven distribution (along with ever-present geopolitical implications) makes their identification even more complex for the design of a global ODSN.

Therefore, we describe an analysis and methodology that can be used to identify possible peak candidates for a future ODSN. The approach is as follows. First, we define a baseline optical deep space mission. By determining characteristics of an optical communication payload on the spacecraft and using a link budget, we calculate the photon flux reaching the Earth. Then, modeling the atmospheric effects along the atmospheric profile, we determine the atmospheric losses, the background photon noise, and the receiver performance at different peak altitudes, which helps identify the optimal peak elevation for an individual ground station in an ODSN. Finally, we study the global distribution of the Earth’s peaks and landmass elevations at the required altitude, and we introduce determined conditions about the required low-cloud coverage. Results from this last step will help in selecting the telescope sites for the ODSN and in analyzing the advantages of LDOS versus COS (or vice versa).

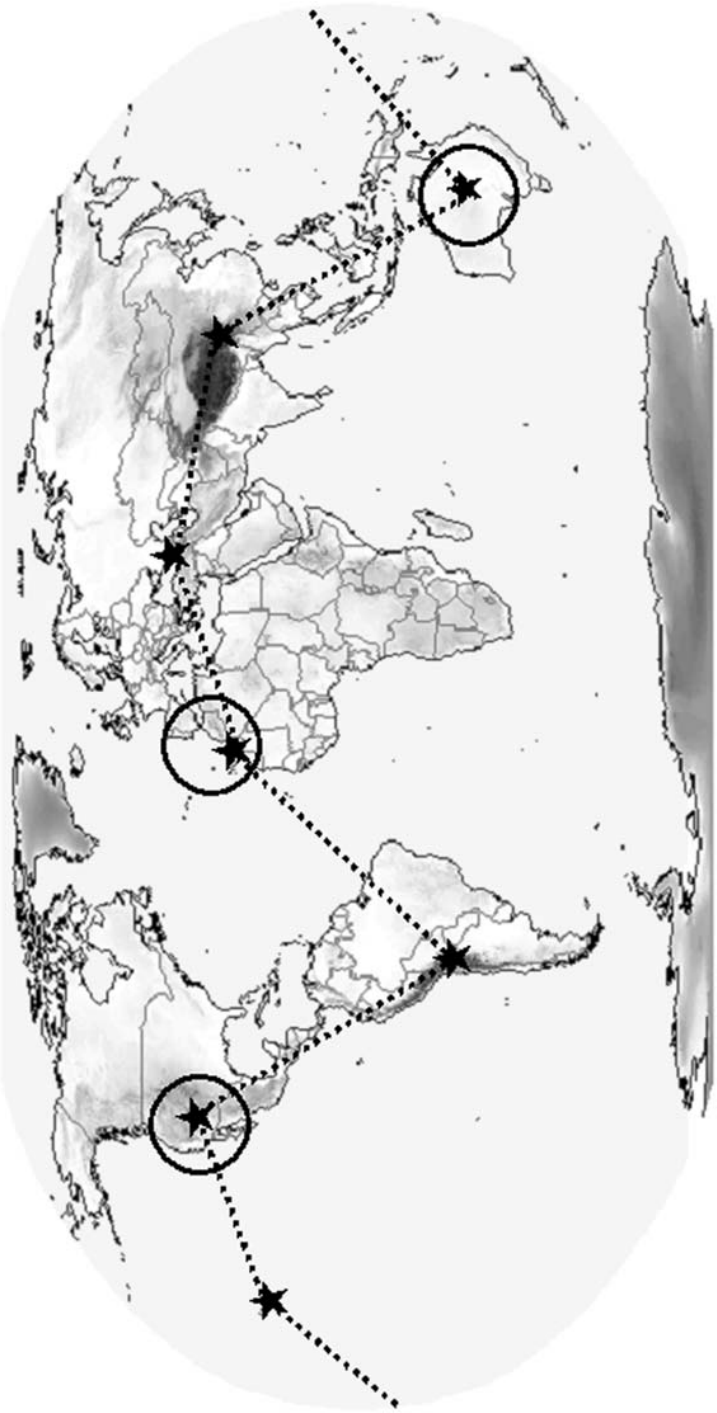

Fig. 3-39. Example of LDOS (star = telescope) and COS (circle = hub) architectures for an optical deep space network (ODSN).

3.3.2 Data Rate/BER of a Mission

The long-term objective of the ODSN is to provide ground support for Solar System exploration. In doing so, a practical and logical step is to base the ODSN analysis and site selection strategy around a specific mission and use it as a reference model to begin the point design.

A first logical choice for a reference mission for the ODSN is to understand how it may support a Mars mission. To design the ODSN as a support for a Mars mission, the next logical step is to derive an initial link budget based on the requirements, and then to analyze how the telescope aperture and the telescope location (via the atmospheric transmittance and daytime sky radiance noise) may affect the link budget itself. Specifically, the mission is required to provide a link at 1 million bits per second (Mbps), with an uncoded bit error rate (BER) of 0.001 at the largest distance of separation between Mars and Earth of 2.4 AU. The spacecraft laser has 5 W of average power, and the wavelength selected is $\lambda = 1064$ nm. (Another possible option is to consider 1550 nm for the laser wavelength.) The modulation used is M-ary Pulse Position Modulation (M-PPM) with M = 256, which corresponds to a 31-ns pulse. The spacecraft telescope has an aperture of 30 cm diameter with a linear obscuration of 10 percent. Transmitter loss was set to be 1.42 dB (72% of the laser power). Given these data, we ran a link with results as summarized in Table 3-7.

Because we did not restrict the ground telescope to a specific site (and therefore to a specific atmospheric condition), the link budget of Table 3-7 does not indicate any atmospheric loss. Concerning the receiver, we supposed an optical loss of 2.21 dB (60 percent transmission), and we normalized the receiver aperture to 1 m in diameter with linear obscuration of 20 percent to better describe the photon/flux per telescope aperture at the detector of a telescope on Earth. Losses of non-ideal synchronization and pulse amplitude were also added. Table 3-7 shows that in these conditions photon flux is 10.45 photons per pulse at the detector. To complete the information on link performance, a brief characterization of the receiver is necessary. Because our intent in this monograph is to consider a general detection case, we hypothesized a photodetector of quantum efficiency of 50 percent. Thermal noise is then not considered, which can be an appropriate hypothesis in the case of a cryogenic receiver with low noise amplification [29]. Noise from photodetector dark counts is also not considered (photodetector dark counts are greatly reduced when the photodetector is cooled to cryogenic temperature [30]).

3.3.3 Telescope Site Location

As already presented in a previous subsection, Earth's atmosphere affects the optical signal from deep space in two ways. First, when the optical signal

Table 3-7. Link Summary.
Bit Rate: 1.0 Mbps Modulation: PPM (M = 256)
Range: 3.59×10^8 km BER: 0.0010

Parameter	Description		Budget
Transmitter power	5.0-W average	31-ns slot time	61.08 dBm
Optical transmitter losses	72% transmitted		–1.42 dB
Transmitter gain	30.0-cm aperture	5.98 μr beam-width	117.67 dB
Pointing losses			–2 dB
Space loss	3.59×10^8 km	2.4 AU	–372.54 dB
Atmospheric transmission	100.0% transmitted	No atmosphere	0.0 dB
Receiver telescope gain	1.0-m aperture	20% obscured	129.40 dB
Optical receiver losses	60% transmitted		–2.21 dB
Non-ideal bit synch. adjustments			–1.0 dB
Pulse amplitude variation adjustments			–1.0 dB
Peak signal power at detector	10.45 photons/pulse	0.06262-nW peak	**–72.03 dBm**

goes through the atmosphere, it is partially (if the wavelength is not in the forbidden bands) attenuated. The longer the path through the atmosphere, the lower the atmospheric transmittance. Therefore, the higher the telescope's altitude, the higher the atmospheric transmittance. Moreover, the larger the observation zenith angle, the lower the atmospheric transmittance. Second, during daytime, the sunlight scattered by the atmosphere causes a number of unwanted photons to be collected by the telescope aperture, increasing the noise level at the receiver and badly affecting the receiver performance (BER) itself. Again, sky radiance is dependent on the sunlight's path through the atmosphere. Moreover, sky radiance depends on the concentration of aerosol suspended in the atmosphere, and finally it depends on the Sun–Earth–Probe (SEP) separation angle. To guarantee the largest continuity of the data delivery, it is recommended that the SEP angle be as low as possible. In this study, we assume a SEP of 5 deg. Also, in order to limit the number of stations deployed by the ODSN, an optical communication telescope must be able to observe the sky at a large zenith angle (low elevation angle). In our study, therefore, we set this limit at 70 deg of zenith angle.

A good baseline for the ODSN is to require that the ground stations work in the worst conditions for transmission and sky radiance (except the case of overcast sky where the link cannot be closed at all) that correspond, from our

assumptions above, to the case of 70 deg from zenith for observation angle and 5 deg of separation from the Sun during daytime. (One should notice that star and planet irradiances in the FOV of the telescope during daytime are much less than the sky radiance; and therefore, it is possible to ignore them without loss of accuracy.)

The MODTRAN simulation program [14] was used to describe values of sky radiance and atmospheric transmittance at different altitudes over the Earth. The Fig. 3-40 simulation considers altitudes between 0.5 and 3.5 km. The simulation refers to an atmospheric profile typical of a mid-latitude region, with the rural aerosol model, having its boundary layer starting at 0.5 km. Two cases of aerosol concentration are indicated, clear sky (visual range of 23 km at the bottom of the boundary layer) and hazy (visual range of 5 km at the bottom of the boundary layer). Keeping in mind that the aerosol concentration decreases exponentially starting at the beginning of the boundary layer, Fig. 3-40 shows that at 2 km of altitude, transmittance and radiance are independent of the aerosol concentration at the boundary layer. In Fig. 3-40, the dashed line describes the case of a rural aerosol model with a visual range of 5 km (hazy

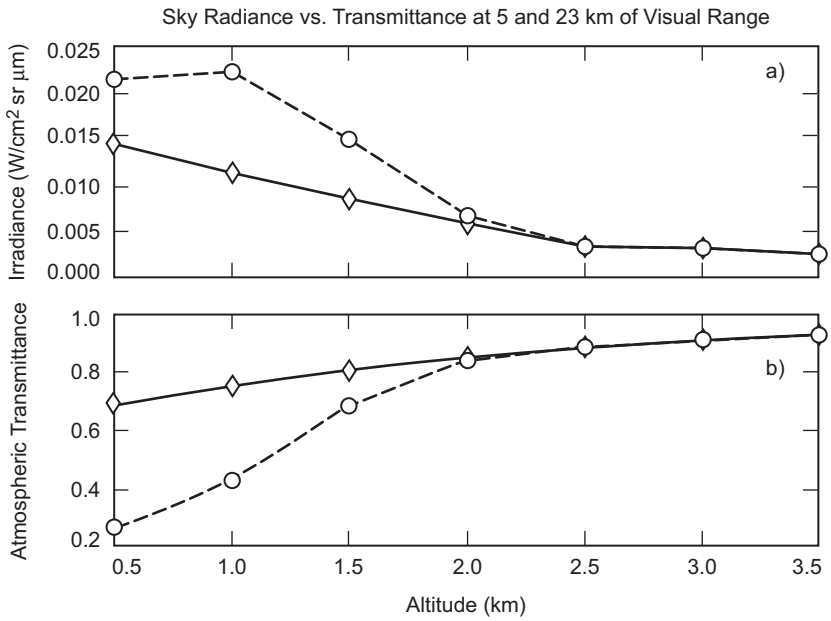

Fig. 3-40. (a) Sky radiance versus transmittance at 1064 nm for varying altitude of a telescope at 70-deg zenith angle with a 5-deg SEP angle. The dashed line describes the case of a rural aerosol model with visual range of 5 km (hazy sky) at the bottom of the boundary layer. The continuous line is for visual range of 23 km (clear sky) at the bottom of the boundary layer. (b) Atmospheric transmittance at 1064 nm for varying altitude for a telescope at 70-deg zenith angle. The dashed and continuous lines relate to atmospheric conditions as in (a).

From examination of Fig. 3-41, one can see that there are obvious compromises between aperture size and site altitude. Of course, the deployment of a smaller-aperture telescope has its own advantages, mainly related to the cost [31,32]. However, the scarcity of peaks available at higher altitude may also make it easier to find a lower altitude point that can house a large-aperture telescope (e.g., 10 m) for deep space optical communications. Moreover in the design of a global ODSN, the dichotomy of the problem "telescope aperture vs. site altitude" is even more critical. In fact, in a global ODSN, each single telescope must be located with precise coverage requirements that depend on the location of all the ground stations in the ODSN itself.

3.3.4 Network Continuity and Peaks

In a global ODSN, in principle the sites selected need to meet most, if not all, of the following conditions.

1) Latitude in proximity of the equator to better track spacecraft in the Solar System ecliptic. In this work we consider the latitude within range of ±40 deg.
2) Longitude according to the architecture requirements, in our case according to LDOS or COS requirements.
3) A minimum mutual view period of 4 hours with at least one other site, to allow smooth hand-off of the operations.
4) Absence of geopolitical issues for site locations outside the United States.
5) Close to pre-existing facilities for easy installation and operation.
6) Low time-duration (year-long) cloud coverage with fairly constant and predictable weather.
7) High altitude for high atmospheric transmittance and low sky radiance, as derived in Subsection 3.2.4.
8) Favorable atmospheric seeing (as explained in the next subsection).

Considering the results obtained in the previous subsection, we derived the baseline that when selecting a site for a 5-m aperture telescope, an optimal site altitude would be 1.9 km, while for a 10-m aperture the requirement can be relaxed to 1.2 km. Unfortunately, there is an overall scarcity of high-elevation land on Earth, as indicated in Fig. 3-42. Overall, only 7.5 percent of the Earth is above 1 km, 3.2 percent is above 2 km, and 1.38 percent is above 3 km. The latitude restriction of ±40 deg of the Earth surface dictated by the above selection criterion 2) further restricts the landmass availability to 3.5 percent, 1.2 percent, and 0.76 percent respectively for altitude above 1, 2, and 3 km. Furthermore, geopolitical restrictions imposed by selection criterion 4), and the fact that the peaks are not regularly distributed in the Earth's landmass, greatly limit the availability of candidate sites for a global ODSN.

As a first approach to analyze the global availability of global peaks, we elaborated a digital topographic map of Earth with resolution of 2 km × 2 km. The Earth surface to be analyzed was restricted in the latitude interval [–40, +40] and longitude interval –180, 180]. Moreover, to better view the potential ODSN site distribution, we divided the Earth altitude in three interval ranges as 0–1 km, 1–2 km, 2–3 km, 3–4 km, and higher than 4 km. Results of this altitude level division of the Earth surface are presented in Fig. 3-43. Again, one should notice that only 7.5 percent of the Earth is above 1 km, 3.2 percent is above 2 km, and 1.38 percent above 3 km when considering the entire globe (solid curve). Restricting the available landmass within latitude +40° (dashed curve), we have only 3.5 percent, 1.2 percent, and 0.76 percent of Earth above altitudes of 1, 2, and 3 km, respectively.

Analyzing the Earth elevation map in Fig. 3-43, provides a number of useful indications for the construction of an ODSN. For instance, if the LDOS design approach is going to be taken for the global ODSN architecture, there is large area of Earth, mainly defined by the Pacific Ocean that lacks available peaks. In that case, a sure stop for a station in the LDOS must to be Hawaii, where incidentally there are already a number of astronomical telescopes housed on high-altitude peaks (e.g., Mauna Kea and Mount Haleakala). At the same time, Australia (where incidentally there is already a DSN radio-antenna complex), is relatively poor in high-altitude areas. Mainly, these locations, all within in the first range of 1–2 km of elevation, are concentrated in the center of the continent (Alice Springs) or close to the east coast of the continent. This

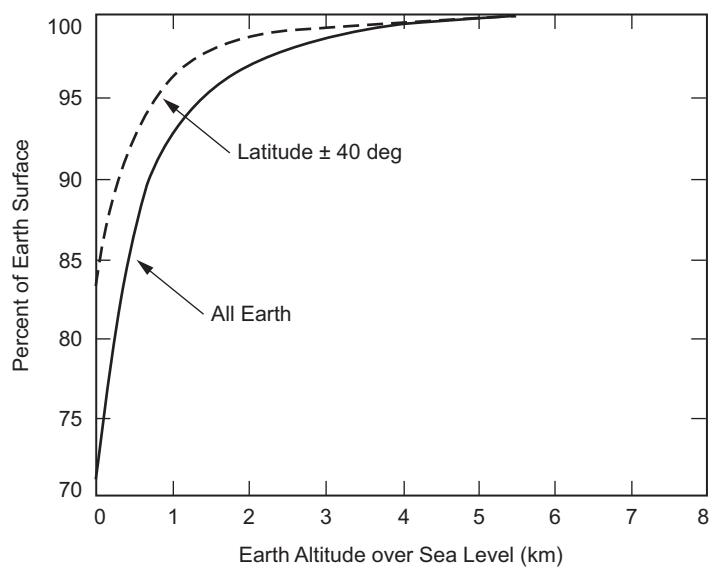

Fig. 3-42. Cumulative altitude distribution function of Earth's landmass.

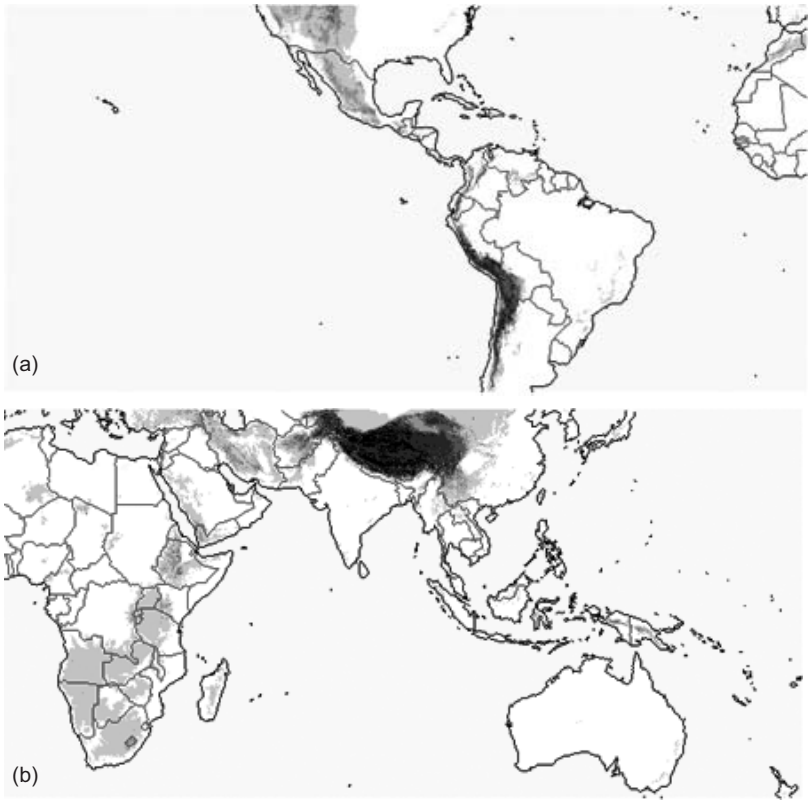

Fig. 3-43. Depiction of Earth landmass altitude in the latitude range of [–40 deg, 40 deg] at different ranges, as 0–1 km (white), 1–2 km (light gray), 2–3 km (gray), 3–4 km (dark gray), more than 4 km (black): (a) Earth map in the longitude range [–180 deg, 0 deg] and (b) Earth map in the longitude range of [0 deg, 180 deg].

scarcity of peaks in Australia can hamper the possible design of COS with a possible hub in this continent as previously suggested in the literature [28]. However, a more definitive answer to this last problem can come only after a careful evaluation and measurements of the sky background radiance and atmospheric transmission at candidate sites in Australia. However, as also stated by selection criteria 6), the altitude of the station of the ODSN, is not the only atmospheric/environmental requirement.

The location of a network station must be in an area where the cloud coverage has minimal impact on the operation of the network itself. Therefore, a more powerful indication of the site suitability for belonging to the ODSN can be made after simultaneously considering cloud coverage statistics of the area and peak availability. To better explain the study approach for joint correlation of low cloud coverage and higher altitude peaks, we first present in

Fig. 3-44 the cloud coverage in the section of Earth of interest for the ODSN using data from the International Satellite Cloud Climatology Project (ISCCP) [33].

The Earth map in Fig. 3-44 is within latitude range [–40 deg, 40 deg] and longitude range [–180 deg, 180 deg], and the map resolution is 2.5 deg × 2.5 deg. The figure indicates in grayscale-coded fashion the annual average of cloud coverage in percent in the region of Earth of interest for the ODSN. Clearly, for ODSN site selection, average cloud coverage duration must be as low as possible.

While the map in Fig. 3-44 may indicate regions of favorable cloud coverage for the installment of optical telescopes for deep space communication, it does not convey any information about the site/area altitude. However, one can further reduce the search for ODSN sites around the Earth, by introducing the simultaneous selection criteria of low cloud coverage (less than 50 percent) and altitude higher than 1 km (other more restrictive conditions about cloud coverage and altitude can also be used). Results from this last operation are shown in the maps of Fig. 3-45.

Figure 3-45 gives us more precise indications about the possible locations for ODSN and its possible architectural solutions. Starting from the Eastern Hemisphere as depicted in Fig. 3-45 a), beside Hawaii, other candidate areas are the United States Southwest and the Andes region (including northern Chile, southern Peru, and portions of Ecuador. Unfortunately, there is a lack of available sites east of these regions in both North and South America. Proceeding eastward, we can observe a number of candidate sites in the northern African continent and southern Spain. Southern Africa and eastern Africa (especially close to the horn of Africa) may also be regions of interest. A number of interesting regions are located in the Middle East, particularly in the Arabian Peninsula. Unfortunately, after the a region west of Pakistan and the Karakorum, moving eastward, (according to this first analysis) there is a great scarcity of peaks available in the map, except for the region around Alice Springs in the Australian Outback, and on the Australian east coast itself.

In conclusion, the approach just described is a practical methodology for the selection of potential sites for a global ODSN. In our approach, we first baselined a possible deep space mission and its requirements in terms of BER, link margin, data rate, and a few design figures (e.g., modulation, spacecraft, and ground telescope optical transmission). Then, to study link performance, it was supposed in our link scenario that we considered the worst case of optical signal interaction with Earth (i.e., 5 deg of SEP angle, 70 deg of observation zenith angle, and 2.4 AU range). It was demonstrated that at different altitudes on Earth, link performances differ greatly, and also that for different telescope apertures, there are different requirements for Earth altitude in order to successfully close the link. Next, we projected our study from single telescope

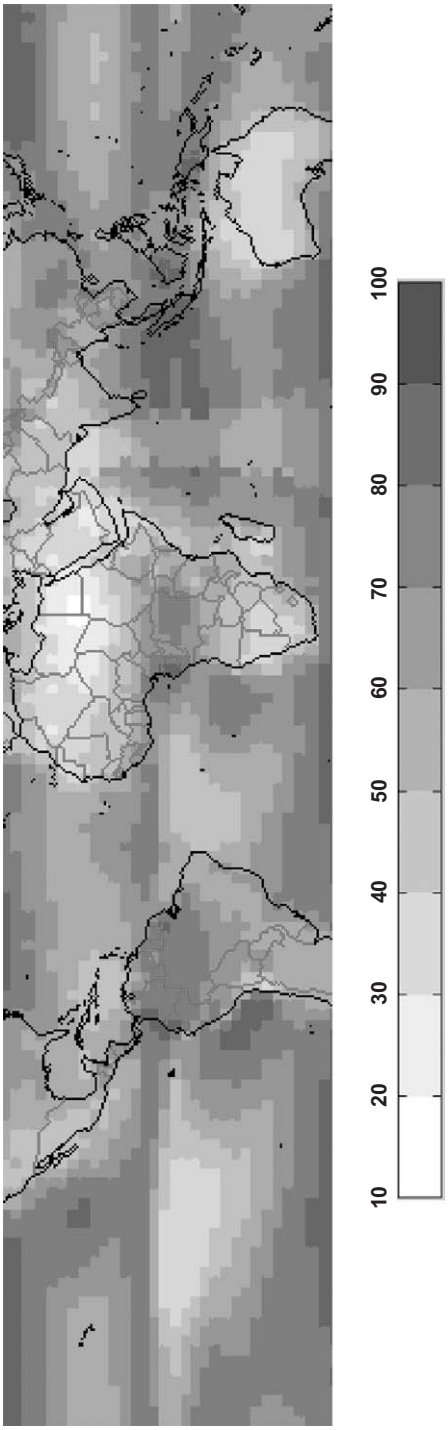

Fig. 3-44. Average annual percentage of cloud coverage for the Earth surface in the latitude range of [–40 deg, 40 deg]. The cloud coverage percent duration is indicated by the gray-scale per horizontal bar.

location to a global ODSN, and we demonstrated that high-altitude siting requirements, jointly with those of global cloud coverage, greatly restrict the landmass availability to house ODSN ground stations.

However, a number of issues must be further explored and amplified to provide a more precise answer to the problem of ODSN site selection. For instance, we limited the deep space mission requirements to a minimum 5 deg SEP angle separation. Conversely, to extend the duration of link coverage during a mission, the SEP angle requirement can be further reduced. Consequences of a smaller SEP angle separation will be a greater background sky radiance captured by the ground station and a greater noise in the receiver. A direct consequence of a noisier receiver is that our minimum altitude per station requirement will be raised, and fewer sites will be suitable for the ODSN use.

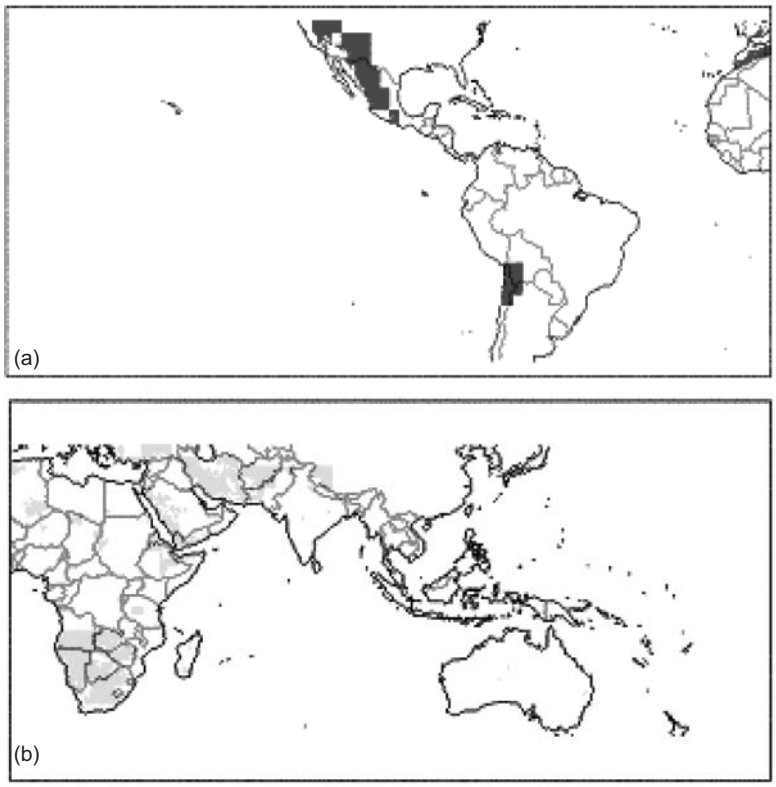

Fig. 3-45. Locations on Earth in the latitude range [–40 deg, 40 deg] that satisfy the simultaneous conditions of altitude higher than 1 km and average annual cloud coverage less than 50 percent: (a) Earth map in the longitude range [–180 deg, 0 deg] and (b) Earth map in the longitude range of [0 deg, 180 deg].

This work analysis can be further improved by providing a more precise model of the receiver channel. For instance, we did not consider effects of thermal noise in the receiver, or other noise factors derived by the detector dark counts. In other cases, a Poisson channel may be more representative of the receiver statistics. In any case, a precise modeling of the receiver channel can provide better information on the BER statistics and, therefore, the necessary signal photon flux that can satisfy the link requirements. Conversely (as previously demonstrated in this chapter), from these requirements we can derive the ground station diameter and/or the altitude of the ODSN stations.

Considering the meteorological activity of Earth, we introduced in our analysis a methodological approach to use global information on the cloud coverage. However, to further improve this analysis it is also necessary to consider diversity statistics [6]. In fact, to optimize Earth coverage, one of the operational principles of the ODSN is that at least two stations must be contemporarily seen by the spacecraft pointing towards Earth. In this case, the positioning of the stations with respect to each other cannot be done without considering weather diversity.

Finally, in this study we did not consider the action of atmospheric turbulences. It is known that Earth turbulence badly affects the signal both on the downlink and on the uplink in a number of ways. One of the most evident effects of turbulence is the spreading of the received signal focused on the photodetector with a consequence of net loss of power [34]. Again, to limit effects of atmospheric turbulences, the ground station should be located higher in altitude (i.e., less turbulent atmospheric path for the uplink and downlink signal), which again may further raise the threshold of minimum altitude for ODSN ground stations and the related available sites. Implications of atmospheric turbulence effects on the deep space downlink analysis and on the global ODSN need therefore to be included. A description of such effects is presented in the next subsection of this chapter.

3.4 Laser Propagation Through the Turbulent Atmosphere

3.4.1 Atmospheric Turbulence

As noted in the opening paragraphs of this chapter, laser beam propagation is perturbed by random refractive index fluctuations of the Earth's atmosphere. Therefore, a plane wave arriving at the top of the atmosphere, from a deep-space-transmitted laser beam, undergoes phase distortions prior to incidence on a groundbased receiver. This subsection discusses the impact of these phase distortions upon laser communications. The discussion is initiated with a brief summary of relevant atmospheric properties. Following this description, the dominant effects on link performance (namely, turbulence-induced spatial and

temporal effects on the received irradiance) are discussed. Experimental results of laser beam propagation through horizontal atmospheric paths are also included, and even though these are not truly representative of deep space optical link configurations, they are indicative of the relevance of the theory. For gaining a deeper understanding of the problem, relating atmospheric turbulence to laser beam propagation the reader is urged to explore the vast amount of existing literature [35–40] on the subject. The following discussion is a very high-level summary extracted from the detailed discussions presented in these references.

The atmosphere can be thought of as a medium into which energy is injected in the form of thermally induced convection or wind shear. The upper scale at which this energy is dissipated is known as the outer atmospheric scale, commonly designated as, L_0. This outer scale is representative of the largest sized eddies involved in flows, that upon reaching a critical point break down to smaller scales by a cascading process. The critical point occurs due to the Reynolds number (Re) exceeding a value that demarcates laminar and turbulent flows. Re is defined as:

$$\mathrm{Re} = \frac{Vl}{n} \tag{3.4-1}$$

where V is the flow velocity, l is the scale size, and ν is the kinematic viscosity. For air, the kinematic viscosity is 1.5×10^{-5} m^2/s; therefore, if the product $V \times l$ exceeds 0.033, the critical Re (2200) that distinguishes between laminar and turbulent flows will be exceeded, hence the term atmospheric turbulence. This stepwise reduction in dissipation-scale or "eddy" size continues until an inner scale size, l_0 is reached. Below the inner scale size, energy dissipation occurs by viscous effects. The scale size bounded by L_0 and l_0 is referred to as the inertial scale, and it typically ranges from 10–100 m down to 0.1–1 cm.

The mathematical description of atmospheric turbulence, and in particular its effect on optical beam propagation, relies on idealized assumptions that treat the fluctuations of atmospheric parameters as stationary random processes that are homogeneous and isotropic. Within this mathematical framework, Kolomogorov [35,40] showed that the structure function follows a $r^{2/3}$ dependence, where r refers to the spatial scale defined as:

$$r = \left|\bar{r}_1 - \bar{r}_2\right| \tag{3.4-2}$$

with $\bar{r}_1$ and $\bar{r}_2$ referring to position vectors with $l_0 \le r \le L_0$ $l_0 \le r \le L_0$. The structure function for a random variable $x(r)$ is defined as:

$$Dx(\bar{r}_1, \bar{r}_2) = \left\langle \left| x(\bar{r}_1) - x(\bar{r}_2) \right|^2 \right\rangle \tag{3.4-3a}$$

If the random variable $x(r)$ has a slowly varying mean with a superimposed fluctuation as represented by Eq. (3.4.3b)

$$x(\bar{r}_1) = \langle x(\bar{r}_1) \rangle + x'(\bar{r}_1) \tag{3.4-3b}$$

with the term in angle brackets denoting a slowly varying mean. With this definition of the random variable $x(r)$, the structure function can be rewritten as

$$Dx(\bar{r}_1, \bar{r}_2) = \left[\langle x(\bar{r}_1) \rangle - \langle x(\bar{r}_2) \rangle \right]^2 + \left\langle \left[\langle x'(\bar{r}_1) \rangle - \langle x'(\bar{r}_2) \rangle \right]^2 \right\rangle \tag{3.4-3c}$$

The first term in Eq. (3.4-3b) goes to zero for a stationary random process thereby emphasizing the merits of using the structure function in describing the fluctuations. The discussion above can be extended to any of the random variables associated with the atmosphere, such as velocity, temperature, and (of particular interest to optical propagation) refractive index $n(r, t)$

$$n(\bar{r}) = n_0 + n'(\bar{r}) \tag{3.4-4}$$

where $n_0 \cong 1$ represents the mean and $n'(\bar{r})$ represents random fluctuations. Furthermore, the long-term mean of the fluctuations is also equal to zero. The left-hand side of Eq. (3.4-4) can be related to visible and near-infrared optical wavelengths (λ), pressure $p(r)$, and temperature $T(r)$ by the relation:

$$n(\bar{r}) = 1 + 77.6 \times 10^{-6} \left(1 + 7.52 \times 10^{-3} \lambda^{-2} \right) \frac{p(\bar{r})}{T(\bar{r})} \tag{3.4-5}$$

Furthermore, the structure function for refractive index $D_n(r)$ can be expressed as:

$$D_n(r) = C_n^2 r^{2/3} \text{ for } l_0 \le r \le L_0 \tag{3.4-6a}$$

$$D_n(r) = C_n^2 r^{-4/3} r^2 \text{ for } r << l_0 \tag{3.4-6b}$$

The quantity C_n^2 is called the structure function constant of the refractive index, and mathematically it represents the slope of the structure function versus $r^{2/3}$ plot in the inertial range. The structure constant can be related to other structure function constants of temperature C_T^2 and velocity C_v^2, where

$$D_T(r) = C_T^2 r^{2/3} \text{ and } D_v(r) = C_v^2 r^{2/3} \text{ for } l_0 \le r \le L_0 \tag{3.4-6c}$$

The discussion so far has emphasized spatial fluctuations of atmospheric parameters; however, knowledge of temporal characteristics is also needed for

optical communications designers to devise strategies for mitigating temporal fluctuations. Atmospheric perturbations that contribute to temporal fluctuations owe their time scale to two types of effects, those associated with atmospheric eddies flowing past a fixed observer and those having to do with the dynamics within the eddy or atmospheric "cell." The former time scale is of the order of L_0 / V_T or D / V_T where V_T is the traverse wind speed and D is the diameter of the collecting aperture. For example, with the $V_T = 12$ m/s and D ranging from 5–10 m, the time scales of the order of 0.5–1 s are obtained. The dynamics within an atmospheric eddy or "cell" are thought to be of a longer duration, and the Taylor frozen-atmosphere hypothesis [40] is invoked to ignore this effect.

The preceding brief discussion of atmospheric turbulence introduced the refractive index structure function constant. Various moments of this function can be defined, and these in turn can be used to make first-order predictions of the effects expected on optical-link performance. The validity of these predictions will to a large extent depend upon the link configuration, as well as the location of the optical transmitter and receiver. Before initiating a discussion of these effects, however, a brief description of the methods followed to describe C_n^2 are in order.

Measurements of the refractive index structure function constant or C_n^2 can be classified into boundary-layer and free-atmosphere measurements. The boundary layer is the region close to the surface over which convective instabilities extend due to temperature differences. This region can extend from hundreds of meters to 2 km above the surface. Furthermore, it is dynamic, depending upon the time of day and the extent of solar heating. A good example of boundary layer C_n^2 measurements [41] shows diurnal variations with peaks at local noon, dips during the neutral durations close to sunrise and sunset, and a near-constant value at night. The variations have to do with the characteristics of heat transfer between the dry soil and surrounding atmosphere. One can well imagine the dependence on local terrain, vegetation, and prevalent wind speed that will influence this process. Thus, for sharp mountain peaks the boundary layer effects are not prevalent by virtue of the relief above the surrounding terrain. Thermosonde daytime measurements of the structure constant profiles as a function of altitude showed a –4/3 dependence of C_n^2 on altitude [42]. However, with winds that cause mixing in the boundary layer, deviations to the said dependence are observed. The daytime measurements of C_n^2 are particularly relevant to deep space optical communications links. The line-of-sight to deep space probes from Mars and all outer planets involves extended daytime durations. Thus, future operational optical communications systems must devise strategies to successfully mitigate daytime turbulence effects in order to be viable. In contrast with the boundary layer, the free-atmosphere layer involves the altitudes in the vicinity of the

tropopause (15–17 km) and higher altitudes. C_n^2 at these altitudes is less well known, though measurements have been reported [43].

Based upon the measurements, empirical and parametric models of C_n^2 have been derived, and a good description of these models is found in [39]. The Hufnagel-Valley (HV) parametric model is widely used. This model includes an upper atmospheric part of 3–24 km that applies to both daytime and nighttime and can be rewritten as:

$$C_n^2(h) = 8.2\times10^{-16} W^2 \left(\frac{h}{10}\right)^{10} \exp(-h) + 2.7\times10^{-16} \exp\left(\frac{-h}{1.5}\right) \tag{3.4-7}$$

Here, h is the height in kilometers, and W is the root mean square (rms) wind speed in meters per second in the range 5–20 km above the ground, specifically

$$W^2 = \left(\frac{1}{15}\right)\int_5^{20} V^2(h)\,dh \tag{3.4-8a}$$

where $V(h)$ is the wind speed in meters per second is also given by the Bufton wind model [40]:

$$V(h) = \omega_s h + v_g + 30\exp\left[-\left(\frac{h-9400}{4800}\right)^2\right] \tag{3.4-8b}$$

where ω_s is the residual slew rate between the spacecraft and ground that can be neglected for deep space probes where good tracking can be assumed. v_g refers to the ground wind speed. By adding a boundary layer term to Eq. (3.4-7) above the model can be extended to include the boundary layer effects. Therefore, the HV model takes the form:

$$\begin{aligned} C_n^2(h) = {} & 8.2\times10^{-16} W^2 \left(\frac{h}{10}\right)^{10} \exp(-h) + 2.7\times10^{-16} \exp\left(\frac{-h}{1.5}\right) \\ & + A\exp\left(\frac{-h}{0.1}\right) \end{aligned} \tag{3.4-9}$$

where A represents the ground level structure constant value or $C_n^2(0)$. The parameters A and W are adjustable in order to correspond to a desired value of "seeing" and isoplanatism, as explained further below. An alternate model for C_n^2 is the CLEAR 1 Night Model that can be extrapolated to the ground invoking the –4/3 height dependence to represent day time turbulence as

described earlier. Figure 3-46 below shows a comparison of the HV and 2 × CLEAR 1 models to represent daytime refractive index structure constants.

The moments of the refractive index structure constant allow estimates of parameters for predicting the influence of the atmospheric turbulence on optical link performance. These are described in the chapters that follow. The dependence of the moments derived from C_n^2 is a path integral, with the path extending from the height of the receiver above sea level to the top of the atmosphere. Therefore, the manner in which atmospheric turbulence influences space-to-ground propagation relative to ground-to-space propagation is different. Consider for a moment that a laser beam originating from deep space spreads to hundreds or thousands of kilometers and far exceeds atmospheric characteristic spatial scales, whereas for an upward propagating laser beam originating from an optical communications ground station and transmitted to space, the beam diameter is expected to be within the inertial range. In a qualitative sense, this causes the uplink beams to be steered by large angular displacements whereas the same is not true for downlink beams.

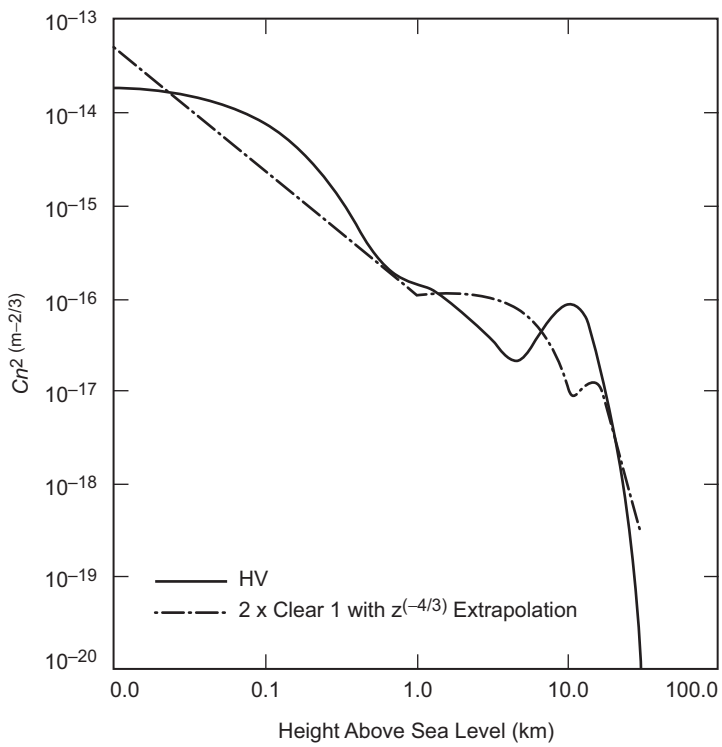

Fig. 3-46. Refractive index structure constant model derived using the Hufnagel-Valley and 2 x CLEAR 1 models. The CLEAR 1 model was extrapolated to the ground by a –4/3 dependence.

3.4.2 Atmospheric "Seeing" Effects

The atmospheric coherence diameter (also commonly referred to as the Fried parameter [44] or r_0 usually expressed in centimeters) is an important atmospheric parameter in determining optical link performance. Physically r_0 represents the spatial extent over which the phase of a propagating optical beam is preserved. For a plane wave, r_0 can be estimated from C_n^2.

$$r_0 = 1.67\left[\sec(\eta)k^2\int_{h_0}^{H} C_n^2(h)dh\right]^{-3/5} \tag{3.4-10}$$

where η represents the zenith angle of the observer, and k is the wave number defined as $2\pi/\lambda$ corresponding to the wavelength λ. This form of r_0 is applicable to the downlink beam. For the uplink beam, variations to this relation have been shown for the propagation of an assumed Gaussian beam intensity profile where r_0 increases with path length. As mentioned previously, the HV model parameters (such as A and W) can be adjusted in order to scale r_0 to desired values. Figure 3-47 shows the r_0 derived from the C_n^2 models discussed above, where the parameters A and W were adjusted to provide zenith r_0 values of 16 and 13.3 cm for the HV-models while the 2 × CLEAR 1 model was extrapolated to the ground by a –4/3 dependence on height yielded the smallest r_0 value of 9.5 cm at zenith.

These models provide a basis for predicting Fried parameters; however, as should be obvious from the discussions so far, the dependence on terrain, wind speed, topology, and solar illumination all together complicate the r_0 problem sufficiently to merit confirmation by measurement. Figure 3-48 shows a compilation of measured [39,45] r_0 values over mostly night, twilight, and dusk hours. These measurements were scaled to 1064 nm by the wavelength dependence indicated in Eq. (3.4-10). As shown in Figs. 3-48a and 3-48b, the r_0 measurements show very little dependence on altitude but show evidence of a relation to the relief.

An abundance of daytime measurements are found in the solar astronomy literature [46,47,48] where r_0 is extracted from a variety of solar irradiance and limb image motion measurements. Figure 3-49 shows a 2-year compilation of data measured at Sacramento Peak, New Mexico. The data are compared to the diurnal variation of r_0. A partial agreement is observed; however, note that the diurnal model is predicted for fully developed boundary layers.

One noteworthy difference between solar and stellar techniques for measuring r_0 is that the latter are usually not capable of making measurements in the vicinity of the Sun. Generally, stellar measurement systems are capable of observing daytime stars as close as 30 deg from the Sun in order to allow

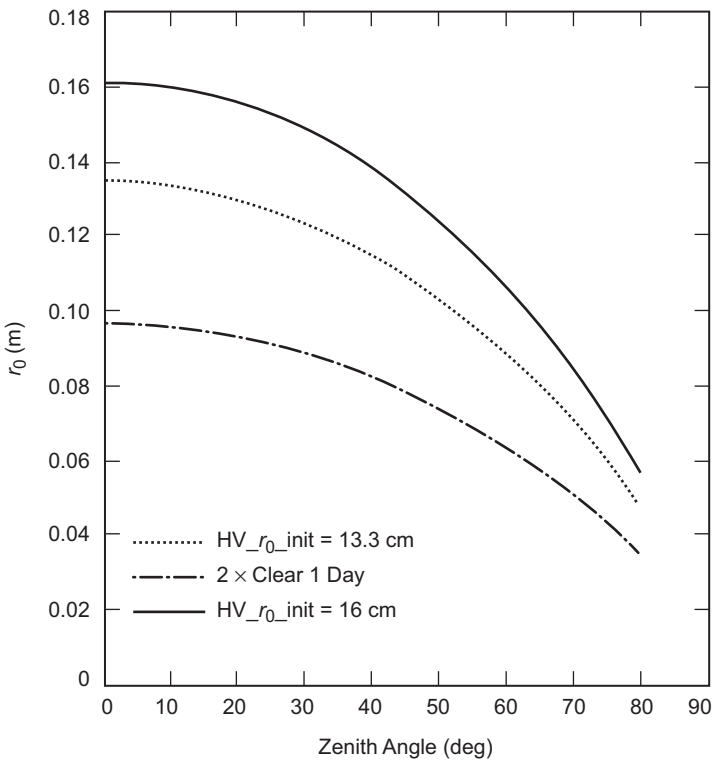

Fig. 3-47. Plots of r_0 versus zenith angle derived from the C_n^2 models discussed in 3.5.1. The Hufnagel-Valley models were scaled to provide zenith r_0 values of 13.3 and 16 cm, whereas the 2 × CLEAR 1 model extrapolated to the ground by the –4/3 dependence yields a zenith r_0 of 9.5 cm.

enough contrast in measured stellar images. Similarly solar observations are limited to direct observations of the Sun and cannot be used to look at zenith angles away from the Sun.

The beam perturbations associated with r_0 are also commonly referred to as atmospheric "seeing" effects with the "seeing being defined as $\sim \lambda / r_0$ expressed in angular units, or radians. Atmospheric "seeing" effects upon a deep space optical link are related to the fact that the diameter or Fried parameter presents a limiting aperture size to the laser beam wavefront. For a perfect optical collection system, the spot size in the focal plane to first order is determined by 2.44 $f\lambda/D$, with f and D representing the focal length and aperture diameter of the collection system. However, when the beam propagates through the atmosphere, D is replaced by r_0 so that first, the spot diameter at the focal plane is increased by the ratio D / r_0. This increase in focal

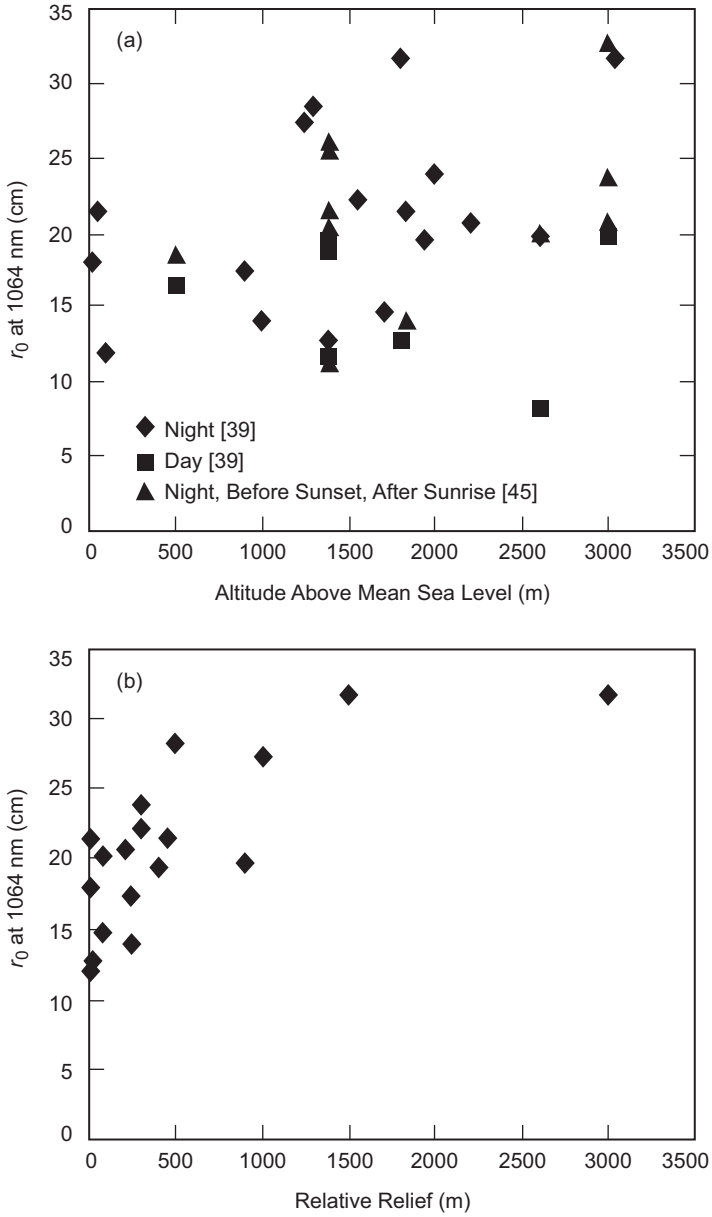

Fig. 3-48. (a) Distribution of r_0 values [39,45] as a function of height of location shows no correlation with altitude. (b) Measurements from [45] plotted as a function of the relief above the surrounding terrain where evidence of functional relationship seems apparent.

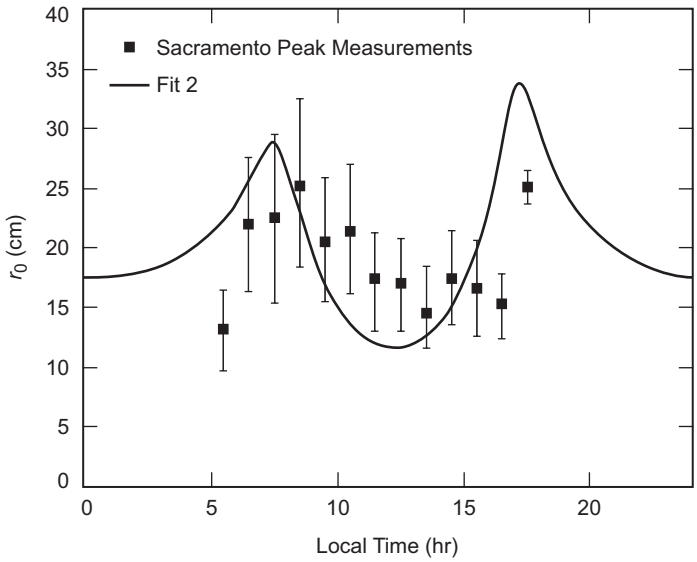

Fig. 3-49. Summary of r_0 obtained from solar observations [46], compared to the diurnal variation model. Note that the diurnal variation applies to measurements where the boundary layer is fully developed.

spot or atmospheric "blurring" increases the effective FOV required to collect all the laser signal photons. The two big disadvantages are (1) increased sky background noise contribution, especially for daytime links, and (2) increased detector area that could be bandwidth limiting. The latter problem is not insurmountable since detector sizes satisfying the FOV and bandwidths to support 10-Mbps class links are available. However, the former problem cannot be circumvented without the use of an adaptive optical system. Using adaptive optical systems in the daytime, very likely with an artificial guide star because the communications laser signal from the spacecraft will be too weak, poses a formidable challenge [49]. Conversely, being able to accommodate the turbulence-degraded FOV, since imaging is not required for communications, could greatly simplify matters. Alternatively, adaptive signal processing techniques using array detectors is a viable approach discussed later in Section 6.2.2. Detectors with adequate collection area do not suffer from turbulence in the nighttime when background light levels are sufficiently low. Furthermore, the background light penalty is really a product of the prevalent sky radiance and the "seeing" limited FOV or solid angle. Thus, if at large Sun-separation angles "seeing" is poor, the penalty on the optical communications system may not be very large; however, low Sun-separation angles combined with poor seeing present the worst case for the optical link performance.

Designs that address the worst-case condition will provide much better performance at other times. To cite an example, consider a spacecraft orbiting Mars. The farthest range between Earth and Mars occurs at solar conjunction when optical systems must communicate at Sun-separation angels as low as 3 deg in order to limit the outage to 30 days. Here of course, the spacecraft and the Sun rise at approximately the same time, and the sky radiance can be very high. If the ground-based receiver is operating under fully developed boundary layer conditions with worst seeing, performance is severely impeded. Furthermore, the time of day when the spacecraft rises has to be factored in while evaluating performance.

Next, some analysis is presented to further elaborate on the spot blurring due to atmospheric turbulence. Consider an ideal annular light-collection system with diameter D and obscuration ratio ε. The mean fraction $P(r)$ of the incident energy collected within the normalized detector radius $r \equiv a / \lambda F$, (a is the detector radius, and $F \equiv f / D$) is given, by the approximate relation [50,51]

$$P(r) = 2\pi r \int_0^1 \langle \tau(\rho,\varepsilon) \rangle J1(2\pi r\rho)\, d\rho \tag{3.4-11}$$

where $\langle \tau(\rho,\varepsilon) \rangle$ represents the time-averaged optical transfer function (OTF) of the annular optical system corresponding to a spatial frequency ρ with a linear obscuration ratio, ε and $J1$ is the first-order Bessel function of the first kind. The time-averaged OTF can further be expanded

$$\langle \tau(\rho,\varepsilon) \rangle = \tau_1(\rho,\varepsilon)\tau_a(\rho) \tag{3.4-11a}$$

Here $\tau_1(\rho,\varepsilon)$ is the OTF of the aberration free annular pupil, and $\tau_a(\rho)$ represents the effect of turbulence.

$$\tau_a(\rho) = \exp\left[-3.44\left(\frac{D\rho}{r_0}\right)^{5/3}\right] \tag{3.4-11b}$$

where a Kolmogorov model of atmospheric turbulence has been invoked.

$$\tau_1(\rho,\varepsilon) = \tau_1(\rho) + \varepsilon^2 \tau_1(\rho,\varepsilon) - \tau_{12}(\rho,\varepsilon) \tag{3.4-11c}$$

with

$$\tau_1(\rho) = \frac{2}{\pi\left(1-\varepsilon^2\right)}\left[\cos^{-1}\rho - \rho\left(1-\rho^2\right)^{1/2}\right], 0 \le \rho \le 1 \tag{3.4-11d}$$

$$\tau_{12}(\rho,\varepsilon) = \frac{2\varepsilon^2}{1-\varepsilon^2}, 0 \le \rho \le \frac{1-\varepsilon}{2}$$

$$\tau_{12}(\rho,\varepsilon) = \frac{2\varepsilon^2}{1-\varepsilon^2}\left[1 - \frac{1+\varepsilon^2}{2\pi\varepsilon^2\beta} - \frac{1}{\pi\varepsilon}\sin\beta + \frac{1-\varepsilon^2}{\pi\varepsilon^2}\tan^{-1}\left(\frac{1+\varepsilon}{1-\varepsilon}\tan\frac{\beta}{2}\right)\right],$$

$$\frac{1-\varepsilon}{2} \le \rho \le \frac{1+\varepsilon}{2} \qquad (3.4\text{-}11e)$$

$$\tau_{12}(\rho,\varepsilon) = 0,$$

otherwise

$$\beta = \cos^{-1}\left(\frac{1+\varepsilon^2-4\rho^2}{2\varepsilon}\right)$$

The ratio D/r_0 determines the quantity r required to collect a desired fraction of the signal energy where *r* is measured in units of λF. Adapting the daytime models represented in Fig. 3-47, where zenith-viewing r_0 values ranged from 9.5–16 cm and 5–8.5 cm for zenith angles of 70 deg. Table 3-8 below gives the approximate corresponding D/r_0 values that can be expected for a number of representative ground antennas.

Figure 3-50 shows a plot of the integral given by Eq. (3.4-11) for a number of the aperture diameters spanning the range of Table 3-8. Included in Fig. 3-50 is a plot for $D/r_0 \to 0$, or $r_0 >> D$, meaning no atmospheric turbulence with a diffraction-limited ideal optical system. So the curve with $D/r_0 \to 0$ and $\varepsilon = 0$ is simply the Airy pattern plot from diffraction theory that shows 84 percent of the energy corresponding to the dimensionless spot size of 1.22 in units of $1/\lambda F$, as expected. As the D/r_0 increases, the long term average spot size for encircling a given fraction of energy also increases as shown. Figure 3-50 shows that the dimensionless spot size required to encircle 84 percent of the energy can be approximated by the quantity D/r_0. This approximation gets

Table 3-8. The D/r_0 ratios for a number of large-aperture telescopes.

	D (m)	Obscuration (m)	D/r_0 Best Day	D/r_0 Worst Day
Hypothetical	10	1.4	62.5	200
Palomar	5	1	31.25	100
AEOS, Mt. Haleakala*	3.67	0.86	23	73.4
TMF	1	0.2	6.25	20

*AEOS = Advanced Electro-Optical System

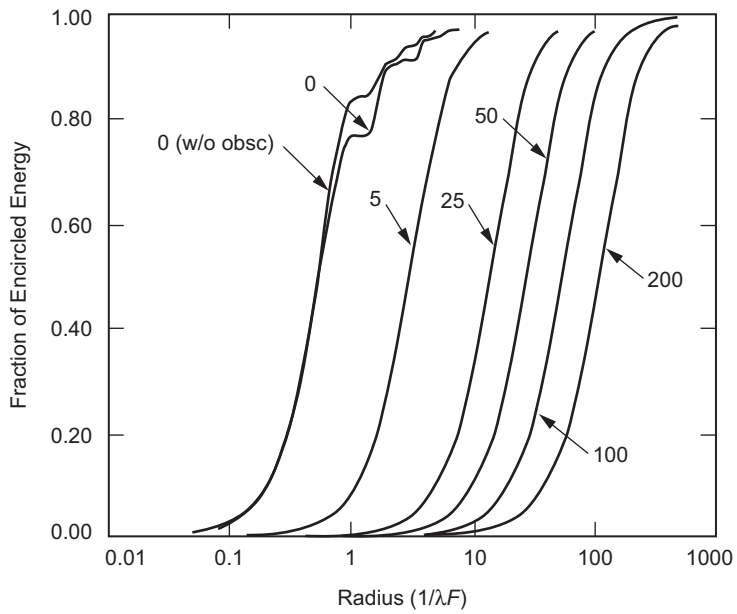

Fig. 3-50. Fraction of encircled energy versus radius at focal plane in units of 1/λ*F*, λ being wavelength and *F* being the focal ratio of the optical system with a circular aperture of diameter *D* with a central obscuration 20 percent of *D*. The labels indicate the D/r_0 ratio, with $D/r_0 = 0$ representing the diffraction-limited case. For comparison, a diffraction-limited unobscured circular aperture corresponding to an ideal Airy pattern is also included.

better as the D/r_0 increases For example, $D/r_0 = 200$ (the percent error in dimensionless spot size) is <3 percent, while for $D/r_0 = 5$ the percent error in dimensionless spot size is 15 percent. Thus, the FOV required for encircling 84 percent of the energy or the ratio of the detector diameter to the focal length is given by:

$$FOV_{84\%} \approx \frac{2\dfrac{D}{r_0}\lambda F}{f} \approx 2\frac{\lambda}{r_0} \tag{3.4-12}$$

where *f* is the focal length of the system, and the approximation confirms the simple assertion that the half-angle FOV required to collect on an average 84 percent of the signal energy is the atmospheric "seeing" λ/r_0. Thus, the more severe the turbulence and the smaller the r_0, the larger the FOV and corresponding solid angle required to gather 84 percent of the energy.

The discussion presented above for the mean encircled fraction of energy = 84 percent can be applied for any spot size along the abscissa in order to convert it to FOV, which in turn can be converted to solid angle in steradians using the relation:

$$\Omega = 2\pi\left(1 - \cos\frac{\Theta}{2}\right) \tag{3.4-13}$$

where, Θ is the FOV in radians. The conversion of the abscissa to FOV or solid angle will depend upon the focal ratio of the light collection system. Figure 3-51 shows an example light-collection system with a 5-m diameter collection aperture, a 20-percent obscuration, and a focal ratio of 16. The lower the focal plane loss (FPL) or the larger the fraction of encircled energy, the larger the solid angle. Imagining a vertical line through the plotted points shows that a 1.75-dB change in FPL results in a 5–7-dB change in solid angle.

For daytime optical links relying on groundbased reception, the dominant source of background is the sky radiance. Furthermore, the detected background noise is directly proportional to the solid angle. The significance of the plot of Fig. 3-51, therefore, is that by sacrificing a relatively small fraction

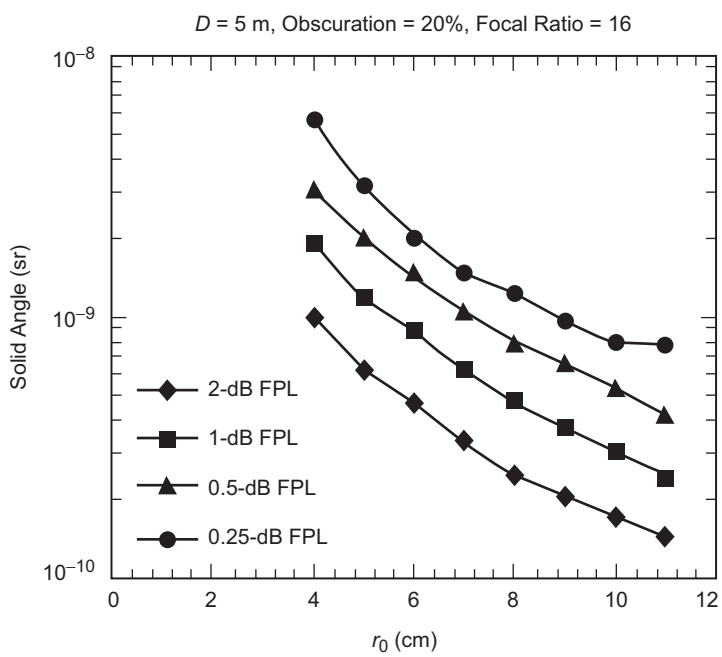

Fig. 3-51. Dependence of solid angle upon the Fried parameter r_0 for collecting 63, 80, 89, and 95 percent of encircled energy or equivalently a 2-dB focal plane loss (FPL), 1-dB, 0.25 dB, and 0.5 dB FPL.

of signal a much larger amount of background can be reduced, thereby increasing the overall channel capacity of the link. Thus, in addition to using optical filtering and polarization discrimination for rejecting background photons incident on the detector, tailoring the detector solid angle provides an additional means of discriminating against background photons. At night, on the other hand with background light levels being relatively low (except when a planet or celestial object also intersects the detector FOV), maximizing the solid angle appears to be optimal since this allows maximum signal collection with a negligible increase in background.

3.4.3 Optical Scintillation or Irradiance Fluctuations

Perturbations of the turbulent atmosphere on received laser beams cause interference so that a point detector placed in the path of the beam will alternately see patches of constructive and destructive interference causing swings in the detected irradiance. These irradiance fluctuations are characterized by a scintillation index (SI), σ_I^2 defined as:

$$\sigma_I^2 = \frac{\left\langle I^2 \right\rangle - \left\langle I \right\rangle^2}{\left\langle I \right\rangle^2} \tag{3.4-14}$$

where $\left\langle I \right\rangle$ represents the ensemble averaged irradiance of the received laser signal. As Eq. (3.4-3) shows, the SI is the variance of the irradiance normalized by its mean. The scintillation index can be expressed as:

$$\sigma_I^2 = \exp\left(4\sigma_\chi^2\right) - 1 \tag{3.4-15}$$

where σ_χ^2 is the variance of the log amplitude that can be expressed in terms of C_n^2 by the relation:

$$\sigma_\chi^2 = 0.56k^{7/6}\sec(\eta)^{11/6}\int_0^L C_n^2(h)(L-h)^{5/6}dh \tag{3.4-16}$$

The relation above applies well to the downlink communications from deep space. However, for uplink, more exact Gaussian beam formulations presented in reference [40] can be used. These estimations are reasonable as long as the weak turbulence approximations are valid. For severe turbulence or large airmass, SI does not continue to increase monotonically. Saturation eventually sets in, and the SI can be estimated [52] by heuristic models.

It is important to recognize that the irradiance fluctuations predicted by Eq. (3.4-16) and its variations apply to a point detector. For viable photon-

starved optical communication links from deep space, relatively large collection apertures (5–10 m) will be utilized for gathering a sufficient number of detectable photons. As a result, the speckle features distributed over the aperture and undergoing random constructive and destructive interference average out to a large extent. Aperture averaging theory [53] predicts a factor A for a plane wave traversing a horizontal atmospheric path:

$$A = \left[1 + 1.062\left(\frac{kD^2}{4L}\right)\right]^{-7/6} \tag{3.4-17}$$

Thus, the irradiance fluctuations or σ_I^2 predicted for a point detector will be reduced by the factor A for a collection aperture diameter D and wave number $k = 2\pi / \lambda$, λ being the wavelength and L being the path traversed.

Figure 3-52 shows the dependence of A upon L for a few different values of D. It is apparent that the larger the diameter the greater the impact of aperture averaging in reducing the irradiance fluctuations or scintillation.

While one can "translate" a horizontal atmospheric path with assumed fixed turbulence structure or C_n^2 into an equivalent slant or zenith path airmass, this approach to predicting the effects of aperture averaging on a downlink signal is

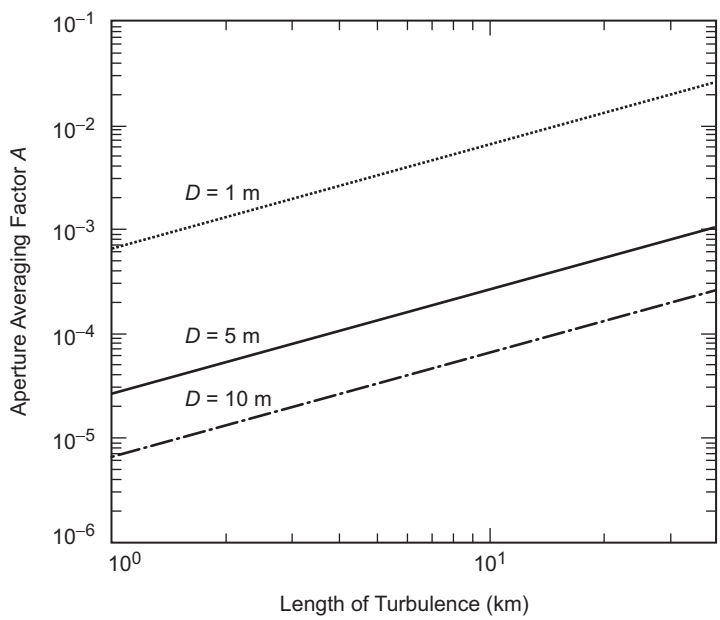

Fig. 3-52. Aperture averaging factor dependence on horizontal atmospheric path length for a number of different aperture sizes.

somewhat speculative. An expression was derived for the space-to-ground aperture averaging factor [54] that allows taking into account the C_n^2 profile and is given by:

$$A = \frac{1}{1 + A_0^{-1}\left(\dfrac{D^2}{\lambda h_0 \sec\theta}\right)^{7/6}} \tag{3.4-18}$$

where θ represents the zenith angle, $A_0 \approx 1.1$, and h_0 is given by

$$h_0 = \left[\frac{\int_{\text{path}} dh C_n^2(h) h^2}{\int_{\text{path}} dh C_n^2(h) h^{5/6}}\right]^{6/7} \tag{3.4-19}$$

This relation takes into account the slant range through the atmosphere and permits the modeling of the atmospheric refractive index structure function. Figure 3-53 shows the dependence of the aperture-averaging factor for a number of different aperture diameters using the approximation represented by Eq. (3.4-18). Surface C_n^2 is given by $A = 10^{-13}$ for an observer located at sea level with a 4-m/s upper-atmospheric wind speed. Changing the altitude did not provide any significant improvement in *A*, and the sea-level estimation below can be used as the worst case. Note that this prediction provides additional improvement in the aperture-averaging factor and is more representative for a true downlink path.

The net result of the predictions is that for downlink signal reception, the large collection-aperture size needed to gather sufficient photons also provides a large mitigation of the irradiance fluctuations experienced by the detector. The reduction in normalized variance of the irradiance has also been analyzed [55] as a function of the ratio of the aperture diameter D/r_0 and shown to decrease monotonically as *D* increases relative to r_0.

Comparisons of experimental measurements with theory are shown in Fig. 3-54. The measurements were performed over a 45-km mountain-top-to-mountain-top horizontal atmospheric path at an average altitude of 2 km. In Fig. 3-54, the solid lines were obtained by using theoretical expressions [40] for a plane, spherical wave propagating through turbulence. The data represented by the diamonds was obtained [56] by limiting the pupil at the Coude aperture plane of a 0.6-m telescope at Table Mountain, California, while transmitting an 811-nm laser beam with a 250-μrad beam divergence from Strawberry Peak near Lake Arrowhead, California. The triangles were obtained [57] during a 150-km laser-communication link demonstration between Haleakala and

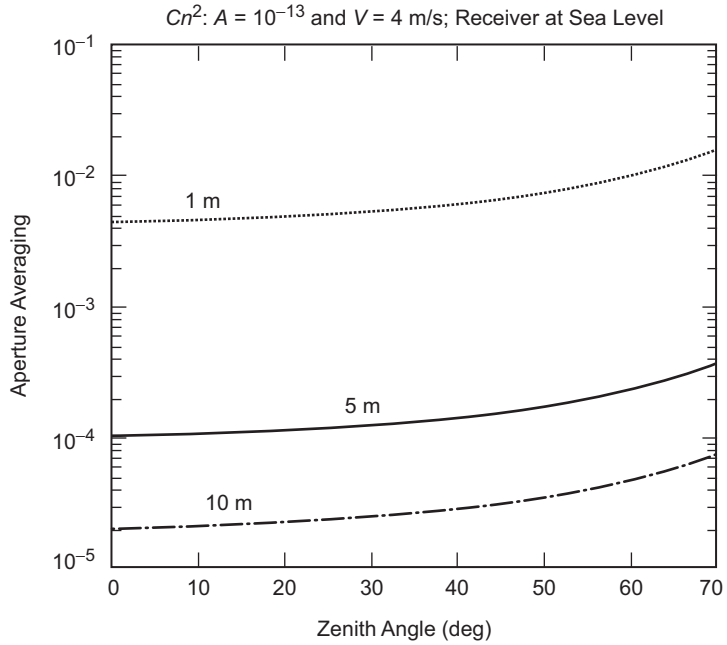

Fig. 3-53. Aperture averaging factor dependence on horizontal atmospheric path length for 1-m, 5-m, and 10-m aperture sizes for a receiver at sea level, with 4 m/s upper-atmospheric wind speed, and *A* of 10^{-13}.

Mauna Kea in Hawaii. The data labeled SP1998 (open squares) were obtained [58] using an 8-cm spotting telescope at Strawberry Mountain, California, while transmitting a 780-nm laser to Table Mountain, California. Finally, the data labeled TMF 1998 and Aug/Sep 2000 were both obtained [58, 59] using a narrow beam-divergence (22-μrad) beam transmitted from Strawberry Mountain, California and received at Table Mountain, California using the full aperture of the 60-cm telescope at Table Mountain. All the data are presented as a plot of the aperture averaging factor versus the Fresnel number. Measurements suggest that the aperture averaging achieved for the horizontal paths are generally better than theory predicts. The wide spread in the TMF 1998 and August–September 2000 factors is partially attributed to the narrowness of the beam so that the beam footprint at Table Mountain just overfills the telescope (0.9-m beam footprint versus 0.6-m aperture) and beam jitter contributes to additional irradiance fluctuations.

An interesting approach being considered for providing large effective aperture on the ground is to use an array of smaller telescopes [60]. In this approach, each individual smaller receiving aperture will have greater

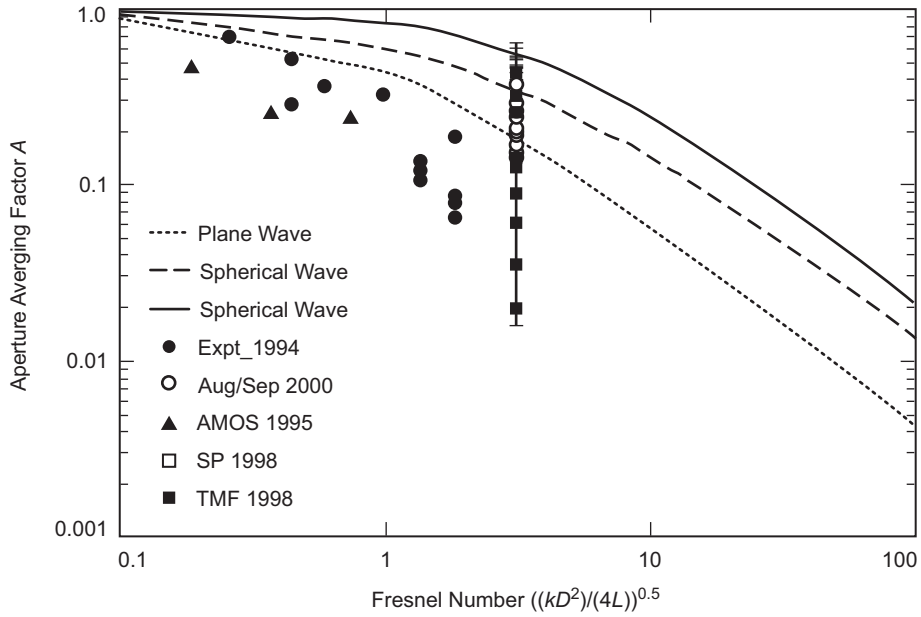

Fig. 3-54. Comparison of some horizontal path aperture averaging measurements compared to theory.

irradiance fluctuations; however, the signal-combining schemes devised for arrayed collection will average signal in the electronic domain.

Irradiance fluctuations must be mitigated on uplink lasers used for optical communications whether their purpose is to serve as a pointing reference for sending command data. At the time of writing this text, the experience with uplink lasers to deep space was very limited, with the Galileo Optical Experiment (GOPEX) [61] being the only reported demonstration. Here pulsed lasers were received by the Solid State Imaging (SSI) camera during the Galileo spacecraft's cruise to Jupiter. During this experiment, uplink scintillation of the laser beam was verified, and a nominal SI value of 0.69 was obtained over several days of transmission. This value of SI fell between those predicted by the weak-turbulence theory and the strong turbulence theory. Limited camera dynamic range coupled with uncertainties in synchronizing the laser pulses with camera framing limited data analysis and fitting measurements to the expected lognormal statistics. Furthermore the fades sensed by the camera cannot unambiguously be associated with scintillation since attitude variations of the spacecraft, and atmospheric turbulence induced beam wander (discussed below) could have contributed to the fades.

Uplink scintillation or normalized variance σ_I^2 was measured for the Low Power Atmospheric Compensation Experiment [62] (LACE) satellite where

retro-reflected links with σ_I^2 values ranging between 0.08 and 0.2 were measured. Furthermore, the temporal power spectral density showed 30 times less contribution at frequencies greater than 100 Hz compared to 1 Hz. The Relay Mirror Experiment [63] (RME) also used retro-reflectors on a near-Earth orbiting satellite to establish optical links. Scintillation indices, σ_I^2, ranging from 0.09 to 0.67 at frequencies ranging from 25 to 400 Hz were reported. The increase in higher frequency contributions in the latter demonstration is noteworthy, though no space-platform jitter results were provided in either of the two retro-reflector space-to-ground links cited.

A geostationary Earth orbit (GEO) laser communications demonstration (GOLD) reported [64,65] scintillation indices of 0.18 or better. GOLD also demonstrated that, by using multiple mutually incoherent beams, the scintillation could be reduced due to an averaging out of the fluctuations. Thus for GOLD, a four-beam 514.5-nm multi-beam uplink was demonstrated that showed a 1/N reduction in scintillation for an N-beam beacon. During the GOLD experiment, the SI values reported were 0.12 for two beams and 0.045 for four-beams.

Figure 3-55 presents a graphical summary of SI values measured during a horizontal path experiment [59]. A reduction in SI with increasing number of co-propagating beams is observed for all three nights that observations were conducted. Overall average reduction factors of 3, 3.2, and 3.7, respectively, were achieved for June 28, 29, and 30, respectively. In results reported elsewhere [66], over a 5.4-km range with nine co-propagating argon laser beams, the predicted reduction was shown to depend on the severity of atmospheric turbulence or Rytov variance. The beam-propagation simulation reported indicates as much as a 10-fold reduction for Rytov variances between 0.4 and 0.5 and a 3-fold to 4-fold reduction for Rytov variance close to 0.2.

From a systems design standpoint, the statistics of the irradiance fluctuations seen by a point detector for either the uplink or downlink obey lognormal statistics, notwithstanding deviations that may be encountered under strong turbulence. However, what is the nature of irradiance fluctuations with the mitigation strategies discussed above (namely, aperture averaging for the downlink and multi-beam averaging for the uplink)? The central limit theorem would dictate that, with enough averaging, the fluctuations should reduce to Gaussian; however, the log-normal distribution is somewhat unique in this sense and displays slow convergence [67, 68].

Consequently, assuming that the residual scintillation-induced fade statistics for an optical communications receiving system is log normal, whether in space receiving a multiple beam or on the ground receiving through a large aperture, may be adequate for design purposes.

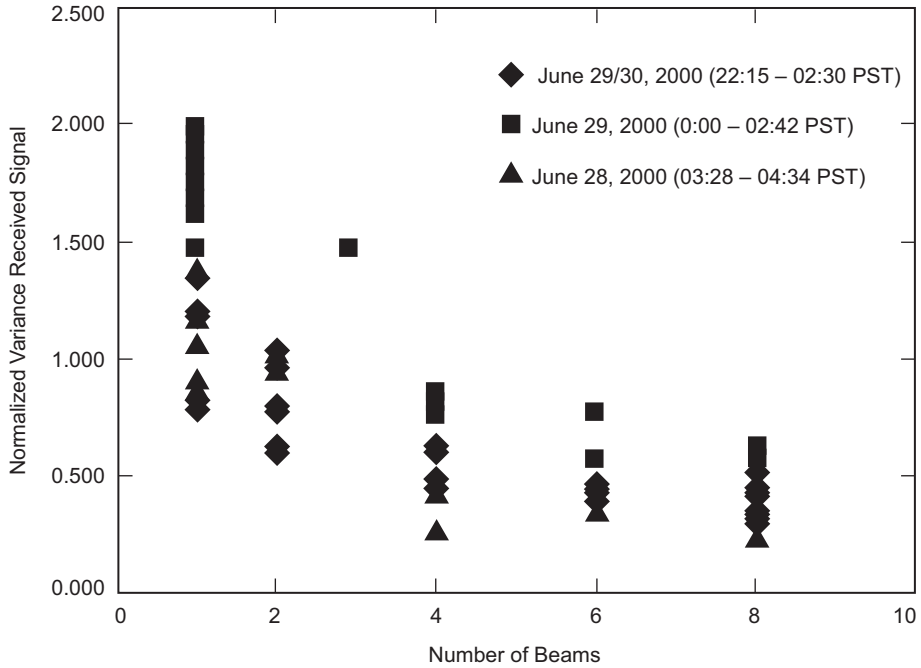

Fig. 3-55. Reduction in scintillation index as a result of multiple-beam incoherent averaging.

3.4.4 Atmospheric Turbulence Induced Angle of Arrival

The atmospheric turbulence induces distortions on the laser beam wavefront. For astronomical imaging applications, adaptive optics systems are being increasingly used to reconstruct the wavefront. For deep space optical communication, this may be a distinct possibility in the future; however, the present discussion is limited to systems that do not rely on an adaptive optical system. One of the consequences of the atmospheric distortion is "image motion" in the focal plane, and this is caused by fluctuations in the angle of arrival. In considering the effect of angle-of-arrival fluctuations on deep space optical communication links, a distinction between the downlink and uplink is needed.

The downlink is collected through a large effective aperture. Furthermore, it was pointed out in 3.4.2 that the detector FOV is restricted in order to reject excessive background from sky radiance and scattering. Imagine, therefore, the spot encircling the signal energy at the focal plane moving around so that at any instant a fraction of the encircled energy is blocked by the field stop. The situation described is shown in Fig. 3-56 where the circle represents the inner edge of the field stop, and the blurred spot represents the long-term averaged

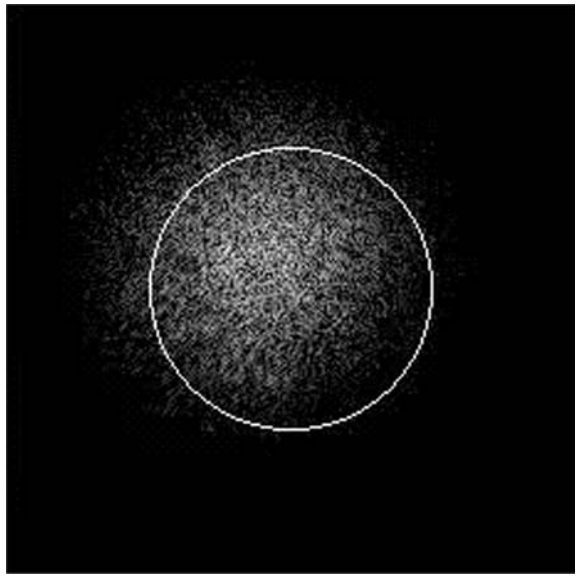

Fig. 3-56. Spatial distribution of mean laser energy averaged over many pulses with respect to the detector field-of-view depicted by the circle.

spatial distribution of the signal. A net loss of signal, with degradation of the optical link performance, will result. The situation can be greatly improved by having a simple correction system comprised of a two-axis fast-steering mirror located at the pupil image plane to actively compensate for the atmosphere-induced angle-of-arrival fluctuations. Note that correction for tilt does not compensate for higher order aberrations in the received beam; however, for optical-communication links, it is adequate since collecting the maximum possible signal energy is the intent. The implications of not having to correct for higher order aberrations is that a much lower bandwidth tracking system can be implemented.

A rather simplified form of the angle-of-arrival fluctuations that is independent of the wind profile is given by [40]

$$\sigma_\beta^2 = 2.914\left[\int_{h_0}^{H} C_n^2(h)dh\right]D^{-1/3}\sec(\eta) \tag{3.4-20a}$$

where σ_β represents the rms angle of arrival jitter. This can be further simplified using Eq. (3.4-10) to yield:

$$\sigma_\beta^2 = 0.170\left(\frac{\lambda}{D}\right)^2\left(\frac{D}{r_0}\right)^{5/3} \tag{3.4-20b}$$

With an r_0 of 10 cm and a wavelength of 1.064 μm, for example, the atmosphere-induced rms jitter, σ_β, will be approximately 2 μrad for a 5-m to 10-m collection aperture diameter, *D*, increasing to 3 μrad for *D* decreasing to 1 m. For example, a collection system with a 5-m diameter and an effective focal length of 80 m (i.e., an *F* ratio of 16 will result in the blur diameter required to enclose 84 percent of the energy of 1.7 mm according to the relations used in Eq. 3.4-12) above. At the same time, the angle-of-arrival fluctuations will cause rms spot displacements of 160 μrad. Therefore, the peak displacement (assuming a Gaussian distribution of the angle-of-arrival fluctuations) can be ± 0.48 mm, which is a significant fraction of the detector size to collect 84 percent of the energy. The need for tracking out the angle of arrival jitter or tilt error using a two-axis fast steering mirror becomes a requirement for reasonable performance. The photon-starved nature of the link may not readily allow for providing adequate signal-to-noise ratio at the desired update rate [70] required to compensate for the tilt. This problem can be further exaggerated by the presence of large amounts of background. Therefore, the design drivers here are methods of sacrificing minimal amounts of communication signal, while at the same time devising a means of getting an error signal derived from the mean spatial distribution of photons in the focal plane. This strongly suggests a class of photon-counting detectors that can be configured as a quadrant or array of detectors.

On the uplink, the atmosphere-induced beam wander can be conceived of as degrading the Strehl of the laser beam transmitted so that the on-axis energy would undergo fluctuations even if the beacon were pointed correctly at the distant spacecraft. By uplinking multiple beams as described earlier, some averaging of the random beam steering due to the atmosphere can in principal be realized, though quantifying this without running a simulation is not possible and is beyond the scope of the present discussion. The fades on the uplink are a combination of the residual scintillation and beam wander effects after multi-beam averaging, combined with superimposed irradiance fluctuations from receiver platform attitude variations and vibrations. The update rates at which the uplink beacon is sampled for command data or for the purposes of a pointing reference have a large effect on beacon design. One of the scenarios for pointing an uplink is to blind point to the spacecraft based on ephemeris predicts.

In this section an attempt was made to provide a brief introduction to the impact of the atmosphere on a groundbased optical-communications receiving and transmitting system. References cited and not cited provide much more in-depth analysis and insight into each of the atmospheric processes described, and an improved understanding will certainly bring forth better solutions. As has been mentioned already, adaptive optics offers a potentially powerful solution to mitigating many of the atmospheric degradations to the optical link. In the

near future planned demonstrations of groundbased reception of laser communication from deep space [60] hold the promise of real data to not only assess the true impact of atmospherics but also provide atmospheric statistics that lend credibility to how often links with a given performance can be operated.

References

[1] W. B. Rossow, F. Mosher, E. Kinsella, A. Arking, M. Desbois, E. Harrison, P. Minnis, E. Ruprecht, G. Seze, C. Simmer, and E. Smith, "ISCCP Cloud Algorithm Intercomparison," *Journal of Climate and Applied Meteorology*, vol. 24, pp. 877–903, 1985.

[2] United States National Oceanic and Atmospheric Administration National Climate Data Center website http://www.ncdc.noaa.gov

[3] Northrop Grumman (TASC), Chantilly, Virginia, a division of Northrop Grumman: http://www.tasc.com/

[4] *Surface Weather Observations and Reports*, Federal Meteorological Handbook (FMH) Number 1, Office of the Federal Coordinator for Meteorological Services and Supporting Research, Silver Spring, Maryland, December 1995.

[5] S. Piazzolla and S. Slobin, "Statistics of Link Blockage Due to Cloud Cover for Free-Space Optical Communication Using NCDC Surface Weather Observation Data," *Proceedings of the SPIE*, vol. 4635, pp. 138–139, 2002.

[6] S. Piazzolla, S. Slobin, and E. Amini, *Cloud Coverage Diversity Statistics for Optical Communications in the Southern United States*, Publication 00-13, Jet Propulsion Laboratory, Pasadena, California, November 30, 2000.

[7] K. E. Wilson and J. V. Sandusky, "Development of a 1-m Class Telescope at TMF to Support Optical Communications Demonstrations," *Proceedings of the SPIE*, vol. 3266, San Jose, California, pp. 146–152, January 1998.

[8] *Cloud Free Line of Sight Study, JPL Contract No. 1248595*, Final Review, Northrop Grumman (TASC), Chantilly, Virginia, September 25, 2003.

[9] R. P. Link, R. J. Allis, and M. E. Craddock, "Mitigating the Effects of Clouds On Optical Communications," Photonics West, 24–29 January 2004, San Jose, California, *Free Space Laser Comm Technologies XVI, Proceedings of the SPIE*, vol. 5338 [G. S. Mecherle, C. Y. Young, and J. S. Stryj, editors], pp. 223–232, June 2004.

[10] A. S. Jursa (sci. ed.), *Handbook of Geophysics and the Space Environment* (NTIS Doc # ADA16700), Air Force Geophysics Laboratory, Hanscom Air Force Base, Massachusetts, 1985.

[11] D. R. Bates, "Rayleigh Scattering by Air," *Planetary Space Science*, vol. 32, pp. 785–790, 1984.

[12] H. C. van de Hulst, *Light Scattering by Small Particles*, Wiley, New York, 1957. (also Dover Publications, January 1, 1982)

[13] *AFGL Atmospheric Constituent Profiles (0–120 km)*, AFGL-TR-86-0110, Air Force Geophysics Laboratory, Hanscom Air Force Base, Massachusetts, 1986.

[14] A. Berk, L. S. Bernstein, and D. C. Robertson, *MODTRAN: A Moderate Resolution Model for LOWTRAN 7*, Air Force Geophysics Laboratory Technical Report GL-TR-89-0122, Hanscom Air Force Base, Massachusetts, 1989.

[15] S. A. Clough, F. X. Kneizys, and R. W. Davies, "Lineshape and Water Vapor Continuum," *Atmospheric Research*, vol. 23, p. 229, 1989.

[16] J. V. Dave, "Multiple Scattering in a Non-Homogenous Rayleigh Atmosphere," *Journal of Atmospheric Science*, vol. 22, p. 273, 1965.

[17] O. Dubovik, B. N. Holben, T. F. Eck, A. Smirnov, Y. J. Kaufman, M. D. King, D. Tanre, and I. Slutsker, "2002: Variability of Absorption and Optical Properties of Key Aerosol Types Observed in Worldwide Locations," *Journal of Atmospheric Science*, vol. 59, pp. 590–608, 2002.

[18] J. M. Rosen, "Stratospheric Dust and Its Relationship to the Meteoric Influx," *Space Science Review*, vol. 9, p. 59, 1969.

[19] R. P. Turco, R. C. Whitten, and O. B. Toon, "Stratospheric Aerosols: Observation and Theory," *Rev. Geophysics and Space Research*., vol. 20, no. 2, pp. 233–279, 1982.

[20] H. Weichel, *Laser Beam Propagation in the Atmosphere*, SPIE Optical Engineering Press, Bellingham, Washington, 1990.

[21] S. Q. Duntley, A. R. Boileau, and R. W. Preisendorfer, "Image Transmission by the Troposphere, I," *Journal of the Optical Society of America*, vol. 47, no. 6, pp. 499–506, 1957.

[22] S. Q. Duntley, R. W. Johnson, and J. I. Gordon, *Airborne Measurements of Optical Atmospheric Properties, Summary and Review III*, SIO Reference 79-5, AFGL-TR-78-0286, NTIS ADA 073-121, Scripps Institution of Oceanography, Visibility Laboratory, University of California, San Diego, California, 1978.

[23] *Atmospheric Transmittance/Radiance: Computer Code Lowtran 6*, AFGK-TR-83-0187, Air Force Geophysics Laboratory, Hanscom Air Force Base, Massachusetts, 1983.

[24] R. C. Ramsey," Spectral Irradiance from Stars and Planets, above the Atmosphere from 0.1 to 100 Microns," *Applied Optics*, vol. 1, pp. 465–471, 1962.

[25] J. Katz, "Planets as Background Noise Sources in Free Space Optical Communications," *The Telecommunications and Data Acquisition Progress Report 42-85, January–March 1986*, Jet Propulsion Laboratory, Pasadena, California, May 15, 1986.
http://ipnpr.jpl.nasa.gov/progress_report/

[26] *Surface Models of Mars (1975)*, NASA SP-8020, National Aeronautics and Space Administration, Washington, District of Columbia, 1975.

[27] K. Lumme and E. Bowell, "Radiative Transfer in the Surfaces of Atmosphereless Bodies," Astron. J. "I Theory," vol. 86, 1694–1704, 1981; "II Interpretation of Phase Curves," vol. 86, 1705–1771, 1981.

[28] K. Shaik and M. Wilhelm, *Ground Based Advanced Technology Study (GBATS); Optical Subnet Concepts for the DSN*, Jet Propulsion Laboratory, D-11000, Release I (internal document), Jet Propulsion Laboratory, Pasadena, California, August 5, 1994.

[29] K. W. Kobayashi, J. E. Fernandez, J. H. Kobayashi, M. Leung, A. K. Oki, L. T. Tran, M. Lammert, T. R. Block, and D. C. Streit, "A DC-3 GHz Cryogenic AlGaAs/GaAs HBT Low Noise MMIC Amplifier with 0.15 dB Noise Figure," *International Electron Devices Meeting, 1999, IEDM Technical Digest*, cat. no. 99CH36318: 775–8, IEEE, Piscataway, New Jersey, 1999.

[30] M. Moszynski, W. Czarnacki, M. Szawlowski, B. L. Zhou, M. Kapusta, D. Wolski, and P. Schotanus "Performance of Large-Area Avalanche Photodiodes at Liquid Nitrogen Temperature," *IEEE Transactions on Nuclear Science*, vol. 49, no. 3, pp. 971–976, June 2002.

[31] F. Amoozegar, R. Cesarone, S. Piazzolla, L. Paal, and R. Emerson, "Performance Analysis and Comparison of Clustered and Linearly Dispersed Optical Deep Space Network," *Proceedings of 5th International Symposium on Reducing the Cost of Spacecraft Ground systems and Operations (RCSGSO)*, July 8–11, 2003, Pasadena, California, Jet Propulsion Laboratory, 2003.
http://descanso.jpl.nasa.gov/RCSGSO

[32] L. Stepp, L. Daggert, and P. Gillett, "Estimating the Costs of Extremely Large Telescopes." *Proceedings of the SPIE*, vol. 4840, *Future Giant Telescopes*, editors: J.R.P. Angel and R. Gilmozzi, pp. 309–321, 2003.

[33] W. B. Rossow, F. Mosher, E. Kinsella, A. Arking, M. Desbois, E. Harrison, P. Minnis, E. Ruprecht, G. Seze, C. Simmer, and E. Smith, "ISCCP Cloud Algorithm Intercomparison." *Journal of Climate and Applied Meteorology*, vol. 24, pp. 877–903, 1985.

[34] A. Biswas, and S. Piazzolla, "Deep-Space Optical Communications Downlink Budget from Mars: System Parameters," *The Interplanetary Network Progress Report, 42-154, April–June 2003*, pp. 1–38, August 15, 2003.
http://ipnpr.jpl.nasa.gov/progress_report/

[35] I. Tatarski, *Wave Propagation in A Turbulent Medium*, McGraw-Hill, New York, translated by R. A. Silverman, 1961.

[36] A. Ishimaru, *Wave Propagation and Scattering in Random Media*, IEEE Press, Piscataway, New Jersey, 1997.

[37] J. Stroebehn, ed. *Laser Beam Propagation in the Atmosphere*, Springer, New York, 1978.

[38] R. L. Fante, "Wave propagation in random media: a systems approach," *Progress in Optics XXII*, E. Wolf ed., Elsevier, New York, pp. 341–398, 1985.

[39] R. R. Beland, "Propagation through Atmospheric Optical Turbulence," *The Infrared & Electro-Optical Systems Handbook*, vol. 2, F. G. Smith, ed., SPIE Optical Engineering Press, Bellingham, Washington, 1993.

[40] L. C. Andrews and R. L. Phillips, *Laser Beam Propagation through Random Media*, SPIE Optical Engineering Press, Bellingham, Washington, pp. 157–229, 1998.

[41] D. L. Walters and K. E. Kunkel, "Atmospheric Modulation Transfer Function for Desert and Mountain Locations: the Atmospheric Effects on r_0," *Journal of the Optical Society of America*, vol. 71, pp. 397–405, 1981.

[42] J. H. Brown, R. E. Good, P. M. Bench, and G. Faucher, *Sonde measurements for comparative measurements of optical turbulence*, Air Force Geophysical Laboratory, AFGL-TR-82-0079, NTIS: ADA118740, Hanscom Air Force Base, Massachusetts, 1982.

[43] R. E. Goof, R. R. Beland, E. A. Murphy, J. H. Brown and E. M. Dewan, "Atmospheric Models of Optical Turbulence," *Modeling of the Atmosphere, Proceedings of the SPIE*, vol. 928, pp. 165–186, 1988.

[44] D. L. Fried, "Statistics of Geometric Representation of Wavefront Distortion," *Journal of the Optical Society of America*, vol. 55, pp. 1427–1435, November 1965.

[45] D. L. Walters and L. W. Bradford, "Measurements of r_0 and θ_0: Two Decades and 18 Sites, *Applied Optics*, vol. 36, pp. 7876–7886, 1997.

[46] P. N. Brandt, H. A. Mauter, and R. Smartt, "Day-Time Seeing Statistics at Sacramento Peak Observatory," *Astronomy and Astrophysics*, vol. 188, pp. 163–168, 1987.

[47] E. Seykora, "Solar Scintillation and Monitoring of Solar Seeing," *Solar Physics*, vol. 145, pp. 389–397, 1993.

[48] J. M. Beckers, E. Leon, J. Mason, and L. Wilkins, "Solar Scintillometry: Calibration of Signals and Its Use for Seeing Measurements," *Solar Physics*, vol. 176, pp. 23–36, 1997.

[49] K. E. Wilson, M. Troy, M. Srinivasan, B. Platt, V. Vilarotter, M. Wright, V. Garkanian, and H. Hemmati, "Daytime Adaptive Optics for Deep Space Communications," *Space Activities and Cooperation Contributing to All Pacific Basin Countries (10th ISCOPS)*, vol. 117, *Advances in the Astronautical Sciences* [eds. P. M. Bainum, L. Furong, and T. Nakajina] American Astonautical Society, San Diego, CA 92198, pp. 481–491, 2004.

[50] V. N. Mahajan and B. K. C. Lum, "Imaging through atmospheric turbulence with annular pupils," *Applied Optics*, vol. 20, pp. 3233–3237, 1981.

[51] V. N. Mahajan, *Aberration Theory Made Simple*, vol. 6 (TT-6) of *Tutorial Texts in Optical Engineering*, series editor. D. O' Shea, SPIE Optical Engineering Press, Bellingham, Washington, p. 74, July 1991.

[52] L. C. Andrews, R. L. Phillips, C. Y. Hopen, and M. Al-Habash, "Theory of Optical Scintillation," *Journal of the Optical Society of America A*, vol. 16, pp. 1417–1479, 1999.

[53] J. Churnside, "Aperture Averaging of Optical Scintillations in the Turbulent Atmosphere," *Applied Optics*, vol. 30, no. 15, pp. 1982–1994, 1991.

[54] H. T. Yura and W. G. Mckinley, "Aperture Averaging for Space-to-Ground Optical Communications Applications," *Applied Optics*, vol. 22, pp. 1608–1609, 1983.

[55] R. M. Gagliardi and S. Karp, *Optical Communications*, Second Edition, John Wiley & Sons, p. 298, 1995.

[56] K.E. Wilson, A. Biswas, S. Bloom, and V. Chan, "Effect of Aperture Averaging on a 570 Mbps 42 km Horizontal Path optical Link," *Atmospheric Propagation and Remote Sensing IV, Proceedings of the SPIE*, ed., J. Christopher Dainty, vol. 2471, pp. 244–253, April 1995.

[57] V. Chan and S. Bloom, "Results of 150 km, 1 Gbps Lasercom Validation Experiment Using Aircraft Motion Simulator," *Free-Space Laser Communications Technologies X, Proceedings of the SPIE*, Ed., G. Stephen Mecherle, vol. 2699, pp. 60–70, 1998.

[58] A. Biswas and S. Lee, "Ground-to-Ground Optical Communications Demonstration," *Telecommunications and Mission Operations Progress Report, 42-141, January–March 2000*, pp. 1–31, May 15, 2000. http://ipnpr.jpl.nasa.gov/progress_report/

[59] A. Biswas and M. W. Wright, "Mountain-Top-to-Mountain-Top Optical Link Demonstration: Part I," *The Interplanetary Network Progress Report 42-149, January–March*, pp. 1–27, May 15, 2002. http://ipnpr.jpl.nasa.gov/progress_report/

[60] B. L. Edwards, et al., "Overview of the Mars Laser Communications Demonstration Project," Paper 2003-6417, *AIAA Space 2003 Conference* Long Beach, California, September 23–25, 2003.

[61] B. M. Levine, K. Shaik, and T.-Y.Yan, "Data Analysis for GOPEX Image Frames," *The Telecommunications and Data Acquisition Progress Report, 42-114, April–June 1993*, pp. 213–229, Jet Propulsion Laboratory, Pasadena, California, August 15, 1993. http://ipnpr.jpl.nasa.gov/progress_report/

[62] J. D. Shelton, "Turbulence-Induced Scintillation on Gaussian-Beam Waves: Theoretical and Observations from a Laser Illuminated Satellite," *Journal of the Optical Society of America A*, vol. 12, pp. 2172–2181, 1995.

[63] P. A. Lightsey, "Scintillation in Ground-to-Space and Retroreflected Laser Beams," *Optical Engineering*, vol. 33, pp. 2535–2543, 1994.

[64] M. Jeganathan, K. E. Wilson, and J. Lesh, "Preliminary Analysis of Fluctuations in the Received Uplink-Beacon-Power Data Obtained from GOLD Experiments," *The Telecommunications and Data Acquisition Progress Report 42-124, October–December 1996*, Jet Propulsion Laboratory, Pasadena, California, pp. 20–32, February 15, 1996. http://ipnpr.jpl.nasa.gov/progress_report/

[65] M. Jeganathan, M. Toyoshima, K. Wilson, J. James, G. Xu and J. Lesh, "Data Analysis Results from the GOLD Experiments," *Free-Space Laser Communications Technologies IX, Proceedings of SPIE*, Ed., G. Stephen Mecherle, vol. 2990, pp. 70–81, 1997.

[66] C. Higgs, H. Barclay, D. Murphy, and C. A. Primmerman, "Multibeam Illumination," *Lincoln Laboratory Journal*, vol. 11, pp. 8–22, 1998.

[67] R. L. Mitchell, "Permanence of the Log-Normal Distribution, "*Journal of the Optical Society of America*, vol. 58, pp. 1267–1272, 1962.

[68] R. Barakat, "Sums of Independent Log-Normally Distributed Random Variables," *Journal of the Optical Society of America*, vol. 66, pp. 211–216, 1976.

[69] G. A. Tyler, "Bandwidth Considerations for Tracking Through Turbulence," *Journal of the Optical Society of America*, vol. 11, pp. 358–367, 1994.

[70] J. W. Hardy, *Adaptive Optics for Astronomical Telescopes*, Oxford University Press, Oxford, England, 1998.